UNIVERSIDAD DE CHILE
FACULTAD DE CIENCIAS FÍSICAS Y MATEMÁTICAS
ESCUELA DE POSTGRADO Y EDUCACIÓN CONTÍNUA

CONVECTIVE PRECIPITATION IN THE SUBTROPICAL ANDES OF CENTRAL CHILE: PHYSICAL MECHANISMS AND CLIMATE CHANGE PROJECTIONS

TESIS PARA OPTAR AL GRADO DE DOCTOR EN CIENCIAS DE LA INGENIERÍA, MENCION FLUIDODINÁMICA

MIGUEL ÁNGEL LAGOS ZÚÑIGA

PROFESOR GUÍA
Roberto Rondanelli Rojas

MIEMBROS DE LA COMISIÓN
René Garreaud Salazar
Ricardo Muñoz Magnino
Deniz Bozkurt
María Bettolli

Esta tesis fue financiada por la Agencia Nacional de Investigación y Desarrollo (ANID) a través de la beca de doctorado Nacional Folio 21192178.

SANTIAGO DE CHILE
2024

RESUMEN
PRECIPITACIÓN CONVECTIVA EN LOS ANDES SUBTROPICALES DE CHILE CENTRAL: MECANISMOS FÍSICOS Y PROYECCIONES DE CAMBIO CLIMÁTICO
POR: MIGUEL ÁNGEL LAGOS ZÚÑIGA
FECHA: 2024
PROF. GUÍA: ROBERTO RONDANELLI ROJAS

Los eventos de precipitación de verano representan menos que el 10% de la precipitación anual en los Andes sub-tropicales (30-35°S); sin embargo, sus condiciones cálidas pueden generar crecidas y aluviones debido a lo elevado del nivel de congelamiento. Comprender eventos históricos es crucial para evaluar condiciones futras más cálidas, sin embargo, la falta de registros largos confiables en altura, representa un desafío significativo, requiriendo el uso e interpretación de diversos productos meteorológicos y simulaciones numéricas; pese a esto, debido al alto costo computacional de modelos que resuelven explícitamente la convección (CPCM), una representación confiable de estos eventos en topografía compleja es un problema abierto en la comunidad científica.

La hipótesis de esta tesis, es que bajo condiciones de cambio climático, las precipitaciones de verano incrementarán en magnitud en los Andes sub-tropicales. Con el fin de estudiar posibles mecanismos asociados a esta hipótesis, seguí un enfoque de tres pasos desde Chile continental, hasta los Andes subtropicales: i) Calculé tendencias observadas en eventos de precipitación máxima diaria estacional (Rx1day estacional, Capítulo 2) y sus procesos asociados; ii) Exploré cambios de precipitación estacional y Rx1day estacional simulada por modelos de circulación global (GCMs) y regional (RCMs) durante condiciones de verano, así como aspectos termodinámicos, e índices de inestabilidad con el fin de identificar relaciones entre inestabilidad seca y húmeda, y las proyecciones de precipitación en los Andes entre 15 y 35°S, (Capítulo 3). iii) Finalmente, evalué simulaciones CPCM para dos eventos de precipitación de verano ($\sim 4km$) en el modelo *Advanced Research Weather and Forecasting model* (WRF) testeando diferentes esquemas y realizando un análisis de sensibilidad ante condiciones de temperatura superficial del mar más cálidas (ΔSST, Capítulo 4).

Los resultados muestran tendencias positivas de eventos Rx1day estacional durante el verano ($\sim$35°S) y otoño austral ($\sim$30°S), potencialmente explicados por un incremento en flujos de humedad hacia la costa norte de Chile, incremento de energía potencial convectiva disponible en los Andes, y fuertes gradientes de SST y circulación, como resultado de la intensificación del anticiclón sur-este del Pacífico sub-tropical. Las proyecciones de cambio climático de los modelos CMIP5 y RCMs sugieren una intensificación de precipitación extrema durante las temporadas cálidas, asociadas a mayor inestabilidad y humedad. Las simulaciones CPCM revelan una alta sensibilidad en la producción de precipitación y sus áreas de afectación a la capa límite planetaria, microfísica de nubes y modelo superficial del suelo. El experimento ΔSST, testeado en un evento de río atmosférico, revela cambios heterogéneos, pero sobre todo, una expansión hacia el norte de las precipitaciones. Estos resultados contribuyen a la comunidad relacionada al análisis de riesgos hidroclimáticos en la zona de estudio.

ABSTRACT
CONVECTIVE PRECIPITATION IN THE SUBTROPICAL ANDES OF CENTRAL CHILE: PHYSICAL MECHANISMS AND CLIMATE CHANGE PROJECTIONS
AUTHOR: MIGUEL ÁNGEL LAGOS ZÚÑIGA
DATE: 2024
ADVISOR: ROBERTO RONDANELLI ROJAS

Summer precipitation events represent less than 10% of annual rainfall in the sub-Tropical Andes (30-35°S); however, their warm conditions may generate flooding and landslides due to high freezing levels. Understanding historical events is crucial to evaluating future warmer conditions. Still, the lack of reliable long-term observations in higher elevations represents a significant challenge requiring the use and interpretation of diverse meteorological products and numerical weather simulations; however, due to the high computational cost of convection-permitting climate models (CPCM), a reliable simulation of those systems in complex topography is still an open problem in the scientific community.

This thesis hypothesizes that under climate change conditions, summer precipitation events will be enhanced in the sub-tropical Andes under warmer conditions. To elucidate the mechanisms associated with this hypothesis, I followed a three steps approach from Continental Chile to the sub-tropical Andes: i) I compute observed trends and associated mechanisms during maximum daily seasonal precipitation events (seasonal Rx1day, Chapter 2); ii) I explore seasonal precipitation and seasonal Rx1day projections in global circulation models (GCMs) and regional climate models (RCMs) during summer conditions, as well as thermodynamics, circulation, and instability indexes to identify relationships between dry and wet instability and projected trends in the Andes between 15 and 35°S, Chapter 3). iii) Finally, I evaluate CPCM simulations for two summer precipitation events ($\sim 4km$) in the Advanced Research Weather and Forecasting model (WRF), testing different schemes and performing a sensitivity analysis under warmer sea surface temperature conditions(Δ SST, Chapter 4).

The results show wetter and warming trends during seasonal Rx1day events during the austral summer ($\sim$35°S) and fall ($\sim$30°S), potentially due to increased moisture inflows to the North-Pacific coast of Chile, enhanced CAPE in the Andes, and strong SST and circulation gradients resulting from the intensification of the southeastern subtropical Pacific Anticyclone. Climate change projections of CMIP5 and RCMs models suggest an intensification of extreme precipitation during warm seasons linked to higher instability and wetter conditions. The CPCM simulations indicate a high sensitivity of planetary boundary layer, microphysics, and land surface schemes regarding total precipitation and the areas affected. The ΔSST experiment, tested in an atmospheric river event, reveals heterogeneous changes but, most importantly, a northward expansion of the studied event under warmer conditions. The results contribute to the hydrometeorological community regarding risk analysis, confirming an increase in the magnitude of flooding, which may raise the potential for landslides at higher rates than those simulated by regional and global models.

A mis estudiantes.

A mi hijo Edén quien siendo tan pequeñito nos abriste las puertas del cielo
A mi esposa Paula por su amor en su sí de cada día.
A mis hijos Benjamín y a José, por enseñarme a amar
. Les amo por siempre.

Y a ti mi Señor, que haces nuevas todas las cosas.

"Cuando veis una nube que se levanta en el occidente,
al momento decís: "Va a llover", y así sucede...
¡Hipócritas! Sabéis explorar el aspecto de la tierra
y del cielo, ¿cómo no exploráis, pues, este tiempo?"

Lucas 12, 54-56.

Agradecimientos

La investigación desarrollada en esta tesis de fue posible gracias al apoyo de a Agencia Nacional de Investigación y Desarrollo (ANID) a través de la beca de doctorado Nacional Folio 21192178, al programa de Doctorado en Fluidodinámica de la Universidad de Chile, al Centro de Investigación del Clima y la Resiliencia (CR)2 y al Laboratorio Nacional de Computación de Alto Rendimiento (NLHPC).

En primer lugar agradezco a quienes me entusiasmaron con las ciencias y me animaron a embarcarme en esta aventura, particularmente a la profesora Ximena Vargas por creer en mi cuando era su estudiante y a mi amigo Pablo Mendoza, quien con su amistad y alegría, siempre me motivó en este camino. Agradezco también a quienes me dieron las posibilidades y coraje de seguir trabajando en ciencia, docencia e investigación, en particular a Santiago Montserrat por ser un gran lider y compañero, a todo el grupo de Agua y Sustentabilidad Ambiental del AMTC quienes cada semana me entusiasman con su gran talento, dedicación y juventud. A mis compañeros de generación del doctorado, a Natalia Bustamante P. por todos sus consejos semestre a semestre. También agradezco a todas las personas que tuve el honor de tener como estudiantes, les agradezco de corazón, este logro es también por ustedes.

Quisiera también agradecer a todos los profesores que tanto me enseñaron en este tiempo, particularmente a René Garreaud, Ricardo Muñoz, Laura Gallardo y mi profesor guía Roberto Rondanelli, disfruté mucho cada una de sus clases y charlas. En particular agradezco a Roberto por aceptarme como su estudiante y por su apañe en todo el proceso, sus consejos, y su guía en cada paso. Agradezco a Claudio Falcón, a Lorena, a Camila, a Jorge y a Loreto (q.e.p.d.) de la EPEC por su ayuda durante mi estadía en el programa. Agradezco también a Deniz y a María Laura, así como a toda la comisión por sus valiosos comentarios y recomendaciones.

Realizar estos estudios no hubiera sido posible sin el apoyo y amor de mi esposa Paula, quien me lleva hacia una mejor versión de mi mismo, por su paciencia, resiliencia y por ser una mujer increible, excelente madre, esposa y profesional. Sin haber tomado el buque de la casa y nuestros hijos durante estos años, no podría haber terminado este proceso. A mis hijos Benjamín y José, quienes le prestaron su papá a la ciencia durante estos años, por enseñarme a amar y mostrarme la belleza de la vida, por su paciencia y amor en medio de mis debilidades y limitaciones. A mi pequeño Edén, quien en tan poco tiempo ensanchó nuestros corazones y nos abrió las puertas del cielo. No puedo dejar de agradecer a mis Padres, a mi hermana Andrea, a Eric y mi querida Francia, siempre están aquí.

Por último quiero agradecer a Dios, quien en cada umbral que intentamos cruzar del límite del conocimiento nos revela una pincelada de sus huellas en todo, desde lo pequeño en la turbulencia, hasta escalas planetarias: transferencia de masa, energía y movimiento, interactuando a con procesos químicos y biológicos, irradiados bajo un sol, procesos aleatorios y también cíclicos, en un sistema hermosamente caótico en nuestra casa común (¡que rota!)...¡cómo no sorprenderse con tanta belleza! ¡cuan insondables son sus caminos!, y aún así, en el rostro de Jesús, en su amor, podemos comprender todo. ¡Gracias por el don de la fe!

Table of Contents

Index of Tables

Index of Figures

Chapter 1

Introduction

1.1 Motivation

Summer convective precipitation events represent most of the annual precipitation in the South American continent (Garreaud, 2009; Huffman et al., 1997) as a result of high instability due to surface warming and moisture circulation in low levels. In the Eastern Andes (20-40°S), the convergence of circulation from the west, the South American Low-Level Jet, and the Southern mid flows generates favorable conditions for convection as in the *Sierras del Córdoba* (Rasmussen and Houze Jr, 2016; Pool et al., 2019). In the western slopes (30-35°S), these kinds of events represent less than 10 % of mean annual precipitation (Viale and Garreaud, 2014); nevertheless, they present high risk in the Andes region because of the warm nature during their occurrence, with freezing levels higher than 4000 [m a.s.l.], exposing western catchments to flooding and landslides.

Diverse studies have shown a general reduction in wet days and intensification of extreme precipitation events (EPEs) (Fischer and Knutti, 2016; Trenberth, 2011). Additionally, in some mountainous regions, there is evidence of higher warming rates than low lands and valleys (Pepin et al., 2015; Falvey and Garreaud, 2009a; Souvignet et al., 2012); evidence that in conjunction with a higher humidity-holding thermodynamic capacity of the atmosphere (Pfahl et al., 2017), may produce more severe precipitation of convective events as a result of higher available instability (Rädler et al., 2019) as shown in regional circulation models (RCMs) in the European Alps (Giorgi et al., 2016; Rädler et al., 2019), the mountainous zones of Cameroon(Sylla et al., 2012), the United States of America (Seeley and Romps, 2015) and Australia (Allen et al., 2014). The potential effects on the destabilization of the troposphere oppose the expected stabilization due to higher warming rates observed and modeled in mid and high troposphere levels (Sherwood and Nishant, 2015; Steiner et al., 2020; Ladstädter et al., 2023).

Numerical climate models, both regional and global models, do not explicitly resolve convection and use parametrization for processes that cannot be represented within their grid spaces (e.g., turbulence, boundary layer, cloud microphysics, Bauer et al. (2015)). Additionally, feedbacks present in convection-scale models ($\sim 3-4km$) need to be resolved to understand their role in precipitation generation better Fowler et al. (2021). Consequently, the community is advancing to the realization of Convection-Permitting simulations as a tool to understand better the physics and interaction between land and atmosphere (e.g., Liu et al. (2017).

Within this context, this thesis aims to contribute to the understanding of dynamics and thermodynamic factors affecting the generation of convective precipitation in the sub-tropical

Andes through observational products and numerical simulations in the generation of convective precipitation and explore expected changes in frequency and magnitude of these events in the context of a warming climate (Boisier et al., 2016a; Schumacher et al., 2020b; Souvignet et al., 2012; Falvey and Garreaud, 2009b; Burger et al., 2018).

1.2 Background

Summer precipitation during summer in the sub-tropical Andes was characterized by Viale and Garreaud (2014), which identified two main mechanisms: i) forced through weak winds, with strong convection (80% of cases), and ii) through strong winds, similar to wintertime baroclinic activity. Both cases are influenced in the generation of precipitation because of the prominent elevation of the Andes, which can enhance precipitation (Barrett et al., 2009; Garreaud et al., 2016; Massmann et al., 2017) when the Froude number of the circulation is larger than 1 ($Fr = \frac{U}{NH} > 1$), otherwise, the flow may be blocked Scaff et al. (2017). Where U is the mean flow velocity, N is the Brunt-Väisälä frequency, and H is the mean barrier height (Markowski and Richardson, 2011). The precipitation type in the Andes is prominently stratiform but also presents cumulonimbus and intense convective precipitation in the western Andes (Viale et al., 2019), a fact that also unveils the Mountainous impact of these kinds of precipitation events (Viale and Garreaud, 2014; Poveda et al., 2020).

The genesis of precipitation in Chile strongly depends on the latitudes, being EPEs frequently associated with atmospheric rivers (ARs) and baroclinic instability processes (Viale and Nuñez, 2011; Valenzuela and Garreaud, 2019). This synoptic configuration favors water vapor convergence on the Chilean coasts. Falvey and Garreaud (2007) found strong correlation ($r^2 \sim 0.4$) between moisture transport[1] and EPEs at 2000 [m a.s.l]. Similar results were found by Valenzuela and Garreaud (2019), who reported that the Integrated Water Vapor Transport (IVT), explains 40% of the variance of EPEs. Additional large-scale circulation, such as Cut-Off Lows (COLs), in configuration with positive anomalies in Sea Surface Temperature (SST), can produce severe storms as the Atacama Floods in 2015 (Bozkurt et al., 2016; Rondanelli et al., 2019), influenced by mesoscale processes as warm season instability and forced ascent that have an important role in precipitation production.

Positive trends of EPEs have been reported worldwide (Sharma et al., 2018; Pepin et al., 2015; Trenberth, 2011; Regoto et al., 2021). In particular, Meredith et al. (2019) indicates that this intensification has a strong diurnal signal associated with convective precipitation events. These signals, in daily precipitation during summer, appeared in the Souvignet et al. (2012) study for the Coquimbo Region in Chile ($\sim 30°$S). However, an extensive revision of the presence of trends in Chile needs to be addressed, including associated mechanisms and seasonality.

The Clausius-Clapeyron relationship (Clapeyron, 1834; Clausius, 1850), indicates that the thermodynamic equilibrium between solid-liquid phases depends only on air temperature (T), and in the context of a warmer climate can be interpreted as higher vapor holding capacity in the atmosphere, before the condensation process (CC, Eq. 1.1).

[1] $\rho_v \vec{U}$, where ρ_v is water vapor density, and $\vec{U}$ is the wind speed.

$$\frac{de_s}{dT} = \frac{L_v e_s}{R_v T^2} \tag{1.1}$$

where L_v is the latent heat of evaporation, e_s is the saturation vapor pressure, T, the absolute air temperature, and R_v the gas constant for water vapor.

In the context of a warming world, the increase in temperature is thermodynamically associated with greater water vapor capacity in the atmosphere and leads to an enhancement in precipitation compared to historical conditions. This intensification has been documented through observations and expected through climate models (Fischer and Knutti 2016, and references therein), translating into fewer precipitation days and higher frequencies in EPEs in Europe and USA. This water vapor enhancement is typically known as Clausius-Clapeyron and reaches around $7\%/°C$ (Fowler et al., 2021), reproduced by climate models in historical simulations (e.g., Algarra et al., 2020).

In Chile, there are expected warming signals averaging $1.2 - 1.5°$ C in the 2030-2060 period in comparison to the historical 1985-2005 period (DGA, 2017; Bozkurt et al., 2018), reaching higher changes at the Andes at the end of the XXIth century $\sim$ 3.8°C in the RCP8.5 scenario, reaching in some cases up to 6° C (Araya-Osses et al., 2020). In terms of precipitation, the general picture is to drier conditions (Araya-Osses et al., 2020; Vicuña et al., 2010; DGA, 2017), explained by enhanced subsidence in the subtropics (Pfahl et al., 2017), and the poleward expansion of the Hadley Cell (He and Soden, 2017; Grise and Davis, 2020; Zhao et al., 2016). Nevertheless, some models project intensification of EPEs for some regions of Chile and South America (Ortega et al., 2019; Lagos-Zúñiga et al., 2022a). Additionally, the projections for warm precipitation will increase up to 25% in the high Andes (>3300 m a.s.l., 30°-38°S), according to Mardones and Garreaud (2020), enhanced warming trends in numerous mountain ranges worldwide (Pepin et al., 2015), reaching between 0.4-0.5 $°C/decade$.

Additionally, some regional models in mountainous regions project enhancement of precipitation in regional climate models that paradoxically contradict their drying signals (Bozkurt et al., 2019; Giorgi et al., 2016; Hodnebrog et al., 2022). These projections are consistent with different convection schemes models and observed trends in high elevations (Pepin et al., 2015; Giorgi et al., 2019; Scaff et al., 2019). In Giorgi et al. (2016) they hypothesize that this increase in precipitation in the Alps could be explained by enhanced convection as a result of surface warming and a decrease of the snow retreat and the change in the albedo feedback in the energy balance. Therefore, studying the physical processes at the convection scale is critical to disentangle the roles during summer precipitation events in warmer conditions.

Considering the lapse rate, commonly used as a proxy of instability (Markowski and Richardson, 2011), we can expect the joint effect of three mechanisms affecting the stability at the mesoscale, summarized in Figure 1.1: i) Stabilization effect by enhanced warming in high levels (Sherwood and Nishant, 2015; Ladstädter et al., 2023), ii) Rise in instability due to expected surface warming, and snow retreat at mountainous areas (Giorgi et al., 2019; Araya-Osses et al., 2020; DGA, 2017), and iii) Enhanced convective activity due to higher water vapor in low levels (Fischer and Knutti, 2016; Algarra et al., 2020; Pfahl et al., 2017).

The scheme summarizes the effect of future climate (red box) on the Convective Available Potential Energy (CAPE) compared with the present climate (blue box). The future climate effects are the enhanced warming in upper levels and its consequence in less CAPE (effect i, left panel in red box) in a future climate. The central and right panels in the red box show the increased CAPE due to surface heating and moistening (effects ii and iii, right panels in red box) compared to a present climate profile of virtual temperature (T_v).

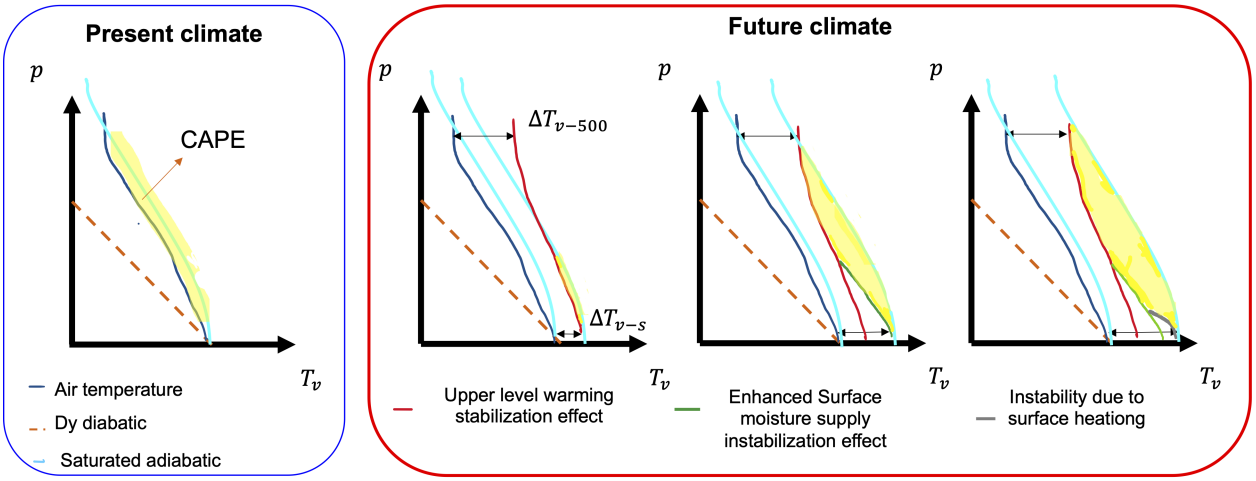

Figure 1.1: (Left) Vertical structure of virtual temperature in the present climate in the presence of CAPE (yellow). (right) Joint effects on the troposphere stability due to differentiated warming rates (less CAPE than present climate), surface heating, and higher humidity in low levels, which are expected in future climates (higher CAPE than present climate).

1.3 Hypothesis

The research hypothesis proposes that warmer conditions will increase the magnitude and frequency of extreme convective precipitation in response to a higher vapor supply in the atmosphere and enhanced summer instability in the subtropical Andes (30-35°S).

1.4 Objectives

Main objective

To comprehend the physical mechanism associated with convective precipitation in the subtropical Andes through numerical weather models in warmer conditions and to understand the influences of thermodynamic and dynamic aspects.

Specific objectives

OE1 : To determine trends in extreme precipitation events in continental Chile and associated temperatures, analyzing seasonal behavior and related physical processes.

OE2 : To verify simulated processes in RCMs in the subtropical Andes, emphasizing convective precipitation due to warming conditions.

OE3 : To determine the Advance Weather and Forecasting Model (WRF) ability to represent convective summer precipitation testing different physical schemes related to surface processes and cloud microphysics in convection-permitting simulations.

OE4 : Through a sensitivity over SST, investigate potential changes in spatio-temporal behavior of extreme summer precipitation historical events, considering an ensemble mean perturbation from selected CMIP6 models.

1.5 Methodology

To achieve the OE1, in collaboration with other co-authors, we worked with long-term daily precipitation and associated maximum and minimum temperature in continental Chile for maximum seasonal extreme daily precipitation events through the Sen's slope (Sen, 1968) and Mann-Kendall (Kendall, 1948) test of significance. Changes in SST, CAPE, and Precipitable Water (PW) were analyzed, as well as upper air observations and anomalies in meridional winds and AR frequency.

The OE2 considered mainly regional climate model simulations from the CORDEX-Core initiative: REMO (Jacob et al., 2007), RegCM4.7 (Giorgi et al., 2012), as well as regional simulations from the Eta Model (Mesinger et al., 2012), and the simulations from Bozkurt et al. (2019). An analysis of synoptical features related to seasonal changes in extreme precipitation, their magnitude, and frequency was performed for each simulation. The analysis of changes in convective precipitation was achieved through the Instability Index used by Giorgi et al. (2019) and the attribution analysis provided by Hodnebrog et al. (2022).

The Convection-Permitting simulations were performed in the WRF (Skamarock et al., 2019), testing different surface schemes in land surface processes: boundary and surface layers, land-surface model, and cloud microphysics. Other schemes were adopted from Yáñez-Morroni et al. (2018). The impact in the vertical and horizontal resolution of the models to represent two summer precipitation events is also considered. The simulations were assessed through satellite information from IMERG (Huffman et al., 2015), upper air soundings, and surface observations of temperature, precipitation, humidity, wind, and boundary layer height (OE3).

Finally, the impacts of warmer conditions in summer precipitation events were achieved through an SST warming approach. The change signal was obtained by selected Global Climate Models (GCMs) from the CMIP6 simulation under the SSP5-8.5 scenario (O'Neill et al., 2014), applied to a historical summer precipitation event. The WRF simulations were performed in the National Laboratory of High-Performance Computing from the Physical and Mathematical Sciences Faculty, *Universidad de Chile* (OE4).

1.6 Thesis structure

The following chapters of this document include research articles: Chapter 2 is published, Chapter 3 is under review, and Chapter 4 is in preparation, all for indexed journals in atmospheric sciences. The format of each chapter was adapted to the thesis document and did not correspond to the actual layout of the manuscripts. In Chapter 5, I provide the conclusions, limitations, and future work of the research. Part of this work was presented at international conferences of the American Geophysical Union (Lagos-Zúñiga et al., 2021d, 2022b), The European Geosciences Union (Lagos-Zúñiga et al., 2021a), The International Atmospheric River Conference (Lagos-Zúñiga et al., 2022c), The Physical Oceanography, Meteorology, and Climate of the East South Pacific conference (Lagos-Zúñiga and Rondanelli, 2022), the Chilean Conference of Hydraulics Engineering (Lagos-Zúñiga et al., 2021b) and the Convection-Permitting Climate Workshop (Lagos-Zúñiga et al., 2022d). Finally, in the context of national and international collaboration done during the thesis, I participated in publications related to the atmospheric sciences, mountain hydrology, and climate change (Lagos-Zúñiga et al., 2022a; Zegers et al., 2021; Machado Crespo et al., 2022; Gateño et al., 2023; Dominguez et al., 2023), and other ongoing initiatives.

Chapter 2

Trends in seasonal precipitation extremes and associated temperatures along continental Chile

This chapter was prepared with the contributions of Pablo A. Mendoza, Diego Campos, and Roberto Rondanelli. It was published in January 2024 in Climate Dynamics. https://doi.org/10.1007/s00382-024-07127-z

Abstract

We characterize trends in maximum seasonal daily precipitation (seasonal Rx1day), minimum (Tn), and maximum (Tx) daily temperatures during days with precipitation over continental Chile for the period 1979-2017, using surface stations and the AgERA5 gridded product derived from ERA5 reanalysis dataset. We also examine seasonal trends of Sea Surface Temperature (SST), Precipitable Water (PW), Convective Available Potential Energy (CAPE), Eddy Kinetic Energy (EKE), Atmospheric Rivers (ARs) frequency, and upper air observations to seek possible mechanisms that explain precipitation trends. Our results show an increase in seasonal Rx1day during fall in the south part of Northern Chile (15-30°S) and during fall and winter in Austral Chile, and mostly negative trends in Central Chile (30-36°S) where a few locations with positive trends appear along the coast during summer. Temperature trends presented cooling patterns north of 33°S in almost all the seasons (¡ -2°C/dec) while warming trends prevail south of 38°S (¿ 1 °C/dec). The highest values in Tn trends are obtained on the western slopes of the Andes around 30°S. We also explore temperature scaling in surface stations, finding strong positive super Clausius Clapeyron with Tn, especially between the fall and spring seasons in the 33-40°S region. Sounding observations in five stations across Chile suggest warming trends at 23.5°S, °S, 33°S, and 53°S, with a stabilization effect by enhanced warming in the upper troposphere while presenting cooing trends in Puerto Montt (4.15°S). Seasonal trends in PW reveal moistening along the southern-Peru and Northern-Chile during spring and summer. Positive trends in CAPE are observed over 35-40°S (austral summer and fall) and the northern Altiplano (autumn). SST analyses reveal strong cooling around 30°S in winter, explaining the negative trends in seasonal Rx1day in central Chile. A warming spot on the northern Peruvian coast during fall may be responsible for humidification in front of Northern Chile, particularly during summer and fall. Positive EKE trends are detected south of 40°S, being stronger and reaching almost all of the coast during spring. ARs frequency unveils negative trends up to -5 days/dec during summer and positive trends of 1 day/dec in 40°-50°S coastal

regions during spring. More generally, the results presented here shed light on the main large-scale processes driving recent trends in precipitation extremes across continental Chile.

Keywords: Seasonal maximum daily precipitation, freezing level, warm precipitation, trends.

2.1 Introduction

Precipitation is an essential input for hydrological studies, modulating water availability and the occurrence of extreme events like floods and landslides. During the last decades, several studies have shown significant variations in extreme precipitation regimes (Trenberth, 2011; Fischer and Knutti, 2016; Fowler et al., 2021), which have been attributed to climate variability (Pei et al., 2018; Martel et al., 2018) or anthropogenic climate change (Mukherjee et al., 2018; Zou et al., 2021). Changes in extreme precipitation have been documented worldwide (Fowler et al., 2021) and have contributed to defining guidelines for adaptation, risk management, and engineering design (Martel et al., 2021). Further, floods and debris flows risk analyses may benefit from characterizing possible changes in extreme precipitation events (EPEs) and associated temperatures, especially in mountainous areas, where a future intensification of EPEs under warming conditions is expected (Fischer and Knutti, 2016).

Improved understanding of precipitation extremes is crucial for a thorough assessment of historical climate model simulations (Paxian et al., 2015; Alexander, 2016), to evaluate the realism of gridded meteorological datasets (e.g., Schumacher et al. 2020b), and to examine possible relationships between warming/drier conditions, and potential changes in the frequency and intensity of EPEs. Previous studies have reported seemingly contradictory trends: a decrease in wet day fraction and together with more intense precipitation events in some regions of the United States (Janssen et al., 2014; Prein and Mearns, 2021), Europe (Zolina et al., 2008; Fischer and Knutti, 2016), Australia (Guerreiro et al., 2018), China (Zhai et al., 2005; Shi et al., 2019), India (Pal and Al-Tabbaa, 2009) and Russia (Aleshina et al., 2021). In principle, such trends in the EPEs can be connected to the Clausius-Clapeyron scaling of the water vapor with surface temperature (Fischer and Knutti, 2016; Wang et al., 2017; Guerreiro et al., 2018; Fowler et al., 2021). Nevertheless, the intensification of EPEs is not homogeneous across seasons, and negative trends have also been reported in the literature; therefore, changes in the local thermodynamics and large-scale phenomena need to be analyzed to better understand the observed trends.

In South America, a few studies have examined trends in extreme precipitation, mainly based on different Indices provided by the Expert Team on Climate Change Detection and Indices (ETCCDI, Karl et al. 1999). Cerón et al. (2021) analyzed the trend in maximum 5-day precipitation (Rx5day) in La Plata Basin using the (CHIRPS product Funk et al., 2015), finding opposite annual and seasonal trends (-20 to 20 mm/dec). More recently, Regoto et al. (2021) analyzed surface stations across Brazil, finding different spatial behavior of trends ranging from -30 and +30 mm/dec, analyzing Rx1day and Rx5day events. Cerón et al. (2022) found similar patterns with the CHIRPS product for seasonal EPE in Colombia,

with an intensification of up to 20 mm/dec for RX5day events during the warm seasons.

Continental Chile (∼17-57°S) spans a myriad of hydro-climatic conditions, from extremely arid in the north to extremely humid in the south. According to the Köppen-Geiger climate classification, the prevailing climates in this domain are Arid, Temperate, and Polar (Sarricolea et al., 2017), which are influenced by the Andes Cordillera and coastal mountains, which enhance orographic precipitation (Falvey and Garreaud, 2007; Barrett et al., 2009; Garreaud et al., 2016; Massmann et al., 2017; Scaff et al., 2017; Viale et al., 2019). The Altiplano in Northern Chile is influenced by the upper-level Bolivian High and moisture advection from the Amazonas, with precipitation events occurring during the austral summer (Vuille, 1999; Garreaud, 2000; Garreaud and Aceituno, 2001; Espinoza et al., 2020). Arid and hyper-arid conditions prevail on the western side of the Northern Andes, with observed mean annual precipitation varying between ∼1 mm in Arica (18.5°S) to 85 mm in La Serena (29.5°S). Cutoff lows (COLs) strongly influence precipitation events in these latitudes, contributing up to 50% of mean annual amounts (Aceituno et al., 2021; Muñoz and Schultz, 2021) and triggering extreme events like the Atacama floods in 2015 (Barrett et al., 2016; Bozkurt et al., 2016; Wilcox et al., 2016). In central Chile, most precipitation events are related to mid-latitude baroclinic perturbations and are usually accompanied by atmospheric rivers (ARs), which contribute up to 40% of extreme precipitation amounts (Aceituno et al., 2021; Valenzuela and Garreaud, 2019; Viale et al., 2018). Although most EPEs occur during the austral winter, some events are observed during the warm season (Viale and Garreaud, 2014; Valenzuela et al., 2022), mainly associated with COLs. On the other hand, precipitation events are evenly distributed during the year in southern and Austral Chile (Aceituno et al., 2021). In general, at different scales, all precipitation events are strongly teleconnected with tropical modes of variability such as the Madden-Julian Oscillation (Juliá et al., 2012; Barrett et al., 2009; Rondanelli et al., 2019), the Pacific Decadal Oscillation, and El Niño Southern Oscillation (Garreaud, 2009; Schumacher et al., 2020b; Aceituno et al., 2021).

To our knowledge, no previous studies have charaterized seasonal trends in extreme daily precipitation and associated temperatures in Chile. Further, only a few studies have examined trends in precipitation and temperature across continental Chile, focusing on climatological aspects such as mean annual temperature (e.g. Falvey and Garreaud, 2009b) and mean annual precipitation (e.g., Boisier et al., 2016a), or other metrics such as precipitation concentration (Sarricolea et al., 2019) and aggressiveness (Valdes-Pineda et al., 2016). Souvignet et al. (2012) studied northern Chile (29-32°S), finding positive trends in fall and negative trends in spring (1964-2006), and a positive trend in Rx5days over the Andean region (¡ 10 mm/dec), and no clear spatial patterns in other climate change ETCCDI indices. Valdes-Pineda et al. (2016) showed positive, weak (i.e., not statistically significant) trends in annual precipitation (36- 44°S), finding significant, positive trends north to 42°S during the 1996-2006 period and some negative trends to the south; nevertheless, they found fewer stations with significant trends when considering a longer time-window (1914-2006). Boisier et al. (2016b) reported regional drying conditions for annual precipitation (-65 mm/dec) in central-southern Chile (30-40°S) from 1979 to 2014. More recently, Schumacher et al. (2020b) reported positive trends in summer precipitation north of 26°S and negative trends

in austral winter precipitation (26-35°S), in the 1985-2015 period.

In terms of temperature, Falvey and Garreaud (2009b) reported positive trends in mean annual values on valley and mountain stations (0.25 °C/dec) and coastal cooling (-0.2 °C/dec) with surface observations in the 1979-2006 period. Positive trends have generally for northern Chile's maximum and minimum temperatures (0.46 °C/dec, Souvignet et al., 2012). Schumacher et al. (2020b) found generally warmer conditions between 15-40°S, without clear signals of change in extreme temperatures. Those trends have induced upward trends in the snow line elevation of 10-30 m/year south of 29–30°S (Saavedra et al., 2018).

Previous studies analyzed extreme precipitation events in Chile considering: (i) the relationship between water vapor transport at different pressure levels (e.g., Falvey and Garreaud,2007), (ii) the role of the Andes in orographic precipitation (Barrett et al., 2009; Garreaud, 2009; Massmann et al., 2017), and (iii) the Integrated Vapor Transport (IVT) and its role on EPEs (Valenzuela and Garreaud, 2019) and landslides (Rutllant et al., 2023). Hence, summer precipitation events have received less attention because they contribute less than 10% of annual precipitation (Viale and Garreaud, 2014). Nevertheless, these events have triggered floods and/or debris flows, with economic damages and fatalities in the Arid Atacama region (Bozkurt et al., 2016; Rondanelli et al., 2019), the Austral Santa Lucía village (Somos-Valenzuela et al., 2020) and Central Chile (Valenzuela et al., 2022), due to a rise in rainfall contributing area and humidity, leading to higher storm intensity. Additionally, regional and global projections indicate an increase in EPEs for Northern Chile (Ortega et al., 2019) with higher freezing level conditions (Mardones and Garreaud, 2020) and generally drier and warmer climatic conditions (Araya-Osses et al., 2020; Vicuña et al., 2021).

This paper aims to detect and characterize seasonal maximum daily precipitation trends and study their thermal characteristics, including freezing level behavior across continental Chile, analyzing temperature Clausius-Clapeyron scaling. Specifically, we examine surface meteorological observations and upper air sounding data during the 1973-2017 period. We also explore climatological trends in precipitable water (PW) and instability. to better understand the influence of large-scale processes on the seasonal extreme precipitation events, we also analyze Sea Surface Temperature (SST), Eddy Kinetic Energy (EKE), and Atmospheric Rivers frequency to discuss possible mechanisms that explain some of the detected trends.

2.2 Data

Precipitation (Pr), maximum (Tx), and minimum (Tn) daily temperature data for the period 1979-2017 were obtained from 405 meteorological stations (Fig. 2.1b) for Pr, and 129 for Tn and Tx (Fig. 2.1c), managed by the Chilean Water Service (*Dirección General de Aguas, DGA*) and the National Weather Service (*Dirección Meteorológica de Chile, DMC*) gathered by the climate explorer service (CR2, 2020). These observations are not homogeneously distributed across continental Chile and are mainly concentrated below 2000 m above sea level (m a.s.l. Fig. 2.1d-g). The quality control of meteorological surface station data included the Buishand (1984) U Test for annually-averaged time series, exclusion of stations

with more than two years of gaps, and removal of records with Tn > Tx. To analyze data with complete records, we also performed a quantile mapping procedure to fill missing data with neighboring stations based on the day of the year, selecting the best neighbor station to complete missing information following Tang et al. (2020).

We also used records of temperature, freezing level elevation (H_0, 0° isotherm), and PW from five upper air stations (Table 2.1, Fig. 2.1a). To analyze stability trends, we computed surface convective available potential energy (CAPE), which can be used as a proxy for the maximum updraft strength within a thunderstorm, and convective inhibition (CIN), which is used as a proxy for near-surface stability. All radiosonde variables were observed at 12 UTC (8 hours local time) on the same day of the maximum daily seasonal precipitation per year, hereafter referred to as seasonal Rx1day.

We discarded sounding days with short records of thermodynamic variables required to compute CAPE/CIN and PW - defining a minimum pressure level 500 hPa. We truncated observations up to 10 km a.s.l. and obtained the freezing level by linearly interpolating these observations along the vertical after finding the first record with a temperature below 0°C. If the observed surface temperature was <0° C and positive at higher tropospheric levels, the H_0 calculation was performed, considering the second negative observation from the surface. CAPE/CIN and PW were computed using the MetPy Python library (May et al., 2022).

Table 2.1: Radiosonde stations analyzed in this study and some of their characteristics.

Radiosonde station	WMO code	Latitude	Longitude	Elevation [m a.s.l.]	Observational Period
Antofagasta	85442	-23.45	-70.44	115	Jan 1973 - Dec 2017
Quintero	85543	-32.79	-71.53	13	Jan 1973 - Dec 1999
Santo Domingo	85586	-33.64	-71.61	77	Dec 1999 - Jan 2017
Puerto Montt	85799	-41.45	-73.08	87	Jan 1973 - Dec 2017
Punta Arenas	85934	-53.00	-70.85	36	July 1976 - Dec 2017

Given the considerable changes in upper-air observational technologies over the period (Elliott and Gaffen, 1991; Ross and Gaffen, 1998), we refrained from computing seasonal trends using radiosonde data. From Antofagasta to Puerto Montt (Table 2.1), we considered a year complete when more than 182 days of records were available. In the case of Punta Arenas, we considered years with a minimum of 90 days of observations, homogeneously distributed within the year, because of significantly fewer records in this than the others (See Figures A.1 to A.5).

The outlier detection for seasonal Rx1day events and associated temperature followed the US Water Council recommendation for skewed data, removing data over a threshold of 2.7 standard deviations from the mean in a sample of 40 data in annual maximum series (Te Chow et al., 1988). We followed the same recommendations in the sounding data.

We also used PW, CAPE, and CIN from the European Centre for Medium-Range Weather Forecasts Reanalysis version 5 (ERA5 Hersbach et al. 2020) at 12 UTC to emulate

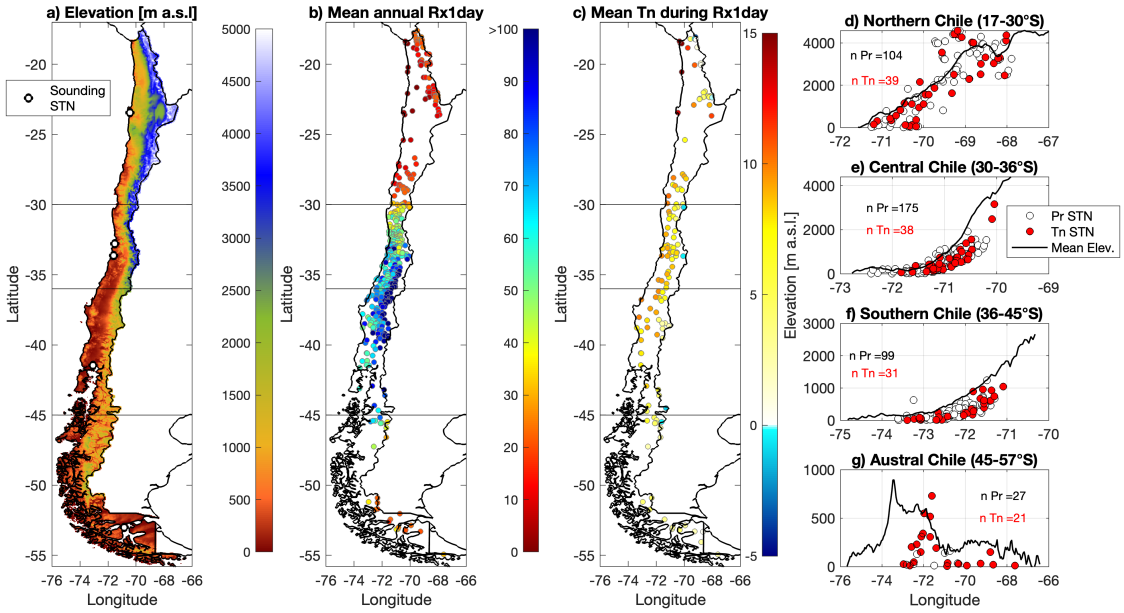

Figure 2.1: a) Elevation of continental Chile and location of the five radiosonde stations, b) Mean annual Rx1day, c) Mean Tn during mean annual Rx1day, d)-g) Mean longitudinal elevation by region, Pr stations (white circles), and Tn/Tx stations (red circles). The horizontal lines in panels a-c) represent the limits between Northern (15-30°S), Central (30-36°S), Southern (36-45°S), and Austral (45-57°S) Chile.

the observational time at the sounding stations; SSTs retrieved from the extended National Oceanic and Atmospheric Administration (NOAA) reconstructed SST v5 (Huang et al., 2017); and Pr from the agrometeorological product derived from hourly surface ERA5 product, hereafter, AgERA5 (Boogaard et al., 2020). This product was aggregated to daily time steps and corrected towards a finer topography at a 0.1° spatial resolution (Boogaard et al., 2020). Here we do not show the results of Tx and Tn during seasonal Rx1day trends, as the spatial correlation between observations and AgERA5 was weak and even negative for some regions and seasons (not shown).

2.3 Methodology

2.3.1 Trend detection

Seasonal trend analyses were performed separately over austral (i) summer (DJA), fall (MAM), winter (JJA), and spring (SON) Rx1day time series derived from meteorological stations; (ii) observed Tx, and Tn during seasonal Rx1day; and (iii) observed PW, H_0 and air temperature from the radiosonde station closest to a Pr surface station. The magnitude of detected trends was quantified with Sen's slope estimator (Sen, 1968), and

their statistical significance was determined through the Mann-Kendall test (Mann, 1945; Kendall, 1948), implemented in the Matlab package *Taub* (Burkey, 2021). A trend was considered statistically significant if the p-value was < 0.1, i.e., 90% of interval confidence. We repeated these analyses using the AgERA5 for comparative purposes and computed the Spearman rank correlation coefficient between AgERA5 trends simulated and the observed trends at the nearest grid cell for each meteorological station.

In the case of Tx and Tn trends (dT/dt), we also computed the altitudinal change of temperature (dH/dt) with Eq. 2.1, to compare against the variation of H_0 (dH_0/dt) obtained with the soundings.

$$\frac{dH}{dt} \approx \frac{1}{\gamma}\frac{dT}{dt} \tag{2.1}$$

In Eq. 2.1, we considered a standard lapse rate of $\gamma \approx -5.9°C/km$ as a reference to help the discussion of impacts associated with temperature trends during Rx1day events based on the analysis of wet days performed by (Ibañez et al., 2021) and (Lagos-Zúñiga et al., 2021c) around 33°S.

To examine possible connections between physical mechanisms and the detected trends, we analyzed trends in seasonal-averaged values of PW and CAPE - retrieved from ERA5 (Hersbach et al., 2020)-, and reconstructed SST time series (Huang et al., 2017). Additionally, we computed trends in the storm track activity and atmospheric river frequency to examine the role of synoptic-scale precipitation systems in the long-term trends in seasonal Rx1day and associated Tx and Tn.

As a measure of storm track activity, we calculated the vertically-averaged eddy kinetic energy (EKE, Eq. 2.2 using daily 12 UTC data from ERA5 reanalysis from 850 hPa to 500 hPa, with a ten-day high-pass filter for the Southern Hemisphere (e.g., Shaw et al. 2016),

$$EKE = \frac{1}{2}\overline{u'^2 + v'^2} \tag{2.2}$$

where u' and v' denote the high-frequency fluctuation of winds, i.e., daily differences from the mean wind. For the AR frequency, we used the AR catalog from Guan and Waliser (2015) derived from ERA-Interim data. Seasonal trends and Associated statistical significance were also computed through Sen's Slope and Mann-Kendall tests.

2.3.2 Temperature scaling

The Clausius-Clapeyron equation states that the saturation vapor pressure in the atmosphere increases with temperature at a rate of ~7%/°C and has been used to compare against observed and modeled trends in extreme precipitation in a warming world scenario (e.g., Fischer and Knutti 2016). The CC scaling can be computed with different approaches such as binning temperatures, considering hourly extreme precipitation, hourly and daily temperature, or dew-point temperature (Martinkova and Kysely, 2020). Since the binning temperature approach led to high variability in the results in our study region (not shown), we decided to report scaling results with all the events by season, fitting a linear regression

between the non-dimensional seasonal Rx1day predictand ($y_{season}(t)$, Eq. 2.3, where t denotes a year) and observed predictors (Tx and Tn) for at least 5 years with Rx1day > 1 by season, considering a 90% confidence level:

$$y_{season}(t) = Rx1day(t)_{season} / \overline{Rx1day_{season}} \tag{2.3}$$

2.3.3 Radiosonde variations

Radiosonde measurements of PW, CAPE, CIN, and H_0 were also analyzed to detect changes in 21-year averages across wet days (Pr $>$ 1 mm) and dry days, using the Wilcoxon rank-sum test (Wilcoxon, 1992). Santo Domingo and Quintero are compared to each other preferentially since they are $\sim$ 95 km apart. For example, in Antofagasta, the compared periods are 1973-1995 and 1996-2017.

We computed the Sen's slope to interpolated averaged values between 1000 hPa to 100 hPa every 50 hPa during wet and dry days. To compute trends, we considered complete soundings reaching at least 500 hPa ($\sim$5600 m a.s.l.). The completitude of records per year, pressure level, and years considered for trend calculation for each radiosonde station are shown in Fig. A.6.

2.4 Results

2.4.1 Precipitation trends

Stations with significant positive trends were found for all seasonal Rx1day time series, with the largest magnitudes ($>$ 4 mm/dec) obtained for fall (MAM) in northern Chile (Fig. 2.2b) and during winter between 38-45°S. The strongest negative trends are observed during fall and spring in Central and Southern Chile between 32-37°S (Fig. 2.2b,d, $<$ -10 mm/dec). Interestingly, the intermediate seasons, fall and spring Rx1day, present the most surface stations with statistically significant trends of 15% and 20% from all the stations, respectively. The southern part of the Austral region (south of 40°S) exhibits generally positive trends in Rx1day for summer, fall, and winter (Fig. 2.2a-c). The AgERA5 product provides similar spatial patterns in Rx1day trends for all seasons (Fig. 2.2e-h), with Pearson correlation between observed and simulated trends $r > 0.5$ between fall and spring (Fig. 2.2i-l). At the same time, there is a low correlation during summer ($r = 0.37$).

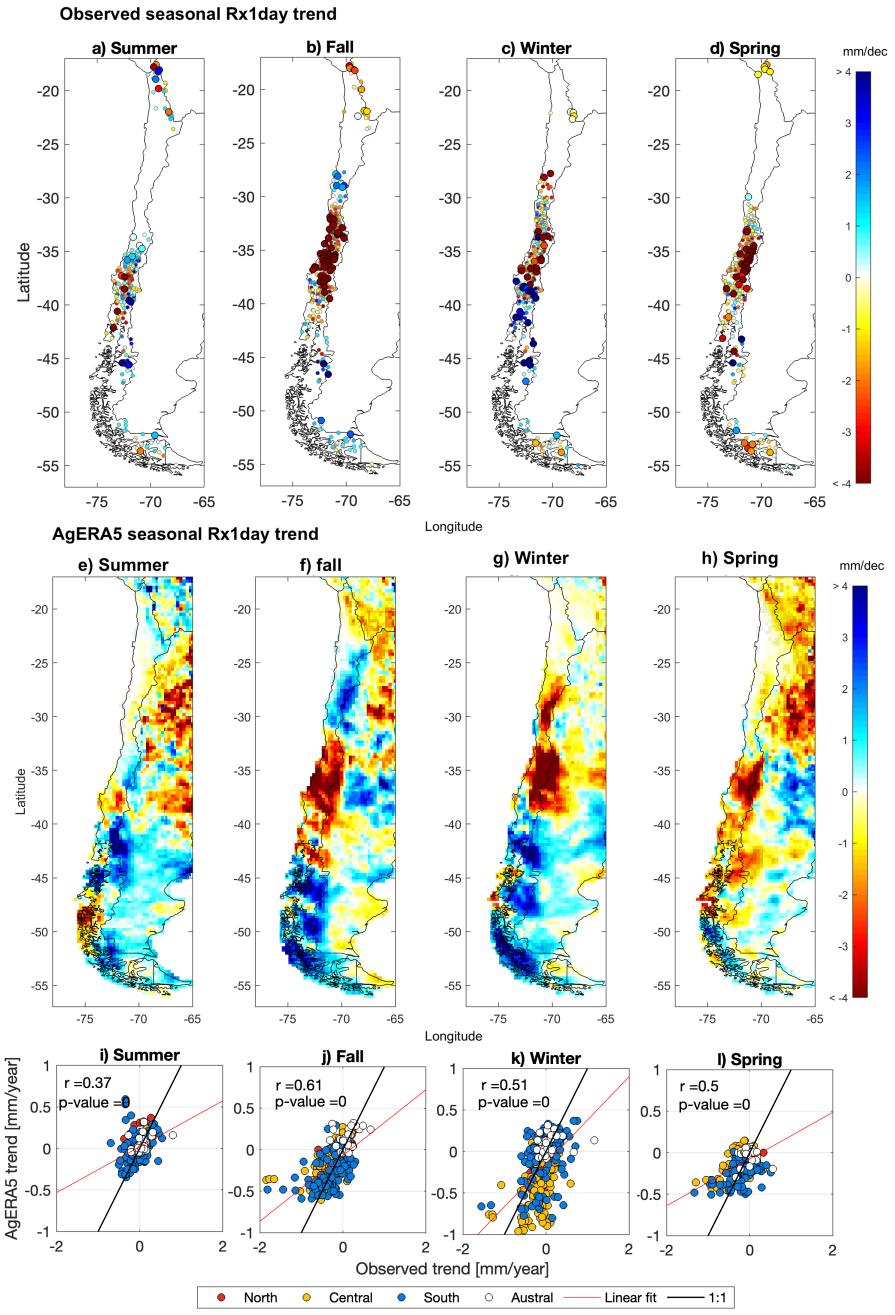

Figure 2.2: Sen's slope for (a-d) observed and (e-h) AgERA5trends in seasonal Rx1day [mm/dec]; and (i-l) relationship between AgERA5 and observed trends (1979-2017). The results are stratified for (a,e,i) summer (DJF), (b,f,j) fall (MAM), (c,g,k) winter (JJA), and (d,h,l) spring (SON). Larger circles (a-d) and dotted surfaces (e-h) denote statistically significant trends at a 90% confidence level. Text r and p-value in panels (i-l) are Pearson correlation and p-value between observed and AgERA5 trends.

2.4.2 Temperature trends for seasonal Rx1day events

The trend analysis over Tn during seasonal Rx1day events reveals between 20 and 36 stations with statistically significant trends in winter and summer, respectively. In the case of Tx trends, these numbers vary from 17 to 28 during the fall and spring seasons. The latter represents more than 16% of the analyzed stations. Surprisingly, a dominant cooling trend pattern arose from north of 33°S; in the South and Austral regions, a warming trend appeared > 2°C/dec. Another significant warming trend is observed for three stations around 30°S during winter; the latter may have substantial implications in meteorological risk as the most significant amount of precipitation is observed during this season (Fig. 2.3a-d). The observed Tn trends during seasonal Rx1day can be approximated to trends in isotherms ranging from -34 m/dec to 34/m/dec. Interestingly, similar patterns arose from Tx trends, except for the South and Austral regions, where a regional cooling is evident for all the seasons (Fig. 2.3e-h).

2.4.3 Temperature scaling

The results in Fig. 2.4 show that seasonal Rx1day scales positively with Tn mostly between 33 and 40 °S in almost all seasons. During winter, sensitivities are similar to the CC scaling ($\sim 7\%/°C$) in the same region; however, larger sensitivities (also known as super-CC, e.g., Lenderink et al. 2011) are observed in the intermediate seasons fall, and spring. We found negative scaling prominently during the fall season in all the regions and in the winter around 30°S (Fig. A.7b,c), which has been explained by Lenderink et al. (2011) and Molnar et al. (2015) for the constraining of vapor availability for precipitation in arid conditions during these events; however, this must be verified.

2.4.4 Radiosonde variations for thermodynamic variables during seasonal Rx1day events

We examined possible temporal variations in H_0, PW, CAPE, and CIN during wet (Pr > 1 mm) and dry days (Fig. 2.5), considering two consecutive climatological periods (each with the same length). The results show more precipitable water in Antofagasta in 1996-2017 compared to the first period 1973-1995 (1.6 mm on wet days, Fig. 2.5, Table 2.2). No evident variations arose in the interquartile distribution of PW for the other stations and periods on wet and dry days. Additionally, a pronounced increase in H0 during wet days has been observed in Antofagasta ($\sim$150 m median, 500 m for the first quartile), while no apparent changes are detected for the remaining sounding stations if data is stratified into wet and dry days. The results in Table 2.2 summarize the Wilcoxon rank test to identify changes in different periods during dry and wet days in PW, CAPE, CIN, and H_0. The analysis reveals a clear trend towards more convective inhibition in all stations during dry days, a decrease in CAPE at Antofagasta, Quintero/Santo Domingo, and Punta Arenas, and less PW (< 2 mm) during dry days. Finally, a significantly lower freezing level ($\sim$-108 m) for all days is detected in Punta Arenas compared to the 1976-1996 period. During seasonal

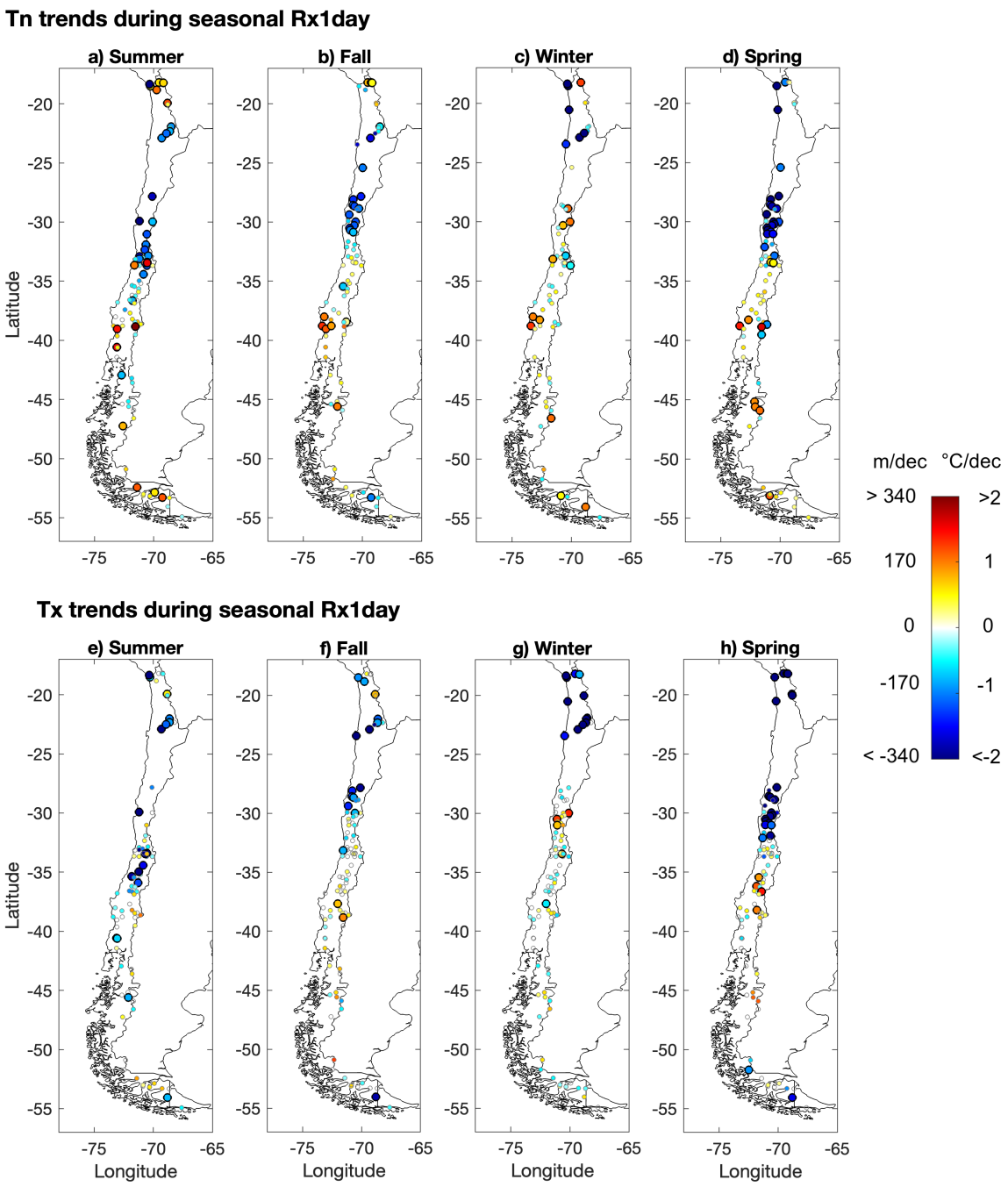

Figure 2.3: Same as in Fig. 2.2, but for Tn (up) and Tx (down) during seasonal Rx1day. Units in [°/*dec*] and [m/dec]

Rx1day events, additional trends were calculated for H_0 and PW. However, no definitive conclusions could be drawn due to the lack of statistical significance, except for Quintero during fall and spring, where the PW trend is up to 3.5 mm/dec (see Table A.1, Fig. A.8).

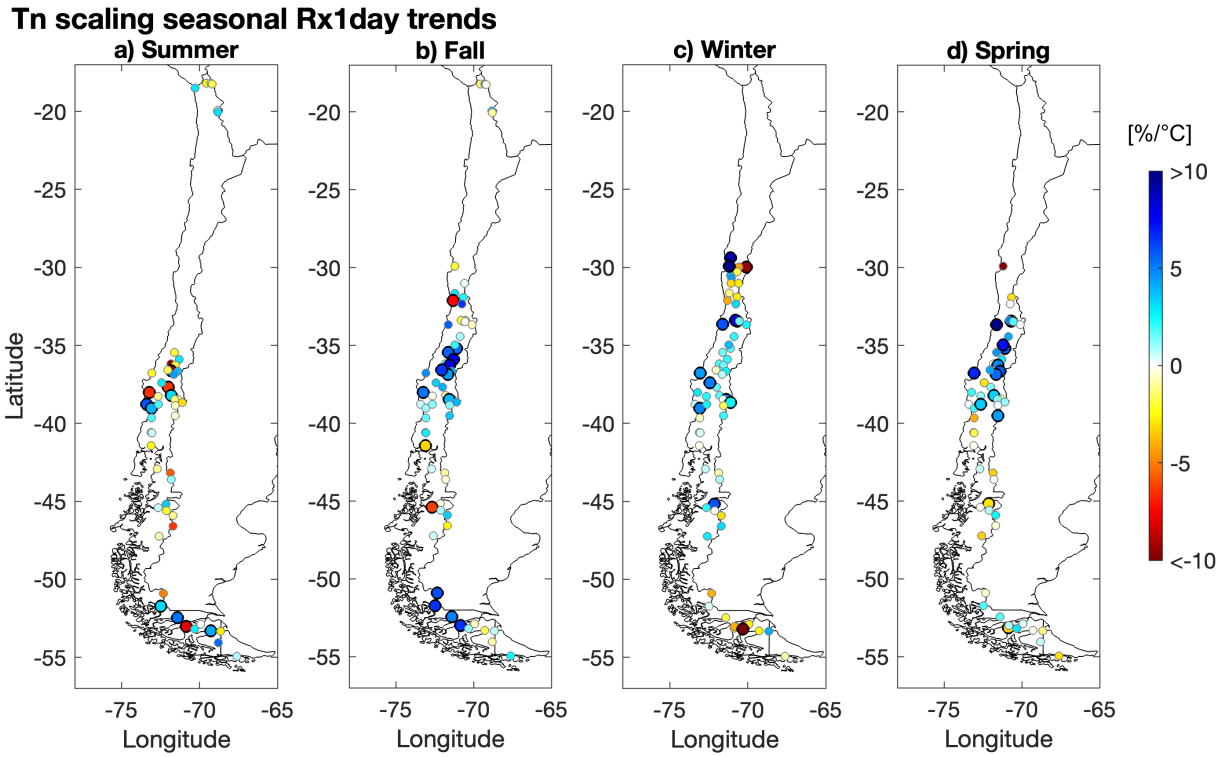

Figure 2.4: Sensitivities of seasonal Rx1day to Tn variations from 1979-2017 [$\%/°/C$].

The trends in upper air temperatures reveal an instability trend during dry days at Quintero due to surface warming (up to 0.5 °C/dec in Quintero between 900 and 800 hPa) and low-level cooling (>-0.5 °C/dec) during the period 1973-1999 (Fig. 2.6). Santo Domingo station showed a stabilization condition due to warming in the upper troposphere during dry and wet days (Fig. 2.6c). In Punta Arenas, enhanced warming in low levels (600-500 hPa) was detected compared to cooling trends near the surface. However, fewer observations were available in Punta Arenas, so these trends do not necessarily represent the analyzed period. Enhanced warming at mid-levels (600-500 hPa, compared to the surface) was found in Antofagasta (Fig. 2.6a); conversely, statistically significant cooling was detected in Puerto Montt during dry days (Fig. 2.6f). The surface temperature trend at the nearest meteorological station from radiosonde (triangles in Fig. 2.6) did not match the magnitude of the lowest level trend estimated by radiosonde, except in Santo Domingo and Puerto Montt (Fig. 2.6c,d). These results agree with the annual trends reported by Burger et al. (2018).

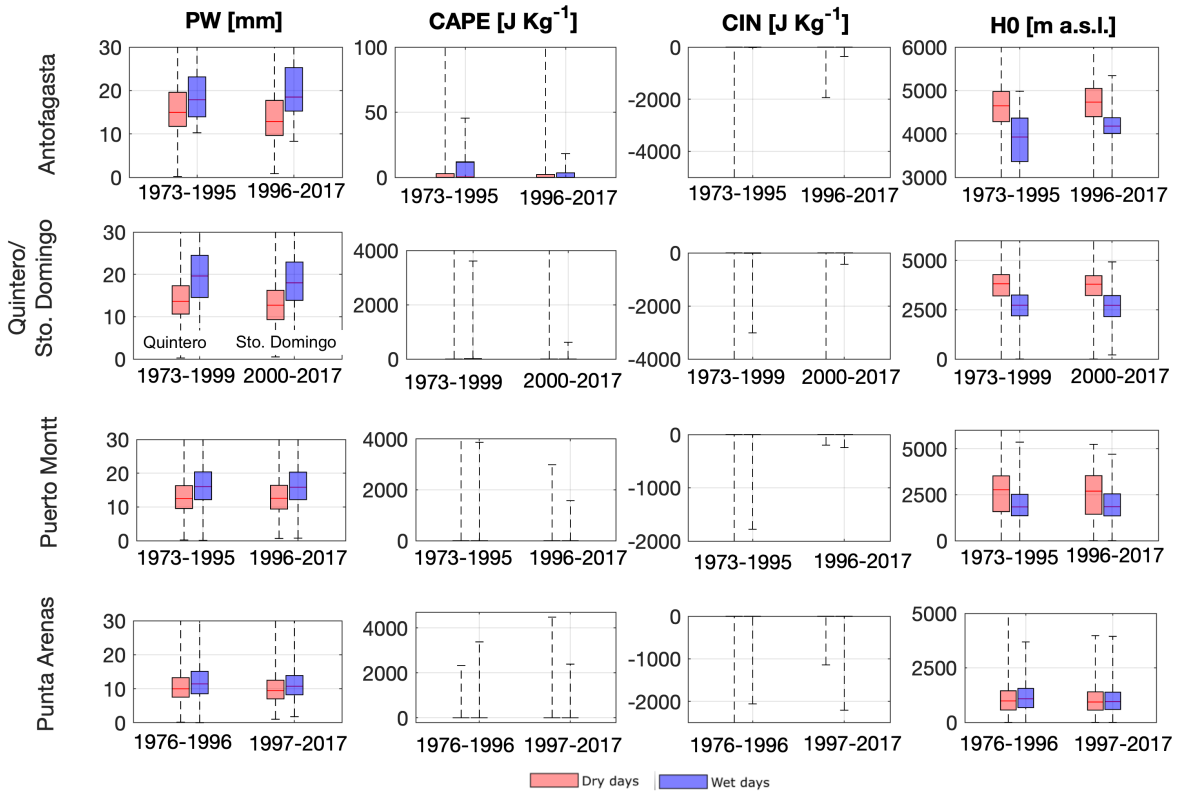

Figure 2.5: Comparison of daily observations of PW (mm), CAPE (J kg^{-1}), CIN (J kg^{-1}), and H_0 (m a.s.l.) obtained from sounding observations during dry and wet days in two periods. The ranges of observed values in all panels were chosen to maximize the distinction of the boxplots or ranges. In the case of CAPE and CIN, the interquartile range is zero.

2.5 Discussion

2.5.1 Trends and scaling relationships

The results presented here unveil three main regional trends in seasonal Rx1day: i) positive trends in summer Rx1day events over the Chilean Altiplano and fall events across 25-30°S; ii) negative trends (i.e., drying) in almost all seasons across central and southern Chile; and iii) intensification in almost all seasons across the Austral region. These patterns align well with previous studies (Souvignet et al., 2012; Schumacher et al., 2020b), and some of them are well captured by the AgERA5 product, especially between fall and spring ($r > 0.5$, Fig. 2.2).

The strongest temperature scaling to enhanced seasonal Rx1day was found between fall and spring in the 33 to 40°S region (2.8 %/°C on average), with the nearest CC scaling (i.e., ∼7%/°C) observed during the winter. Super CC scaling arose in the fall and spring in the foothills of the Andes. The positive scaling during intermediate seasons may be associated with enhanced convective activity, as reported by previous studies for convective

Table 2.2: Changes in mean upper air sounding observations for the Wilcoxon rank-sum test, computed as the differences between 1997-2017 and 1976-1996 averages. The numbers in parentheses show the p-values of the test. Red (blue) indicates statistically significant negative (positive) trends.

Change in Variable		Antofagasta	Quintero/ Santo Domingo	Puerto Montt	Punta Arenas
PW [mm]	Wet days	1.6 (0.723)	-1.4 (0.002)	-0.2 (0.296)	-0.7 (0)
	Dry days	-1.8 (0)	-1.3 (0)	-0.1 (0.999)	-0.5 (0)
CAPE [J Kg-1]	Wet days	-5.2 (0.296)	-40.7 (0)	-11.0 (0.684)	-5.1 (0.040)
	Dry days	-21.8 (0.002)	-24.4 (0)	-14.9 (0.488)	-8.1 (0)
CIN [J Kg-1]	Wet days	-27.0 (0.188)	27.4 (0.003)	5.7 (0.512)	2.3 (0.059)
	Dry days	12.6 (0)	9.0 (0)	12.3 (0.008)	5.9 (0.027)
H_0 [m]	Wet days	262.3 (0.228)	-25.1 (0.433)	18.1 (0.575)	-108.3 (0)
	Dry days	194.3 (0)	42.9 (0.101)	-62.1 (0.133)	-15.1 (0.039)

precipitation events (Hardwick Jones et al., 2010; Lenderink et al., 2017; Mukherjee et al., 2018; Guerreiro et al., 2018; Aleshina et al., 2021; Fowler et al., 2021).

2.5.2 Possible mechanisms

To seek reasons behind the observational trends detected in continental Chile, we looked for climatological trends in seasonal PW and CAPE simulated by the ERA5 reanalysis over the 1979-2017 period. The results for PW indicate an increase in summer and fall moisture along the Pacific coast north from 30°S and drying trends in most continental Chile for all seasons, with the largest magnitudes (∼-1 mm/dec) between 25-35°S (Fig. 2.7a-d). The atmospheric drying south of 30°S aligns well with the observed poleward expansion of the Hadley circulation Cell (e.g., Hu and Fu, 2007; Hu et al., 2011); additionally, the subsidence zone has shifted poleward and, consequently, dryer conditions have been observed, aligning well with projected climate change impacts (He and Soden, 2017). The negative trends in PW across continental Chile agree with those detected in seasonal Rx1day. In contrast, the positive trend of PW in the north Pacific Coast may explain the positive trends of seasonal Rx1day seen with observations and the AgERA5 product during the fall season (Fig. 2.2). Inconsistencies between observed trends in PW (sounding) and ERA5 might be explained by the spatial representativeness of observations (probably more representative of inland sites) and changes in measurement techniques and radiosonde technologies (Elliott and Gaffen, 1991); in particular, radiosondes overestimated water vapor before 1987, especially in dry regions as Antofagasta (Ross and Gaffen, 1998).

The trend analysis of CAPE (Fig. 2.7e-h) reveals an intensification of convective instability on the Pacific coast north from 35°S, which could trigger more convective precipitation over the continent. During fall, strong positive trends in CAPE are detected over the Altiplano and positive trends over the northern coast and the western Andes between

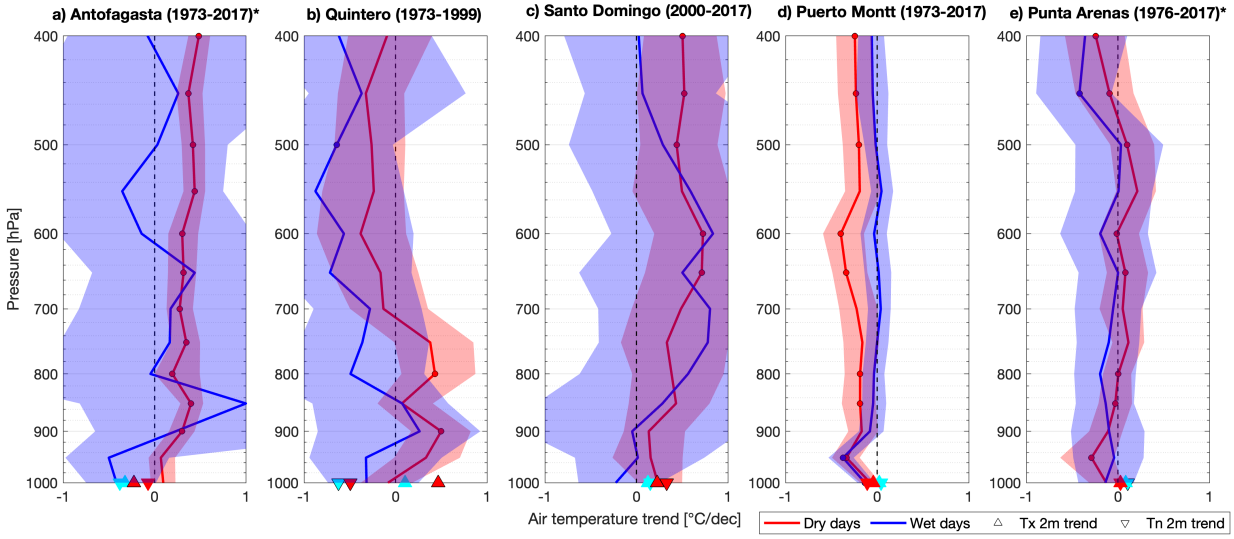

Figure 2.6: Air temperature trends (°C/dec) for radiosonde stations during wet and dry days (red and blue lines). (*) stands for fewer available records per year in comparison to other stations (Figure A.6). Cyan triangles: wet days, red triangles: dry days, circles, and black-contoured markers indicate statistically significant trends. Shaded areas show the confidence interval of the sounding trends (90%)

35-42°S, up to 5 [JKg^{-1}/dec], during summer and fall (Fig. 2.7e,f). Negative trends of CAPE north of 40°S may contribute to explaining the detected trends in winter and spring Rx1day in continental Chile (Fig. 2.7g,h), in agreement with Taszarek et al. (2021), strengthening the effect of the subsidence intensification in the subtropics and the expansion of the Hadley Cell (He and Soden, 2017; Hu et al., 2011). In general, very few historical soundings at 12 UTC (8 Chilean local time) have surface CAPE or CIN, probably due to the lack of buoyant energy at that time of the diurnal cycle, so no general conclusions could be drawn.

If the CAPE trends detected for the warm season project for the next decades along with increasing PW, severe socio-economic damages are expected due to more intense precipitation events during summer or fall, which, in addition to the increase in temperature during seasonal Rx1day, and the rising in H_0 up to 334 m/dec (Fig. 2.3) may trigger landslides and floods (Viale and Garreaud, 2014; Bozkurt et al., 2016; Somos-Valenzuela et al., 2020). Hence, infrastructure design and adaptation strategies should be revisited considering climate change projections for this domain (Vicuña et al., 2021), which are expected to impact the precipitation phase with higher freezing levels (Mardones and Garreaud, 2020) and, therefore, larger rainfall volumes (e.g., Lagos and Vargas, 2014; Ortega et al., 2019). Another striking feature is the intensification of CAPE during fall between 34°S and 40°S during the tornado season in southern Chile (Vicencio et al., 2020), which may lead to an increased frequency of these events. Finally, the CAPE intensification during summer and fall may influence the development of wildfires between 30-40°S (Potter and Anaya, 2015).

The trend analysis of SST during the period 1979-2017 (Fig. 2.8) reveals a hot spot in the Western Pacific (20-40°S, 170-140°W), previously reported by Garreaud et al. (2021), and a

cooling zone along the western coast of South America, more pronounced during winter and spring. The results also show a statistically significant cooling trend in SST south of 60°S, reflecting the lower surface pressures and the intensification of the storm track (Boisier et al., 2018b; Chemke et al., 2022); these results align with EKE positive trends (redFigure 9a-d) that explain positive seasonal Rx1day trends during Fall and Winter in the Austral region (Fig. 2.2). Finally, the warming trend of fall SST in the El Niño 3.4 region may contribute to the observed intensification of seasonal Rx1day for the same season across North and Central Chile, in agreement with previously reported teleconnections between SST and precipitation (e.g., Garreaud, 2009; Aceituno et al., 2021) and their implications on extreme events as seen in the Atacama flood at 2015 (Bozkurt et al., 2016).

The EKE trends (Fig. 2.9) reflect weaker or no eddy activity trends between 30-40°S during summer, fall, and winter. Nevertheless, strong EKE trends appeared in the Austral region, reflecting the intensification of waves and storm tracks, which may explain the positive trends in Rx1day events in these latitudes. The AR trends only showed an intensification in frequency up to 2 days/dec during spring (Fig. 2.9h), but fewer AR days between summer and winter south of 35°S, in agreement with Ma et al. (2020). The joint decrease of ARs, and EKE in mid-latitudes, may explain the negative observed trends in extreme precipitation events along central and southern Chile. However, aspects such as their duration and intensity of moisture flux may also be included in future analysis as they have been shown to strongly influence the magnitude of precipitation (Campos and Rondanelli, 2023).

Based on the above evidence, we hypothesize that the following mechanisms may explain the shifts in seasonal extreme precipitation across Chile.

i The intensification of northern summer Rx1day events may be associated with higher SST and more water vapor supply on the Pacific coast, favoring stronger precipitation.

ii The negative trends in seasonal Rx1day in central Chile could be explained by the combination of the Hadley Cell expansion (Hu et al., 2011) and the circulation induced by the SST Southern Blob, an unusually warm sea region east of Australia and New Zealand that is associated with drier conditions in Central Chile (Garreaud et al., 2021), in addition to the negative trends in ARs frequency.

iii The intensification in seasonal Rx1day across the southern and Austral regions can be associated with the South Pacific Pressure trend dipole and its impacts on the southern hemisphere storm track (Chemke et al., 2022), observed in the EKE trends, which may have more substantial impacts on extreme precipitation than the detected instability inhibition in this region.

2.5.3 Limitations and future work

This work did not address possible uncertainties in high-elevation observation due to precipitation undercatch. Most rain gauges installed along the Chilean Andes are conventional and lack windshields despite the exposure to high wind speeds and solid precipitation. Although the bias correction factor has been estimated to vary between 1.2 and

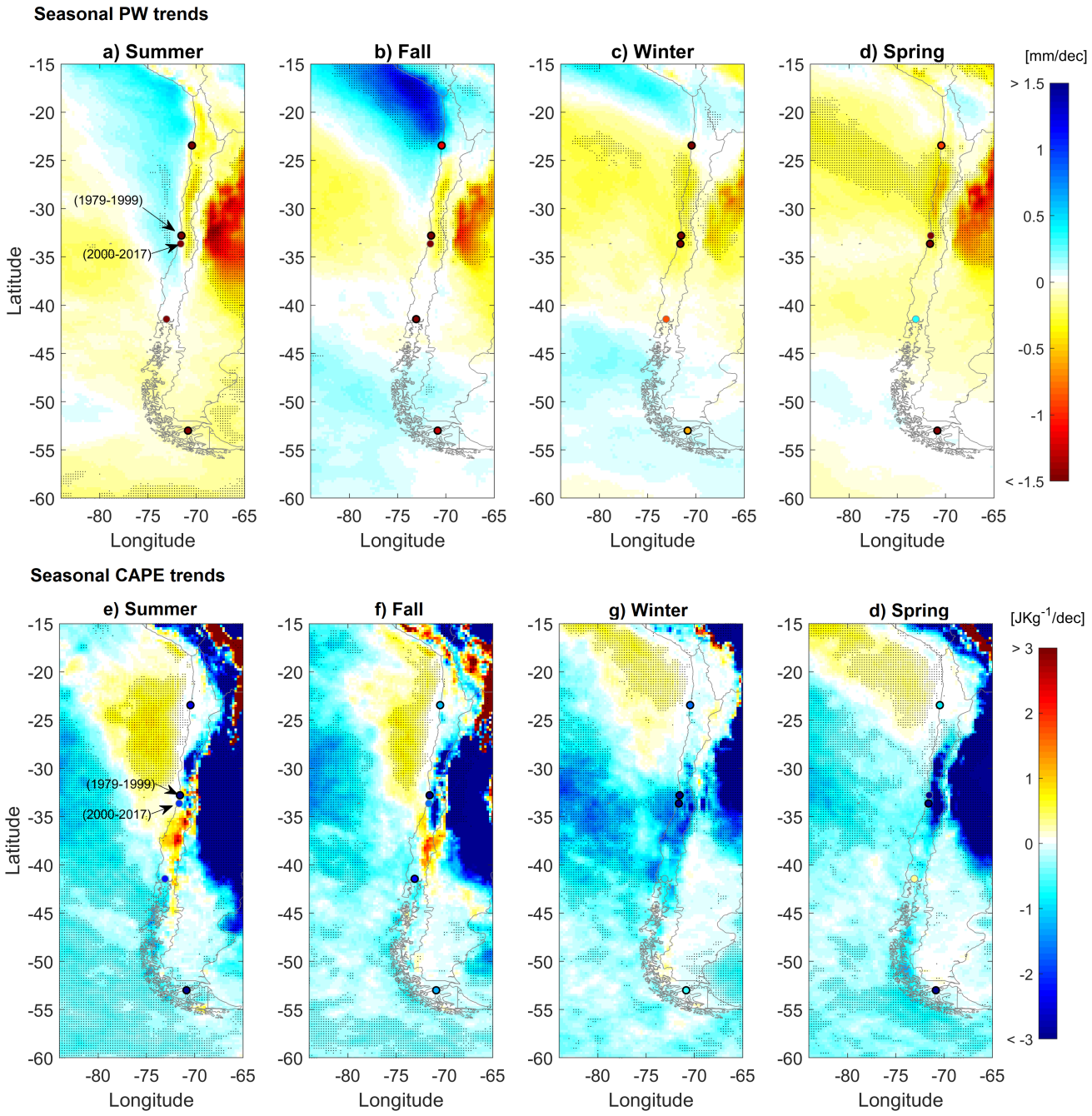

Figure 2.7: (a-d) Trends for seasonal precipitable water [mm/dec] (e-h) Trends for CAPE [J Kg^{-1}/dec] retrieved from monthly averaged ERA5 reanalysis for the 1979-2017 period. Shadowed surfaces denote statistically significant trends. Sounding station trends are shown in circles, and the black-contoured circles stand for statistically significant trends.

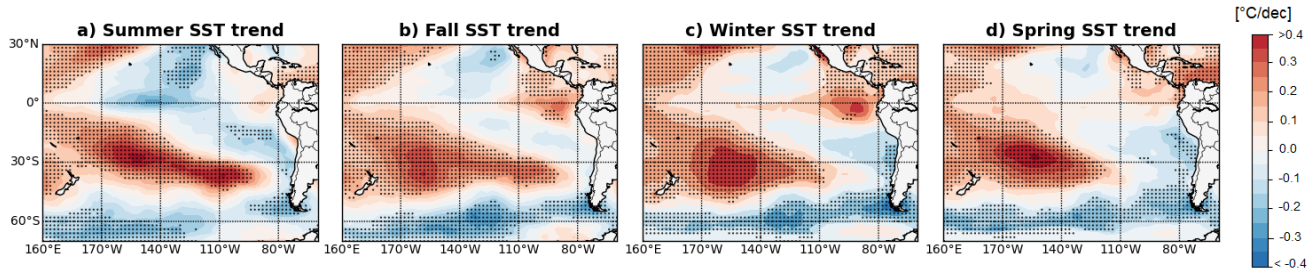

Figure 2.8: Seasonal SST trends from 1979-2017 [°/*dec*]. Circles denote statistically significant trends

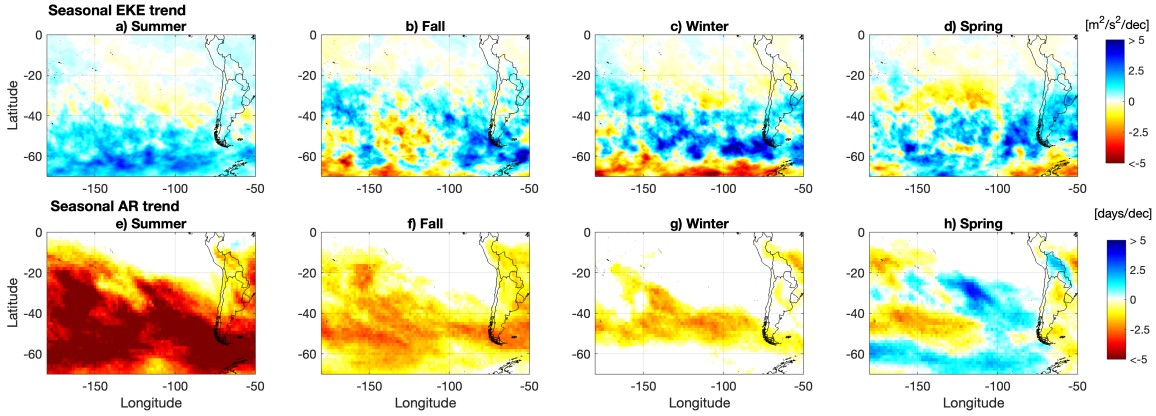

Figure 2.9: (a-d): Seasonal EKE trends from 1979-2017 $[m^2/s^2/dec]$ retrieved from ERA5 reanalysis; (e-h) seasonal AR trends from 1979-2014 [days/dec] retrieved from Guan and Waliser (2015).

3 (Beck et al., 2020), we did not correct observed precipitation data due to the lack of in-situ temperature observations in all Pr stations. Hence, the intensification of seasonal Rx1day detected in mountain stations could be attributed to measurement artifacts, i.e., warmer temperatures allowing the current weather network to measure total precipitation amounts that decades ago could not be captured due to their phase (i.e., snowfall). A more reliable gridded meteorological product is needed to generalize the detected temperature trends during seasonal Rx1day. Even the station-based gridded product CR2METv2.5 (Boisier et al., 2018a; DGA, 2017; Alvarez-Garreton et al., 2018) did not show better performance in temperature trends than AgERA5 during seasonal Rx1day (not shown), which remains a challenging issue in the Andes.

Further analyses are needed for temperatures associated with seasonal Rx1day, and the results presented here are only generalizable to some regions due to the low and sometimes even negative correlations between observations and the AgERA5 product (not shown). To draw more robust conclusions regarding temperature influence in EPEs, more stations and longer records are needed in conjunction with more humidity observations to analyze Clausius-Clapeyron relationships and sub-daily records in precipitation stations. Our CC scaling approach is not comparable with other studies due to the small number of events considered per station (40 events/season), which provided very sensitive (and even contradictory) shifts in the signal change (i.e., from positive to negative and vice versa), depending on the number of bins and extreme daily temperature selected. Further, most regional studies aggregate significant events and stations within a domain (e.g., Lenderink et al., 2017; Fowler et al., 2021). Because of the above reasons, our scaling results should be interpreted with caution; for example, the combination of coastal cooling and drying signal in central Chile led to a strong positive Tn scaling that could be misinterpreted as seasonal Rx1day intensification in the context of an expected future warming signal (Araya-Osses et al., 2020; Vicuña et al., 2021; Lagos-Zúñiga et al., 2022a), contradicting the observed negative trends in that region. The detected trends in extreme temperature may lead to a rise in H0 during warmer climates up to 34 [m/dec]; however, the used lapse rate of 5.9°C/km is only representative for the Andean region around 33°S (Ibañez et al., 2021; Lagos-Zúñiga et al., 2021c) and needs to be better analyzed in different latitudes due to thermodynamic and dynamic constraints and gradients along the country, such as the extreme dryness in the north, and the storm track in higher latitudes.

2.6 Conclusions

We have examined trends in seasonal precipitation extremes over continental Chile and their associated maximum and minimum daily temperatures. Although statistically significant trends (90% confidence) were detected in only 12% of the stations analyzed, we found clear patterns of intensification in precipitation extremes between 25-30°S during fall, followed by less intense seasonal daily maximum precipitation in central-southern Chile. Additionally, we detected an intensification of seasonal Rx1day for South Chile during winter and in the Austral region in almost all seasons. Most of these spatial trends were also detected using the

AgERA5 product during all seasons (p-value < 0.05). The strongest trends are $\sim$4 mm/dec in the Altiplano (summer) and around 30°S during fall, while the most negative signals were found at $\sim$38°S between fall and spring (< - 4 mm/dec).

We found cooling trends in Tn and Tx during seasonal Rx1day north of 30°S ¡ -2°C/dec in the Pacific Coast during spring and winter, while positive trends around 30°S during winter and south of 38°S ($\sim$1 °C/dec) for almost all seasons at the minimum temperature. These warming trends in the South and Austral regions, in addition to orographic enhancement, may increase runoff in contributing areas due to higher freezing levels of up to 334 m/dec, and additionally, less water supply in the warm seasons due to less snow accumulation in the Andes.

We found positive trends in precipitable water in the Northeastern Pacific and negative trends around central Chile. The latter may be associated with the poleward shift of the Hadley Cell, the South Pacific Trend Dipole, the Southern Blob, and less frequent Atmospheric Rivers reaching these latitudes. These mechanisms affect not only annual precipitation but also extreme events. We found an intensification of sea surface temperature near the coast of Peru, which may be triggering the humidification of the northern Pacific coast of Chile during the warm seasons. The positive trends in seasonal Rx1day in Southern and Austral Chile can be attributed to the observed intensification of the southern storm track (reflected in the intensification of Eddy Kinetic Energy activity and related synoptic-scale phenomena), but also to greater atmospheric instability and more water vapor available due to generally warmer conditions.

Although no significant trends were detected for CAPE and CIN from radiosondes, we found climatological variations in the frequency and a trend towards a more unstable atmosphere in Quintero and Puerto Montt during wet days (Pr > 1 mm), but the overall trend is towards a more stable atmosphere due to warmer trends in high levels compared to the surface during dry days. Nevertheless, the ERA5 reanalysis reveals an intensification of CAPE during summer and fall in Southern Chile, the Bolivian Altiplano, and high-elevated areas in the Central Andes (summer). The latter effect should be investigated in detail because of the risk in convective precipitation events and their consequences on flooding and landslides observed worldwide.

Chapter 3

Regional Climate Models projection for seasonal extreme precipitation in the extratropical Andes

This chapter prepared by the authors Miguel Lagos-Zúñiga and Roberto Rondanelli, as submitted to Geophysical Research Letters

Abstract

The Andes Cordilleras ecosystems are threatened due to climate change. Still, it is also one of the regions with broader uncertainties in the precipitation change in regional and Global Climate Models (GCMs). This study explores the thermodynamic impact of the spread of climate change projections of seasonal and maximum daily seasonal precipitation (Rx1day), simulated by ten Regional Climate Models (RCMs) and their driving GCMs through the Potential Instability approach. Our results show a shift in precipitation seasonality and opposite signals between seasonal precipitation and seasonal Rx1day. We found that the robustness of precipitation change in this region is low, unlike the strong drying trend portrayed by GCMs that is observed just between 30-35°S in regional and global simulations (∼-20%). We found that the rise in precipitation is related to enhanced instability due to water vapor contribution (> 7%/°C), except for wintertime occurrences.

Plain Language Summary During the last decades, global and regional climate models at coarse resolution for the Andes Cordillera have projected a robust drying signal for precipitation on the western slope and some moistening on the eastern slope. The last CORDEX and Regional Climate Models (RCMs) simulations in South America confirm the drying signal in the extratropical Andes; however, recent analysis of extreme and mean precipitation has shown some intensification in the subtropical Andes without an explanation of the mechanisms beyond these changes. With this motivation, we analyze ten RCMs simulations from: i) the CORDEX initiative: REMO2015 (3) and RegCM4.7(3) at 0.22°, ii) The Eta model (3) at 0.2°, and iii) RegCM4.5 at 0.11°. We analyze seasonal changes in precipitation and maximum one-day precipitation (Rx1day) in the 15-30°S region and derivate a scaling analysis of changes in potential instability for troposphere heating and increase in near-surface air humidity between the 2031-2060 and 1976-2005 periods at the RCP8.5 scenario. Our results reveal opposing changes between seasonal and extreme precipitation. The increase in precipitation may be explained by enhanced convection in the subtropical Andes; however, a large spread remains between RCMs and GCMs. Reduced uncertainty is shown at 30-35°S, where synoptic activity modulates precipitation.

Keywords: extreme precipitation, climate change, regional climate models.

3.1 Introduction

Despite a significant improvement in the Global Climate Models (GCMs), local processes require finer horizontal resolutions than what is provided by coarse simulations. As a consequence, the dynamical downscaling through Regional Climate Models (RCMs; e.g., Dickinson et al., 1986; Giorgi and Bates, 1989; Laprise) is an essential tool to assess local impacts, particularly in topographically complex terrains such as mountains and headwaters (e.g., Prein et al., 2013; Torma et al., 2015; Giorgi et al., 2019; Bozkurt et al.).

In South America, GCMs projections show enhanced summer precipitation and a general decrease in wintertime precipitation in the continent and the southern Andes (Vera et al., 2006; Blázquez and Nuñez, 2013), existing a general agreement among GCMs regarding a dryer trend with warming over the subtropical Andes (Fuenzalida et al., 2006; Demaria et al., 2013; Araya-Osses et al., 2020; Ortega et al., 2019; Vicuña et al., 2021; Martinez-Villalobos and Neelin, 2023; Gutiérrez et al., 2021). These negative projections for precipitation have been confirmed by Regional Climate Models (RCMs, Teichmann et al., 2021; Gutowski Jr et al., 2016); however, there is still low confidence in the projected sign of change compared to other regions.

RCM studies performed over mountain regions have shown an intensification of extreme precipitation in the European Alps (Feldmann et al., 2013; Giorgi et al., 2016; Colmet-Daage et al., 2018; Brönnimann et al., 2018; Kotlarski et al., 2023), the Australian Alps (Grose et al., 2019), the Tibetan Plateau (Na et al., 2021; Lee et al., 2023) and the US Rockies (Wi et al., 2012; Zobel et al., 2018). Reboita et al. (2022) and Lagos-Zúñiga et al. (2022a) reported an increase of daily precipitation over the 95th percentile (p95) and Maximum 5-day consecutive precipitation (Rx5day) in South Western South America (SWS) and North East South America (SES), respectively, particularly in the Western slopes of the Andes and the Pacific coast north of 30°S with a wide spread among the projections.

Enhanced resolution of RCM allows hypothesizing about changes in mesoscale precipitation, e.g., Giorgi et al. (2016), suggests that surface warming in regions with less snow cover and enhanced air moisture (Fischer and Knutti, 2016) may produce more intense precipitation due to higher instability. Additionally, precipitation projections may differ between RCMs and their driving GCM, as shown by the Eta model (Mesinger et al., 2012) in total and extreme precipitation during the austral and winter seasons (Reboita et al., 2022). Simulations performed by Hodnebrog et al. (2022) in South America concluded that using coarse GCMs or RCMs (∼50km) "may give incorrect conclusions about regional-scale precipitation projections", which is confirmed by the studies of Bozkurt et al. (2019) and CR2 (2018) that show a positive precipitation signal for mean precipitation in Chile, using a ∼12 km resolution, contradicting the expected drying storylines for this region (e.g., Pfahl et al., 2017; Li et al., 2021; Martinez-Villalobos and Neelin, 2023).

Although global warming projections show an increase in stability in the tropics and subtropics due to the vertical amplification of warming with height (Manabe and Wetherald, 1975; Ladstädter et al., 2023; Sherwood and Nishant, 2015), the instability in the extratropical Andes might increase due to local surface moistening (He and Soden, 2017; Pfahl et al., 2017). In the context of dynamical drying in subtropics due to the Hadley

cell poleward expansion, the complex interaction at the mesoscale between the unstable large-scale environment and changes in surface moisture warrants a deeper study making use of the higher resolution runs available for these regions to understand the mechanisms behind the uncertainties in the projected precipitation signal (Gutiérrez et al., 2021; Salazar et al., 2024).

Within the provided context, this study aims to analyze the disagreement and causes of signal changes in seasonal and extreme precipitation in the extratropical Andes region (15 – 35°S), simulated by an ensemble of ten RCMs compared to their driving GCMs. We also analyze instability processes and temperature scaling at a seasonal scale to understand the underlying mechanisms behind the projected trends.

3.2 Methods

3.2.1 Seasonal and extreme precipitation change

We analyzed the seasonal precipitation change in ten RCMs and their corresponding driving GCMs. The RCMs come from the CORDEX initiative, Eta simulations, and the high-resolution RegCM4.5 project from Bozkurt et al. (2019). We compare the intermediate future 2031-2060, in the RCP8.5 scenario, with the historical period 1976-2005 as a percentage change in 1) seasonal precipitation and 2) seasonal maximum daily precipitation (Rx1day). To generate an ensemble mean of RCMs and GCMs, we performed a bilinear interpolation to a common 0.22° and 0.75° grids for regional and global models using the Climate Data Operator software (Schulzweida et al., 2019). A climate change signal was considered robust when: i) the three GCMs, agreed on the sign of change for each GCM (Eta, RegCM4.7 and REMO2015), ii) 70% of models have the same sign of change (7 out of 10) models for the RCMs ensemble and iii) 67% of models agreed in the sign (4 out of 6) in the case of the GCMs ensemble.

To facilitate the analysis of the projections, we made a comparison for seasonal Rx1day in four latitudinal bands: Far North (15-20°S), Near North (20-25°S), Central North (25-30°S), and Southern Central Andes (30-35°S). We also grouped the simulations for each RCM, displaying the mean of the projections as a reference.

3.2.2 Potential Instability temperature scaling

We use the Potential Instability Index,

$$PI = \theta_{e500} - \theta_{e850} \tag{3.1}$$

used by Giorgi et al. (2016) to elucidate changes in seasonal and extreme precipitation associated with convective precipitation. In Eq. 3.1 θ_e is the equivalent potential temperature, and the numbers indicate pressure levels at 500 hPa and 850 hPa. Negative values of PI denote a potentially unstable troposphere.

The relative impact of different processes in the PI can be derived using the approximation of θ_e, where $\theta_{e850} = \theta_{850} exp(L_v r / c_p T)$, L_v is the latent heat of vaporization, θ is the potential temperature, r is the mixing ratio, T is the air temperature, and c_p is the heat capacity of air at constant pressure. Neglecting the water vapor supply at 500 hPa we can approximate $\theta_{e500} \approx \theta_{500}$. When r is small, using the Taylor series expansion $exp(x) \approx 1 + x$, when x is small, we can approximate θ_{e850} to as

$$\theta_e(850) \approx \ \theta(850) + \frac{L_v r_{850}}{c_p} \left(\frac{p_0}{850}\right)^{R/c_p} \tag{3.2}$$

and therefore, PI can be approximated to

$$PI \approx \theta(500) - \theta(850) - \frac{L_v r_{850}}{c_p} \left(\frac{p_0}{850}\right)^{R/c_p} \tag{3.3}$$

where p_0 is the reference atmospheric pressure (1000 hPa), and R is approximated to the dry air constant. Using the derivation of Bohren and Albrecht (1998), $\beta \equiv L_v/c_p(p_0/850)^(R/c_p)$ is approximately constant, except for a slight dependency with air temperature. Therefore, the rate of change of PI with surface temperature T_s, can be estimated as

$$\frac{\Delta PI}{\Delta T_s} \approx -\frac{\Delta\theta_{850} - \Delta\theta_{500}}{\Delta T_s} - \beta \frac{\Delta r_{850}}{\Delta T_s} \tag{3.4}$$

The first term on the right-hand side of Eq. 3.4 can be thought of as the change of static stability of the troposphere, including the vertical amplification of warming with height at 500 hPa, and the surface heating at 850 hPa. The term Δr_{850}, reflects the destabilization effect due to enhanced moisture supply due to enhanced moisture supply due to the Clausius-Clapeyron relationship at lower levels or due to changes in the relative humidity. All PI changes are scaled to surface temperature T_s. Negative values of ΔPI are interpreted as more unstable conditions in the future atmosphere compared to the present. We assumed that simulated fields at 850 hPa are representative of the surface even when their terrain elevation is higher than theirs, following the approach of the Alps in Giorgi et al. (2016).

3.3 Data

The regional models used in this study are listed in Table B.1. We considered three simulations from i) RegCM4.7 (Giorgi et al., 2012), ii) REMO2015 (Jacob et al., 2007) at 0.22°[2], iii) Eta at 0.20° (Mesinger et al., 2012), and one simulation with the RegCM4.5 (Bozkurt et al., 2019) at 0.11°. Because of the availability of information on daily fields in the ESGF (2023) portal, we only performed the PI analysis using the RegCM4.7 and Eta simulations on a monthly scale.

[2]RegCM4.7 and REMO2015 simulations are part of the CORDEX simulations

3.4 Results

3.4.1 Seasonal precipitation change

Unlike the results from GCMs, RCM projections do not show a homogenous behavior of seasonal precipitation between the seasons and models. For instance, the CORDEX simulations show a drying signal between 30-35°S within the RCMs analyzed (Fig. **??**a,b,c) for all the seasons with a magnitude between -20 to -30%. In contrast, RegCM4.5 (Fig. **??**d) presents a humid signal during the warm seasons in the same region (>30%) and a drying signal during winter. The increase of seasonal precipitation (Pr) is larger for the Eta simulations during almost all seasons (>30%) north of 30°S and in the Central Southwestern Andes during summer. A positive signal appears in the western Andes between 22-30°S during winter and spring for the REMO2015 simulations (Fig. **??**c, JJA), while RegCM4.7 presents this positive signal to the coastal regions between 15-28°S (Figure 1a, JJA).

The ensemble of the GCMs (Fig. **??**f) presents a decline of precipitation for almost all seasons in all the domains (∼30%), except a positive signal between fall and spring north of ∼25°S. The RCM ensemble mean (Fig. **??**e) presents a robust drying signal south of 30°S with higher decreases in the coast, a positive signal in fall and spring around 28°S, and the region East of the Andes ∼33°S. Compared with their driving GCMs, the RCMs better distinguish spatial patterns of the seasonal precipitation change.

3.4.2 Seasonal extreme precipitation analysis

Fig. 3.2 also shows heterogeneous signals among the RCMs and seasons in Rx1day events. Only for the case of Austral summer, there is a strong positive signal between all models in the western Andes and the coastal region (> 30% on average); however, the negative projections for Rx1day at RegCM4.7 model affect the mean change at the foothills of the Andes (Fig. 3.2a-f, DJF). Similar results arise for the spring between 30-35°S, mainly centered in the coastal region influenced by the REMO2015 simulations and, additionally, the Altiplano (a geographical region near the limits of Chile, Bolivia, and Argentina, Fig. 3.2a-f, SON). Positive signals also appear at the CORDEX simulations at ∼33°S (10-20%, Fig. 3.2a,c) during fall and winter. A robust negative signal appears for the coast of Chile in the fall season (15-24°S) in the coarser RCMs, but some increasing zones appear in the continent in the same period. Specifically, RegCM4.5 projects a substantial intensification in the same region, while RegCM4.7 ensemble-mean projects a strong drying signal (Fig. 3.2a,d, MAM).

The GCM ensemble mean for Rx1day events presents a strong positive signal (∼15%) in the coastal regions between 28° and 35°S during the fall and spring seasons (Fig. 3.2f). The spatial heterogeneity of projections is evident when analyzing the regional simulations, while the GCMs provide more agreement between the global models. The difference of projections in coastal v/s Andean regions, or west and east of the Andes, is strongly dependent on the model and the season, as can be seen in the REMO2015 simulations for austral winter (Fig. 3.2c, JJA), where a positive to negative gradient appears from the Pacific Coast to Argentina. This local aspect at finer spatial resolution is not captured but presents a general pattern of

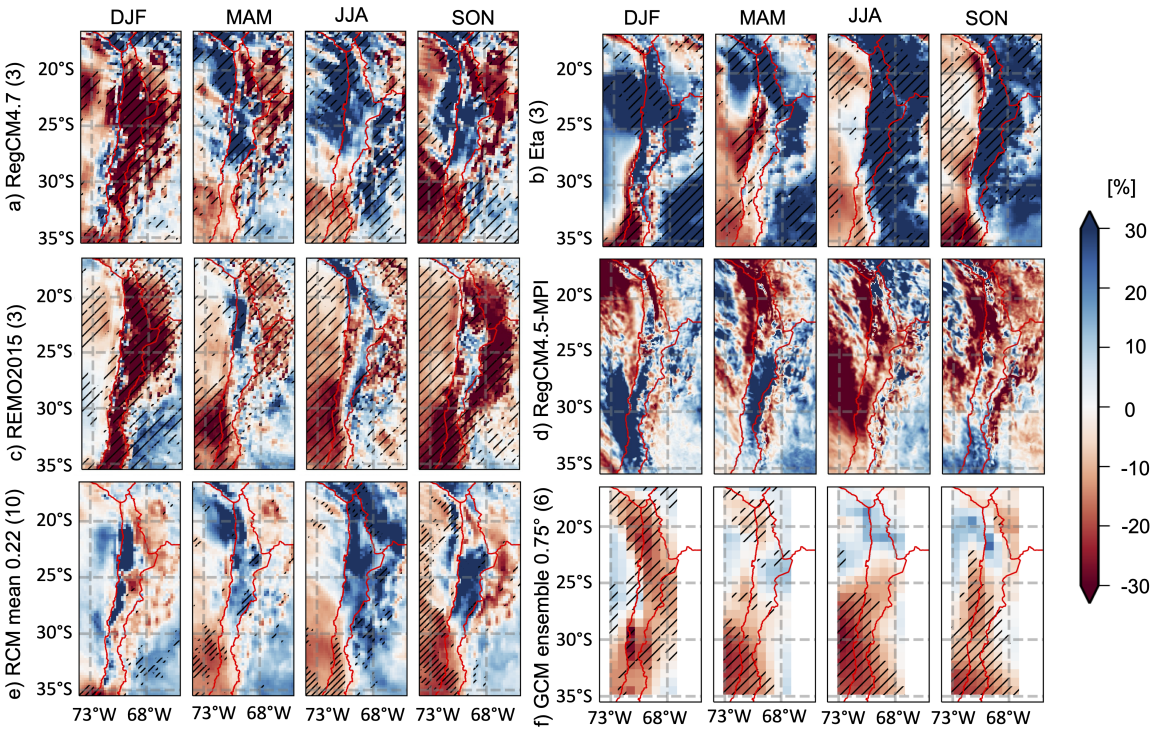

Figure 3.1: Seasonal change of precipitation between periods 2030-2060 and 1976-2005. Row panels show different RCM ensembles, and columns show the different seasons. Panel e) Shows the mean change of 10 RCMs regridded to 0.22° and e) Shows the ensemble mean of the 6 GCMs forcing the different RCMs (see Table 1 for details). Dashed lines denote that all models agree in the sign of the change in panels a-c). In e) (f), the change agreement is computed to seven (four) of ten (six) models.

more intense Rx1day events west of the Andes and a negative signal in the Eastern Andes (Fig. 3.2f, JJA).

When analyzing the cross sections for the latitudinal bands (Fig. 3.3), an evident spread pattern arises for Rx1day events within the RCMs, generally from the whole positive to negative ranges. An intensification of Rx1day events is more substantial between fall and spring in the Central-South region, i.e., the extratropical Andes, where all RCMs except the RegCM4.5, project increases in these events in the western slope of the Andes, up to 40%/°C for the CORDEX models (Fig. 3.3d, red boxes, MAM to SON). In the Near-North region (20-25°S), the CORDEX simulations also show an intensification in summer events at the western slope of the Andes (Fig. 3.3b, DJF, dashed line box). Notably, the projection spread for the Eta simulations is generally more prominent than the CORDEX models; however, even with the same GCM forcings, within the CORDEX simulations, the change signal can significantly differ between RCM (e.g., Fig. 3.3b, JJA). An interesting feature is the strong disagreement in the sign of change for Rx1day events between RegCM4.7 ensemble projections (Fig. 3.3, blue-shadowed areas) and the RegCM4.5 model (Fig. 3.3, dashed blue line). For example, in the far north, between summer and winter, the finer resolution model generally has a positive signal for the Rx1day event (15%/°C). Whereas the coarser simulations show negative projections (-20%/°C on average), with large dispersion between members (Fig. 3.3a), pointing to an important role of the horizontal resolution and/or the model schemes (see Tables B.1 to B.3 for details) even within the same family of RCMs and forcing GCM. The comparison between the CORDEX and Eta models exhibits diverse signal changes with a larger projection spread for the last ensemble, especially during the warm and cold seasons (summer and winter). The Eta model consistently projects an increase in Rx1day events during the fall season for almost all the regions between 20 and 35°S (Fig. 3.3b-d, MAM).

After all the analyzed simulations presented in this section, we can summarize:

i. Mean seasonal precipitation changes generally present an opposite signal than the seasonal changes in mean Rx1day events (Figures **??** and 3.2).

ii. The RCMs add value in the sign of change within the coast and Andean domains, providing detailed changes in different sub-regions across the domain compared to the driving GCMs (e.g., N-S and W-E transition zones in Figures **??** and 3.2).

iii. Rx1day simulations present diverging signals within the domain with an incoherent behavior between RCMs. However, some strong signals arise in the summer for the Near and Far North in the west of the Andes. In the Central North and South regions, the RCMs also agree on a positive signal during spring (Fig. 3.3, c-d, SON) and between fall and spring for the Central South region. (Figure 3.3d, MAM to SON).

3.4.3 Potential Instability scaling analysis

When applying Eq. 3.4 (4) to separate changes in potential instability due to changes in warming and moisture, we can see that dry stability changes ($\Delta(\theta_{850} - \theta_{500})/\Delta T_s$) are close

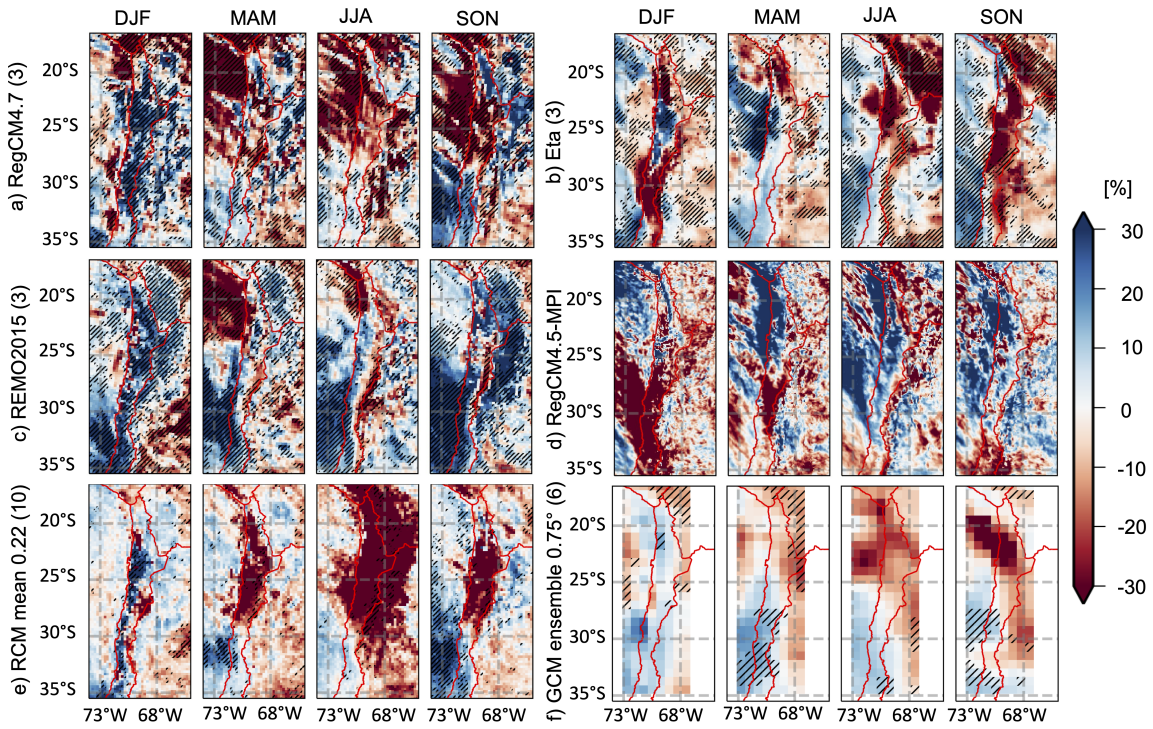

Figure 3.2: Same as in Figure 3.1, but for a seasonal change of mean Rx1day events.

to zero in the continent and along the Andes (Fig. 3.4a, white colors) and reach more stable conditions (Fig. 3.4a, blue tones) over the ocean and in Argentina (25-35°S) during fall and winter in RegCM4.7 and during winter and spring in Argentina for the Eta simulations. The neutral values of dry stability tendency reached in the mountains during all seasons reflect the effect of stronger surface heating that compensates for the tropospheric heating at 500 hPa. The projections of more unstable conditions in dry stability are simulated during summer in the RegCM4.7 (Fig. 3.4a, RegCM4.7 DJF, red colors) at the eastern slope of the Andes and in the Pacific coast around 25°S in the Eta Model (Fig. 3.4a, Eta MAM, red colors). The moisture contribution ($\beta\Delta q_{850}/\Delta T_s$, Fig. 3.4b, red colors) is almost everywhere positive, therefore leading to more unstable conditions in almost all domains and seasons, especially during the summer and fall seasons ($PI < 0$, except for the DJF over the Andes in Fig. 3.4c. RegCM4.7). The stabilization effect is dominated by enhanced warming in the high troposphere during winter and spring on the Pacific coast with a robust signal (Fig. 3.4c, blue tones), and it is closely related to the dry stability tendency during that season (Fig. 3.4a, blue tones).

When aggregating projected changes of the seasonal precipitation at the longitudinal bands, we can appreciate that among the RCMs; there is a coherence between the connection of larger instability and increased precipitation in the far North (15-20°S), i.e., the subtropical Andes, particularly during summer, fall, and spring. This pattern is maintained in some models during spring in the same latitudes (Fig. 3.5a). During the Austral summer, this

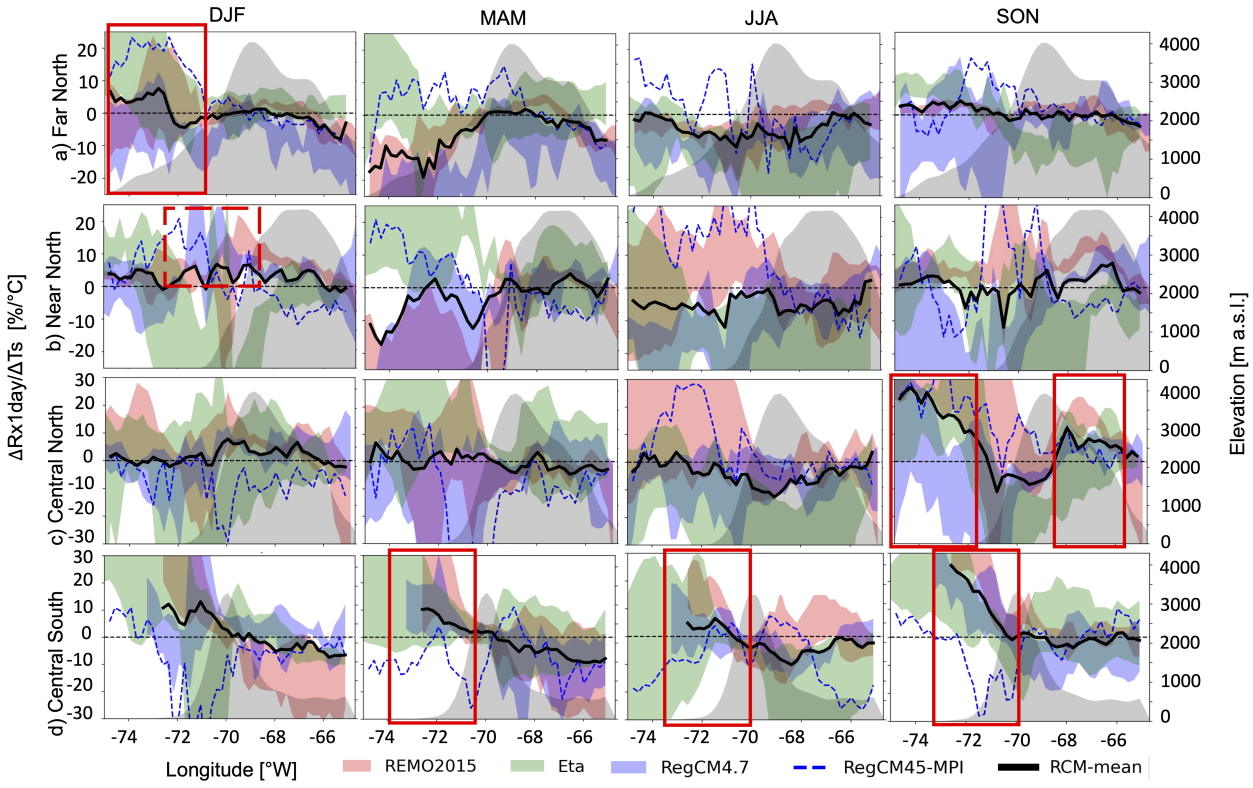

Figure 3.3: Cross sections for seasonal Rx1day change. Rows stand for geographical cross sections and columns for the seasons. The gray-filled area is the mean elevation of the cross sections for 0.22° interpolated elevation.

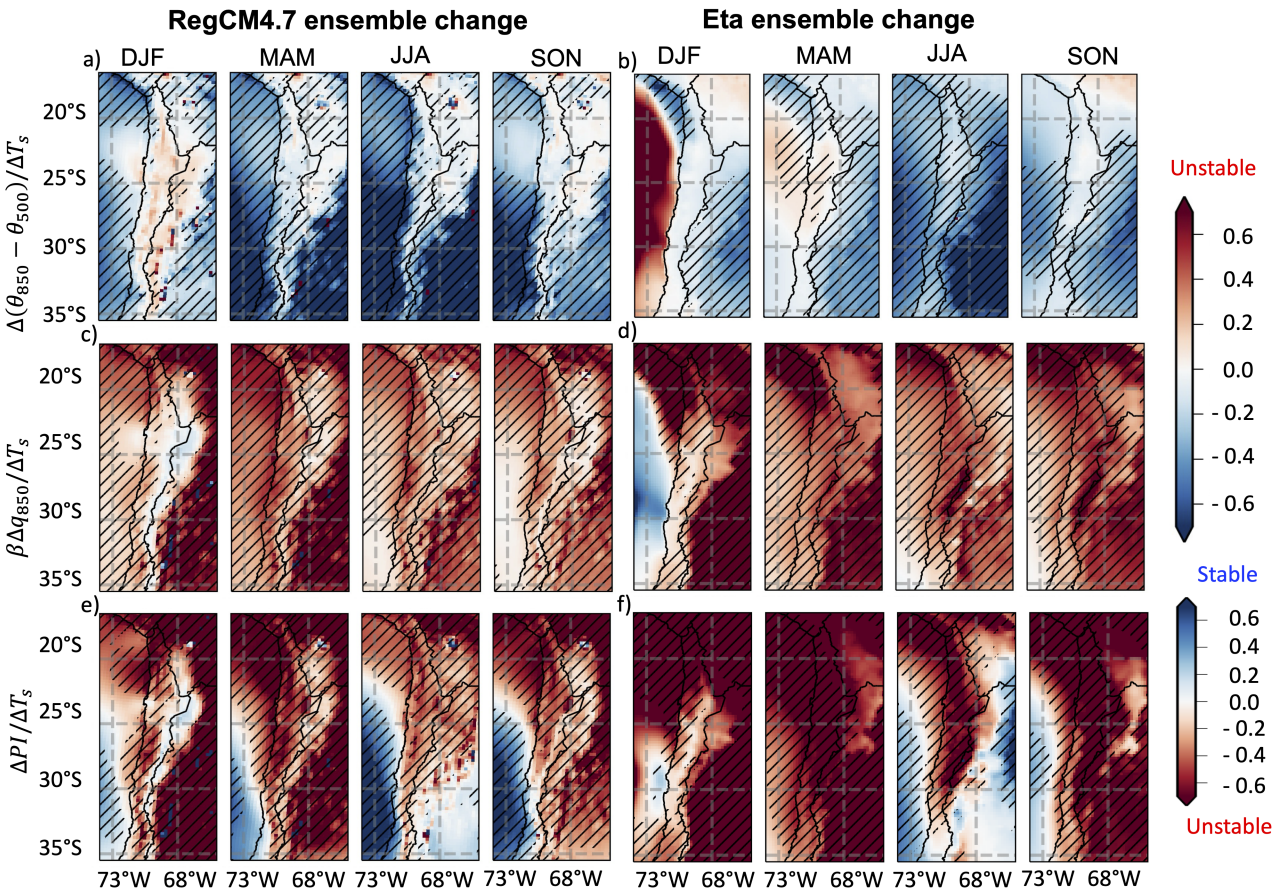

Figure 3.4: Seasonal change of a) θ_{850}, b) θ_{500}, c) q_{850} y d) PI projected by the RegCM4.7 simulations. Dashed lines denote that the three models agree in the sign of the change.

pattern is preserved by Eta simulations CanESM and HadGEM2 in the Central North and Central South regions. Despite the more unstable projections in all the models, the dynamic contribution to precipitation, e.g., the poleward expansion of the subsidence zone of the Hadley cell, may explain the deviation from the thermodynamic projection, especially during winter, when precipitation mostly depends on the orographic enhancement of fronts and atmosphere rivers crossing through the Andes and enhanced synoptic activity (Aceituno et al., 2021). The last explains the apparent loss of correlation between the changes in precipitation and instability during wintertime (Fig. 3.5, JJA) in all regions. When analyzing the HadGEM2 simulations in Eta and RegCM4.7 (squares), it is evident that even with the same forcing GCM, the RCM schemes and/or the horizontal resolution play an important role in the spread of the projections. For example, while the RegCM4.7-HadGEM2 simulation projects less precipitation during summer in a more unstable troposphere, the Eta-HadGEM2 simulation shows enhanced instability and positive precipitation projections for the same season (Fig. 3.4c). This aspect should be further explored.

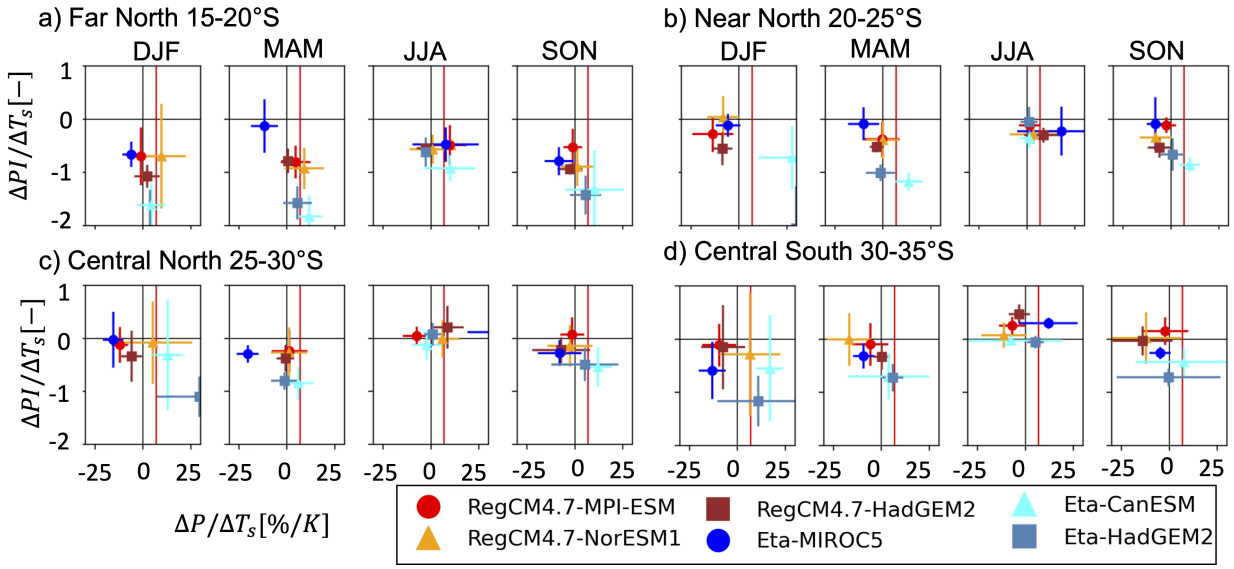

Figure 3.5: Normalized Potential Instability change v/s Normalized Precipitation changes at seasonal scale for different latitudinal bands (rows) simulated by RegCM4.7 (blue tones) and Eta (red tones) simulations. The vertical red line is the Clausius-Clapeyron expected change of ∼7%/K

3.5 Discussion and concluding remarks

Compared to other Mountain regions where summer precipitation is expected to increase in RCMs (e.g., Giorgi et al., 2016; Grose et al., 2019; Zobel et al., 2018), the precipitation enhancement is only simulated in the subtropical Andes by Eta and RegCM4.5 models (Fig. **??**b,d) and it is not observed in the driving GCMs ensemble. However, the RegCM4.7 and REMO2015 do not show that behavior, suggesting that i) The grid resolution is not enough to capture well those expected changes, ii) The driving GCM, and iii) RCMs parametrizations strongly influence the expected change, among others. Nevertheless, the extreme events are expected to increase during summer for the coarser RCMs (Fig. 3.2a,c) and during fall for the GCM ensemble (Fig. 3.2f). In all cases, the instability is expected to increase, especially in the northern part of the domain where the Andes reach the highest altitudes (∼4000 m a.s.l.). Convective precipitation mechanisms are less prominent than synoptic features in modulating the precipitation, specifically during wintertime, when most of the precipitation falls, and the negative signals in the mean precipitation can be associated with the expansion of the Hadley Cell and the poleward shifting of the storm tracks (e.g., Pfahl et al., 2018).

Even when yearly extreme precipitation events show robust positive changes of precipitation in the SWS between regional models (Lagos-Zúñiga et al., 2022a; Reboita et al., 2022), our study showed different results at seasonal scales, simulating an increase of extreme daily precipitation in the coastal region of the Far North in summer (Fig. 3.2e and Fig. 3.3a), the coast of the Central South region between spring and fall (Fig. 3.2e); and in the western slope of the Andes between Fall and Spring in the 30-35°S region (Fig. 3.2d). Even with the same driving GCMs, the RegCM4.7 and REMO2015 produce significantly

different projections of seasonal and extreme precipitation, confirming the impact of model features previously discussed in simulating precipitation and surface processes (e.g., Nguyen et al., 2022); however, within the same RCM, the robustness of precipitation change is more evident at seasonal scale (Fig. **??**) than extreme daily precipitation (Fig. 3.2). Despite these discrepancies, there is an agreement between RCMs and GCMs between fall and spring in the Central Sout regions (30-35°S) regarding a decrease of seasonal precipitation (∼-20%) and an increase of Rx1day (∼10-25%) in the period between fall and spring in the Central Southern region. This region is more dominated by synoptical activity, suggesting that higher resolution of future simulations may provide a better understanding of the expected precipitation change, as indicated by Hodnebrog et al. (2022) around the sub-tropical Andes. However, in northern latitudes, there is a strong disagreement among the RCMs and GCMs for almost all seasons; in these latitudes, convective precipitation related to the SA monsoon during summer and cut-off lows provide the forcing to precipitation that may not be well captured by the RCMs, as shown in Torrez-Rodriguez et al. (2023) using the same models of this study.

Our main findings are summarized as follows:

- RCMs differ in seasonal and extreme precipitation signs compared to their driving GCMs. However, some features appear robust, for instance, the drying signal in extratropical western Andes (∼-20%) between the fall and spring seasons.
- Changes of Rx1day precipitation in the studied zone may differ from the seasonal precipitation; the sign of change occurs at ∼28°S and between the Pacific coast. When the seasonal precipitation is expected to increase, the mean of extreme precipitation will diminish—suggesting a change in the frequency distribution of precipitation.
- Projections in the potential instability index suggest a significant trend to more unstable conditions in the continent; however, the expected increase in the seasonal precipitation is only observed in the subtropics (15-20°S), while some intensification in Rx1dayt is observed during the warm seasons north of 25°S and in the Southern Central region between 30-35°S between fall and spring seasons at the western slope of the Andes.

Further research is still needed to explain why the robustness of the drying signal in GCMs diminishes when we shift our focus to RCMs that exhibit varying signals. However, upon examining the underlying mechanisms, it is observed that the sign of instability tends to determine the direction of changes, except for wintertime occurrences. Additionally, a significant difference between the coarser regional model resolution RegCM4.7 (0.22°) and finer RegCM4.5 (0.11°) suggests that precipitation change in the studied region is much more uncertain than what GCMs depict. To ascertain which projections are more reliable, we highlight the role of surface moisture behavior, which has the potential to offset the overall increase in stability caused by the warming amplification at higher altitudes. Our findings suggest a need for enhanced observations of soil and atmospheric moisture

in mountainous regions, which could significantly improve the testing and verification of models and projections.

Data Availability

The RCMs and GCMs used in this study are available on the ESGF portal https://esg-dn1.nsc.liu.se/projects/esgf-liu/. The RegCM4.7 simulations are available on the website https://simulaciones.cr2.cl/ (In Spanish).

Acknowledgments

The authors acknowledge Andre Lyra from INPE, Brazil, for providing the fields for the Eta simulations and model schemes and Dr. Joni-Pekka Pietikäinen from GERICS for providing the REMO2015 schemes used in the SAM22 simulations.

Supplmentary Information

We provided figures of seasonal projections of precipitation by each individual GCM, and seasonal changes of the different components of the PI scaling procedure in Appendix B.

Chapter 4

Convection-Permitting simulations in summer precipitation events in sub-tropical Andes (30-35°S)

This chapter was partially presented in two international conferences (Lagos-Zúñiga et al., 2022b,d). An article about this chapter is under preparation with the contributions of Deniz Bozkurt and Roberto Rondanelli.

Abstract

Evaluation of weather and climate simulations over the sub-tropical Andes is a significant challenge due to observation scarcity. The problem is exacerbated during summer, when precipitation involves convection-scale processes concentrated within a few kilometers, leading to intense mountain precipitation, landslides, and floods. The Chilean meteorological authority performs sub-daily weather numerical forecasts, and their schemes have not been evaluated specifically for these events. This study aims to evaluate different schemes of convection-permitting simulation behavior in two summer precipitation events associated with a Cut-Off Low (COL) and an Atmospheric River (AR). We consider five schemes for the planetary boundary layer, surface layer, cloud microphysics, and land surface with the Advanced Weather Research and Forecasting model (WRF). We evaluate the simulations through surface stations with precipitation records, temperature, winds, boundary layer height estimated through a ceilometer, and upper air soundings in Santo Domingo and Mendoza. Additionally, we simulate warmer sea surface temperature (SST) conditions in the AR event, forced by the climate change signal on five selected CMIP6 GCMs in the 2070-2100 period under the SSP5-8.5 scenario. Our results suggest that all tested schemes are highly sensitive in reproducing observations, presenting differences in cloud formation and magnitude and spatial scale of precipitation. The PGW experiment reveals that warmer conditions will likely enhance moisture advection and increase precipitation at northern latitudes while potentially altering near-surface winds on both sides of the Andes. However, given the high sensitivity observed in the WRF simulations for precipitation generation—comparable to that seen in the PGW experiment—further investigation through extended simulations or additional case studies is necessary to formulate more robust recommendations.

Key words: *Advanced Weather Research and Forecasting Model; Convective precipitation, extratropical Andes*

4.1 Introduction

Summer precipitation events in Central Chile do not receive as much attention as wintertime because they contribute to less than 10% of annual precipitation (Aceituno et al., 2021). However, because of stronger surface heating, the troposphere can present higher instability compared to wintertime. Because of the high temperatures, the freezing level is located upslope in the Andes, and therefore the precipitation triggers numerous hazards such as floods and landslides (e.g., Wilcox et al.,2016).

Viale and Garreaud (2014) have identified two mechanisms of summer precipitation: i) through strong winds, similar to winter events with stratiform precipitation, and ii) Through weak winds, characterized by local instability induced by cold air in the upper troposphere (e.g., Cut-Off Lows, hereafter COLs), or surface heating. These types of events have induced several human casualties and damage to infrastructure on mountain roads and bridges. Although events such as Atmospheric Rivers (AR) have proven to have higher moisture sources with large implications in runoff generation (Valenzuela et al., 2022), COL events have also produced interruption of water supply, road closure, and victims (El Mostrador, 2017; Meteored, 2023). Storms in the Andes are also challenging to capture with conventional precipitation gauges as they are sparsely distributed and are not equipped with windshields and the technology to capture snow. The use of additional estimations as satellite (e.g., IMERG Huffman et al., 2015) and reanalysis products to estimate precipitation from these events is also full of uncertainty (e.g., Lundquist et al., 2019).

Numerical weather models have been widely used to better understand the physical processes of weather systems. In complex terrain such as the Andes, the required resolution to reproduce realistic fields and precipitation and land features is finer than reanalysis ($\sim$ 0.25 °), and particularly convective precipitation occurs at scales smaller than $\sim$ $4km$, and therefore are not explicitly resolved by coarse simulations. In this context, the convection-permitting climate modeling (CPCM) simulations arise as a valuable tool to explicitly determine the convection at the required scale (Prein et al., 2015). In the last years, diverse institutions have produced these simulations that require high-performance computing and generate outputs with large storage requirements, particularly in South America; the National Center for Atmospheric Research has led the first simulations for the continent at approximately 4 km of horizontal resolution (Dominguez et al., 2023) for the 2000-2021 period. This effort strongly contributes to the region's understanding of mesoscale Convective Systems (MCS) and the Andes at a decadal scale. Although the convective precipitation is explicitly resolved, parametrized processes, such as the cloud microphysics and the planetary boundary layer, have been shown to impact precipitation modeling (Huang et al., 2023) significantly.

This chapter evaluates CPCM simulations from different model configurations, using the WRF (Skamarock et al., 2019) at kilometer-scale at two summer precipitation events associated with a COL and an AR. Here, we evaluate the surface precipitation, temperature, winds, and humidity generated by changing surface-process parameterizations of i) planetary boundary layer (PBL), ii) surface layer, iii) land surface model (LSM), and iv) cloud microphysics (MP). Additionally, we evaluate the Boundary Layer Height and the

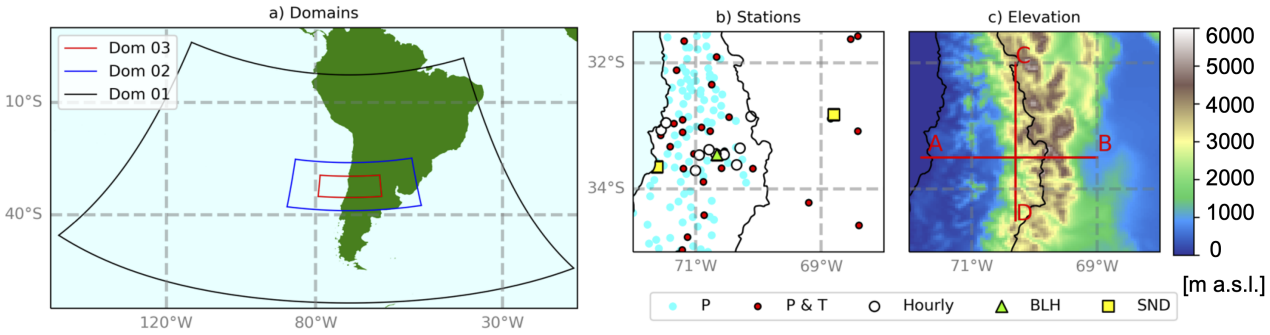

Figure 4.1: a) Domains configuration: Dom 01 ∼36 km, Dom 02 ∼ 12 km, Dom 03 ∼ 4km b) Stations used to evaluate the simulations, and c) Elevation and cross-section (in red) used to evaluate total precipitation in the selected events. P: precipitation, T: temperature, BLH: boundary layer height, and SND: sounding stations. Elevation in c) is taken from the WRF simulations Dom 03.

thermodynamics measured at two upper-air soundings.

4.2 Domain, data, and case study events

4.2.1 Study domain

The study focuses on central Chile (32-34.5°S), where most of the Chilean population lives in Santiago, Valparaíso, Rancagua, and Talca. On the eastern side of the Andes, the Argentinian region of Cuyo also hosts the cities of Mendoza, San Juan, and San Luis. The elevation of the areas studied spans from the sea level to the west of the pre-cordilleras in the Cuyo region, reaching peak elevations higher than 6000 [m a.s.l.] such as the Aconcagua Mountain (Fig. 4.1c).

4.2.2 Observations

The precipitation amounts during the events were compared at different scales: i) Total precipitation at surface stations, ii) Hourly stations (Figure 4.1b, and iii)Through the IMERG product (Huffman et al., 2015). The hourly stations used are shown in Table 4.1, ranging from the Pacific coast at 77 [m a.s.l] in *Santo Domingo* to the station *Las Melosas* in the western slope of the Andes at 3320 [m a.s.l.]. The hourly records evaluated precipitation, temperature, relative humidity, and wind. Additionally, we used the Boundary Layer height (BLH) estimated through the ceilometer in the Department of Geophysics, U. de Chile (DGF) (Muñoz and Undurraga, 2010). Finally, we evaluated the tropospheric thermodynamics observed in the Santo Domingo and Mendoza stations and the temperature and wind speed AMDAR (Moninger et al., 2003) profiles during the evolution of the events. The AMDAR profiles are taken from the Pudahuel Airport departures and arrivals from commercial flights collected by the Chilean meteorological Agency (*Dirección Meteorológica*

Table 4.1: Hourly meteorological stations considered for the evaluation process. PBL: Boundary layer height, P: Precipitation, T: Surface air temperature, HR: Surface relative humidity, and U: Wind speed and wind direction at 10 m. The Pudahuel station also has AMDAR profiles of T and U.

Name	**Lat**	**Lon**	**Elev**	**Variables**
DGF	-33.457	-70.662	555	PBL
El Colorado	-33.35	-70.2936	2750	P, T, HR, U
Los Libertadores	-32.845	-70.119	2955	P, T, HR, U
Quinta Normal	-33.445	-70.683	520	P, T, HR, U
Pudahuel (AMDAR)	-33.378	-70.788	474	P, T, HR, U
Cerro Lo Prado	-33.458	-70.949	1068	P, T, HR, U
Santo Domingo	-33.656	-71.613	77	P, T, HR, U
El Paico	-33.706	-71.008	275	P, T, HR, U
San José Guayacán	-33.615	-70.35	928	P, T, HR, U
Las Melosas	-33.864	-70.273	3320	T, HR, U
Laguna Negra	-33.666	-70.108	2780	T, HR, U
Termas del Flaco	-34.892	-70.330	2650	T, HR, U
Glaciar Cipreses	-34.533	-70.415	1880	T, HR, U
Portillo	-32.833	-70.117	3000	T, HR
El Yeso Embalse	-33.676	-70.089	2475	P, T, HR
Pangal en Pangal	-34.251	-70.334	1500	P

de Chile) within a radio of 16 km, averaging all flights at hourly time-step. This data was previously used in Santiago to characterize the Boundary layer heat budget in Muñoz et al. (2022).

4.2.3 Case study events

February 2017 cut-off low event(Feb-2017)

The February 2017 event, hereafter Feb2017, was synoptically forced by a Cut-Off Low event, started during the night of February 25 and finished on February 27th, and presented a typical convective behavior (Garreaud, 2017) with concentrated precipitation in the mountains with maximum total precipitation of 22.8 [mm] in the *El Yeso Embalse* station during 8 hours. This event interrupted the fresh water supply due to the extreme turbidity on the rivers and caused many casualties and damaged infrastructure (24horas, 2017).

January 2021 atmospheric river event (Jan-2021)

The January 2021 event, which occurred between January 28th and February 1st (Jan2021), was synoptically forced by a zonal AR (Valenzuela et al., 2022) reaching a total amount of precipitation of 62.7 [mm] in the *El Yeso embalse* Station during 65 hours ($\sim 1.5 days$), and about 120 [mm] in the IMERG final product. The AR landed at 39 °S and

then moved northward, evolving with a formation of a COL in the poleward direction. This event also caused significant landslides and flashfloods in the studied region (El Mostrador, 2021).

4.3 Methodology

The experimental setup was based on testing physical schemes in the WRF model skamarock2019description on the representation of the previously described summer precipitation events Feb2017 and Jan2021. We tested different schemes in Table 4.2: 1) surface process: planetary boundary layer, surface layer, surface physics; and the microphysics considered in precipitation processes. Secondly, we evaluated the different simulations of surface temperature, relative humidity, winds, and precipitation in surface stations (Fig 4.1b). The simulated total precipitation was also compared with IMERG final run (Huffman et al., 2015). Finally, we compared temperature, humidity, and winds from upper-air observations and the boundary layer height (Ceilemeter-based). The comparisons were made at the nearest WRF model's grid point corresponding to each station location.

4.3.1 Model configuration

The model configuration was set in three one-way nested domains, 61 vertical levels, and horizontal resolutions of 36, 12, and 4 km in domains d01, d02, and d03, respectively (Fig. 4.1a), defining a grid-cell number 270x200 (d01), 261x121 (d02) and 388x160 (d03) in the west to east and south to north, respectively. The initial and border conditions come from the GFS reanalysis (Compo et al., 2011) for the variables air temperature, geopotential height, sea surface temperature, skin temperature, specific humidity, and pressure every 6 hours in all the domains. The simulations considered two warm-up days, reaching five days and 18 hours for the Feb-2017 event, starting on February 22nd, 2017. The Jan-2021 event began on January 21st with a total of seven days and 18 hours of simulation. We defined a base case (WRF-A), following the recommendations of Yáñez-Morroni et al. (2018) in Central Chile. In that research, they collaborated with the *Dirección Meteorológica de Chile* and tested the schemes used by this Agency to perform forecasts in Chile numerically. The WRF-A schemes consider the Dudhia short-wave scheme (Dudhia, 1989) and the RRTM long-wave radiation scheme (Mlawer et al., 1997). The domains d01 and d02 used the Grell 3D Ensemble to parametrize convective-clouds (Grell, 1993) after testing its performance in simulating convective precipitation over Santiago (Saide et al., 2011). The inner domain resolves explicitly convection and was not parametrized for cumulus. All the tested schemes consider the previous physics mechanisms, and the differences among them considered the findings of Yáñez-Morroni et al. (2018) and Arévalo et al. (2023) to test different Microphysics, Land-Surface models, and the Planetary Boundary Layer (PBL) and surface layer, following the experiments of Huang et al. (2023). Table 4.2 shows the final experiment setup.

The microphysics scheme WSM6 corresponds to the WRF Single Moment class 6 proposed by Hong et al. (2004); it includes six components of water: mixing ratio,

Table 4.2: WRF schemes configuration for the Convection-Permitting simulations.

Process	Mycrophisics	Surface Layer	Land Surface Model	Planetary Boundary Layer
A - Base	WSM6	MYNN	Noah-MP	MYNN 2.5
B- Lin MP	Lin	MYNN	Noah-MP	MYNN 2.5
C- MM5-YSU SF-PBL	WSM6	Revised MM5 Monin-Obukhov	Noah-MP	YSU
D- Noah LSM	WSM6	MYNN	Unified Noah LSM	MYNN 2.5
E - Thompson MP	Aerosol-aware Thompson	MYNN	Noah-MP	MYNN 2.5
F - Janjic SF-PBL	WSM6	Monin-Obukhov (Janjic)	Noah-MP	MYJ

cloud water, cloud ice, rain, snow, and graupel. This scheme was used in the Andes in Yáñez-Morroni et al. (2018); Comin et al. (2018); Schumacher et al. (2020a). The Lin Scheme (Lin et al., 1983) also represents the six components of water but differs from WSM6 in ice and snow generation from water processes (see Hong et al., 2009 for a detailed comparison). The Thompson aerosol-aware scheme represents five components of clouds and was tested in the continental simulation of North America by CPCM in Liu et al. (2017). The PBL YSU - Yonsei University Scheme (Hong et al., 2006) and the Unified Noah Land Surface Model (LSM) scheme were tested in the Peruvian Andes to forecast extreme precipitation, as documented in Moya-Álvarez et al. (2018). The Noah-MP LSM (Niu et al., 2011) was recommended in Yáñez-Morroni et al. (2018) for enhancing the representation of surface processes, timing of snow water equivalent and runoff peaks. The Mellor-Yamada-Nakanishi-Niino (MYNN) scheme, which includes a total kinetic energy (TKE) closure at level 2.5 (Nakanishi and Niino, 2006), was tested due to its accurate representation of Planetary Boundary Layer (PBL) height over Santiago (Saide et al., 2011).

4.3.2 Evaluated fields

We evaluate 2D simulated fields compared to surface observations: 10 m wind speed (U10 and V10), surface temperature (T2M), relative humidity derived from surface water vapor mixing ratio (Q2), surface pressure (PSFC), surface wind direction derived from U10 and V10, and Boundary Layer Height (BLH). For Santo Domingo and Mendoza, we evaluated the 3D fields of air temperature (T), wind speed (U and V), and specific humidity (QVAPOR). Due to the potential spread of height within a WRF cell at 4 km, we corrected the simulated temperatures considering:

$$T_X^c = T_X^r + \gamma(H_Y - H_X) \tag{4.1}$$

where T_X^r is the raw estimation of temperature at the nearest grid cell of WRF to the

station X, γ is the lapse rate, estimated to be -5.9 $km/°C$ during wet days in the Central Andes, according to Ibañez et al. (2021) and Lagos-Zúñiga et al. (2021c). T_X^c is the corrected temperature and H_Y is the elevation of the model (Y) and H_X the elevation of the station.

For comparison purposes, we evaluated the cloud cover fraction (CLDFRA), computed by averaging over the time between 12 and 18 hours Local Time and between 900 to 400 hPa to reproduce mean conditions of cloud fraction during the most vigorous convection activity and near the surface.

4.3.3 Evaluation metrics

We evaluated the temporal coherence between simulations and observations through the Pearson correlation coefficient (r),

$$\rho = \frac{\text{cov}(X, Y)}{\sigma_x \sigma_y}, \tag{4.2}$$

where $cov(X, Y)$ stands for the covariance between the observations (X) and the nearest grid-cell simulation of WRF (Y).σ_x and σ_y are the standard deviations from X and Y, respectively. To characterize the differences between simulations and observations, we used the Root Mean Square Error ($RMSE$, Eq. 4.3) and the mean error (ME, Eq. 4.4) to detect systematic biases in the simulations. X_i and Y_i denotes observations and simulations in time-step i out of N, respectively.

$$RMSE = \sqrt{\frac{\sum_{i=0}^{N-1}(X_i - Y_i)^2}{N}} \tag{4.3}$$

$$ME = \frac{\sum_{i=0}^{N-1}(X_i - Y_i)}{N} \tag{4.4}$$

4.3.4 Warmer SST experiment

To assess the potential impact of climate change on the historical summer precipitation events, we used a sensitive analysis under warming SST conditions; this procedure has been widely used in literature to test precipitation sensitivity to different SST conditions (e.g., Katsafados et al., 2011; Pilatin et al., 2021; Bozkurt et al., 2016). In this aspect, selecting a single model, scenario, and future period presents various subjectivities in similar approaches such as Pseudo Global Warming (PGW) experiments (e.g., Dominguez et al., 2023), the literature selects an average of several average GCM projections to produce new boundary conditions, warmer than the historical series.

To select GCMs, we used the findings of Gateño et al. (2023), whose evaluated past performance of GCMs, including seasonality, spatial patterns, and probability density functions represented by a subset of 26 GCMs in Chile, including teleconnections of the ENSO and SAM affecting temperature and precipitation in different Chilean macrozones. In our experiments, we perturbed the historical SST values with the average of the projected

SST from the best five GCMs ranked in Chile in the historical period, selecting the period 2071-2100 in the SSP5-8.5 scenario. This perturbation was applied to the intermediate files of WRF using the equation:

$$SST_{fut} = SST_{hist} + \overline{\Delta SST}_{GCM} \tag{4.5}$$

where SST_{fut} are the future conditions of SST, SST_{hist}, the historical conditions, and $\overline{\Delta SST}_{GCM}$, the mean of the projected change of SST given by the best-performing GCMs based on past-performance evaluation Gateño et al. (2023), shown in Fig. 4.2, presents warmer conditions of $\sim$ 3 °C, with enhanced warming in the Pacific coast, and moderate warming of $\sim$ 1 °C reaching near 30 °S enclosed by warmer conditions equatorward and poleward, this pattern does not represent the regional cooling observed during the last decades (e.g., Zhang et al., 2010; Falvey and Garreaud, 2009b; Lagos-Zúñiga et al., 2024), a phenomenon under discussion as there is a strong agreement among GCMs to a warming signal (Gutiérrez et al., 2021) and it is out of the scope of this research. This chapter presents the results of warming SST just for the WRF-A scheme and the AR event in January 2021, future simulations in the February 2017 event, and considering other best-performing schemes is part of an ongoing initiative and is not presented in this chapter.

The SST projections in Fig. 4.2

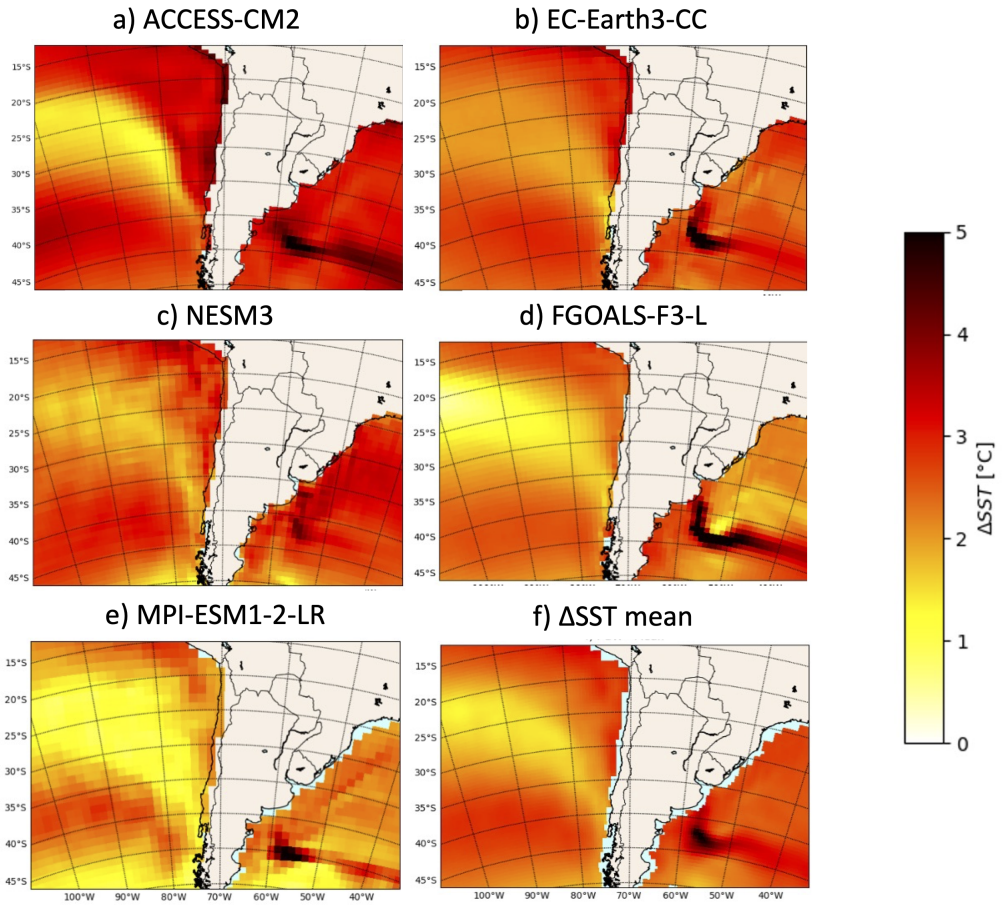

Figure 4.2: SST projection by selected CMIP6 GCMs in the (2070-2100) period at the SSP5-8.5 scenario.

4.4 Results

4.4.1 Evaluation of the simulations

Total precipitation

The simulated precipitation during the Feb2017 event in the WRF-A (Base) model differs significantly from the spatial patterns observed over the three days of the events. However, precipitation is simulated in high-elevation sites. Additionally, it can be observed that there are significant differences between the five schemes; mainly, the WRF- F scheme presents a wet signal in Argentina compared to the base simulations. The differences between the models are not homogeneous across space and time (Fig. 4.3)

The AR Jan2021 event seems to be better represented in the base simulation than the COL Feb2017 event, but the precipitation does not achieve northern latitudes as depicted in the observations. Particularly on January 29. the precipitation almost reached 32.5°S, but

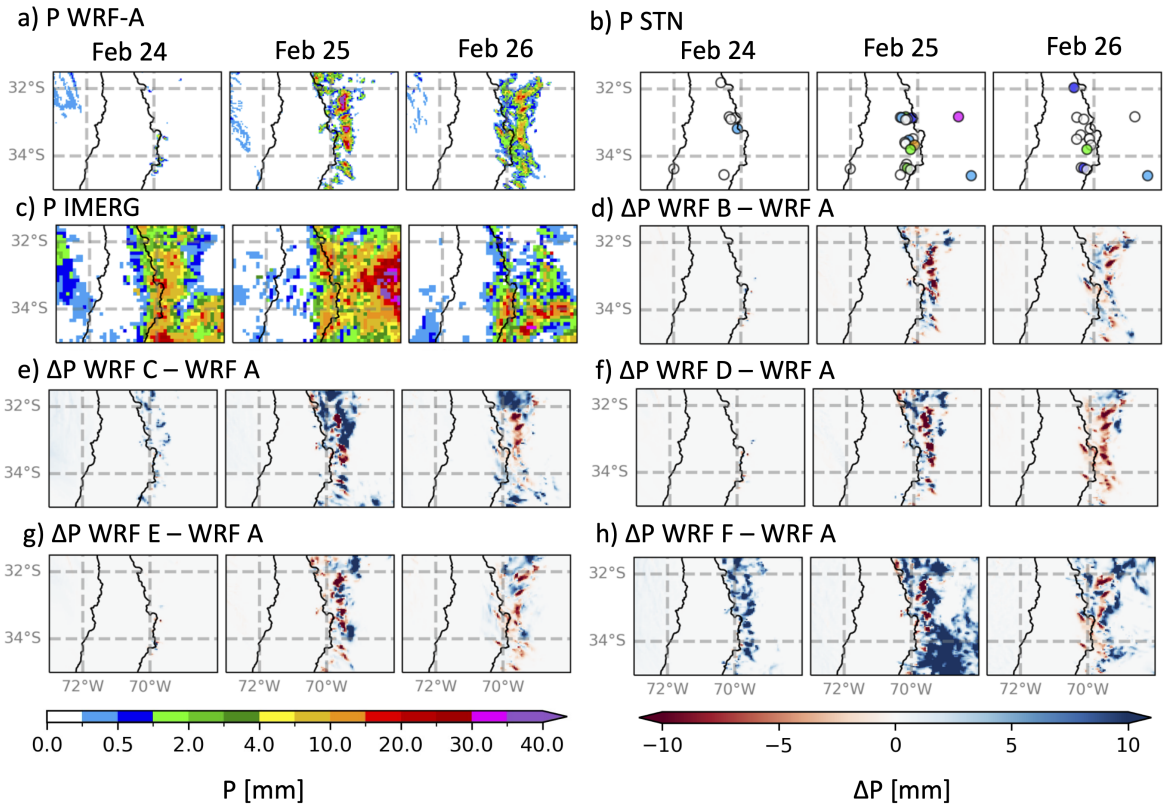

Figure 4.3: a) Daily precipitation as simulated by the WRF-A scheme, and b) Graphs depicting observed precipitation at surface stations (STN), and c) estimates provided by IMERG. d-h) Plots illustrating the differences in daily precipitation between schemes B through F and the WRF-A simulations. Event from February 2017.

the WRF A scheme underestimated total precipitation, reaching only 34°S (Fig. 4.4a-b). The difference in simulated precipitation is more significant in the C and D simulations, where the frontal precipitation achieves northern latitudes. However, none of the simulations capture the observed rainfall on the first day of the event (Fig. 4.4c-g).

When analyzing the orographic profile of precipitation (A-B: West to East), it can be appreciated that none of the simulations captures all the observed precipitation in both events; however, in the AR Jan2021 event, the WRF-C scheme is the closest to the observations (Fig. 4.5a-b). Regarding the meridional gradient of precipitation (C-D: North to South), it is confirmed that the models can't reproduce the occurrence of precipitation at northern and southern latitudes in the case of the Feb2017 event. For Jan 2021, the simulated precipitation in WRF-C and WRF-D are closest to the observations but tend to overestimate the observed precipitation around 32.5 °S.

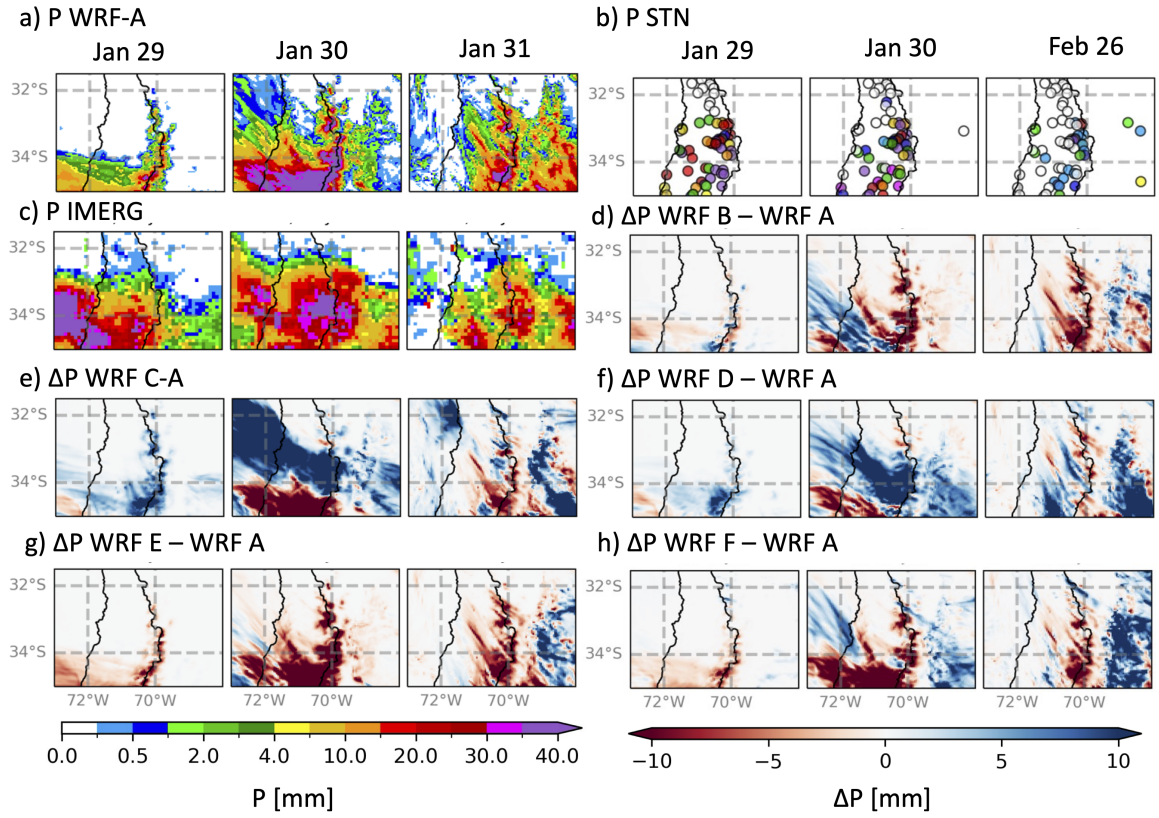

Figure 4.4: Same as Figure 4.3 but from January 2021 event.

Wind simulations

The wind simulation in WRF-A for the Feb2017 event presents weak surface winds on the western slope of the Andes, with winds shifting from N to NE along the Pacific Coast to E winds inland. The eastern slope of the Andes presents N to NW, reaching maximum wind speed aloft the Andes. The wind direction does not change significantly among the simulations, with the most significant differences in speed at the WRF-F simulations with higher winds in the western Andes and weaker winds in Argentina compared to WRF-A (Fig. 4.6). In the case of Jan2021, this event presented a more heterogeneous behavior among the tested schemes. These events simulated strong surface winds $> 8m/s$ in the Pacific and on top of the Andes and moderate to weak winds in Chile and Argentina. Notably, the WRF-C scheme presents stronger surface winds in the continent on January 30 and January 31. Additionally, in the WRF-D, WRF-E, and WRF-F, weaker winds were observed along the Pacific coast (Fig. 4.7).

Cloud cover simulations

The cloud cover simulations do not reveal a cloud cover intensification at the top of the Andes in the Feb2017 event (WRF-A). Still, for February 26, however, the cloud fraction

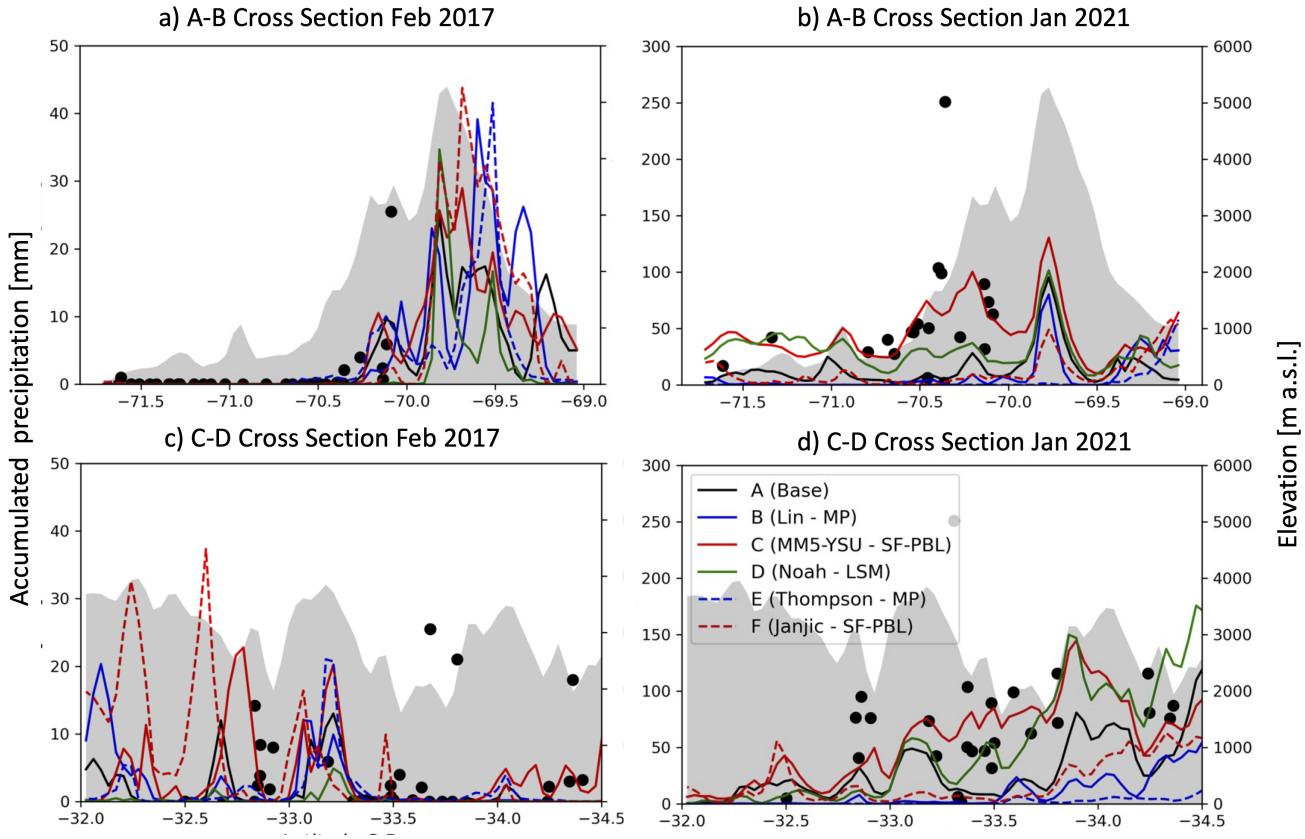

Figure 4.5: Longitudinal cross sections (A-B, up) and Latitudinal sections (C-D, down) for the Feb2017 (left) and Jan2021 (right) events. The shadowed areas are the terrain elevation depicted in the secondary vertical axis.

is enhanced in the WRF-C, WRF-E, and WRF-F simulations, reflecting the impacts of the PBL scheme in this aspect (Fig. 4.8). In the case of the Jan 2021 event, the enhanced cloud cover is evident due to the presence of the AR. In that case, WRF-C and WRF-D experiments presented more clouds at northern latitudes compared to the base simulation ($> 10\%$); in the case of models WRF-B and WRF-E, a suppression in cloud fraction is observed on January 30 h, and on January 31. The differences in cloud formation in northern latitudes may explain the precipitation in these regions simulated by WRF-C and WRF-D schemes (Fig. 4.9).

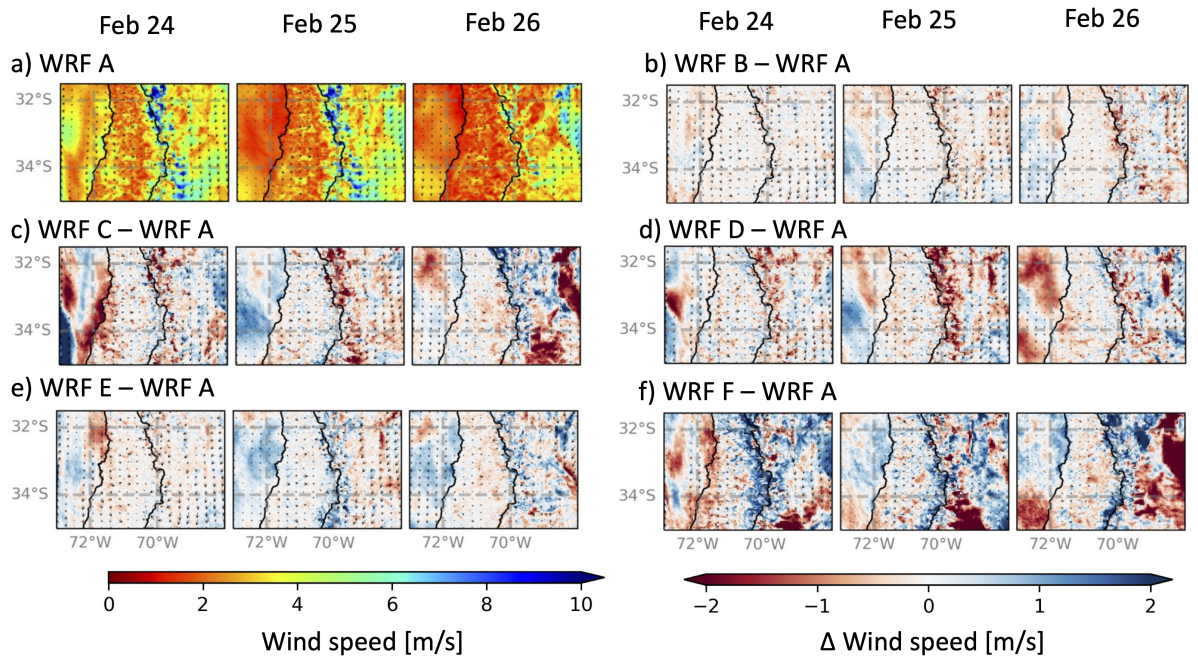

Figure 4.6: Wind speed simulated in the Feb2017 for the WRF-A scheme, and the differences between simulations. Arrows denote wind direction.

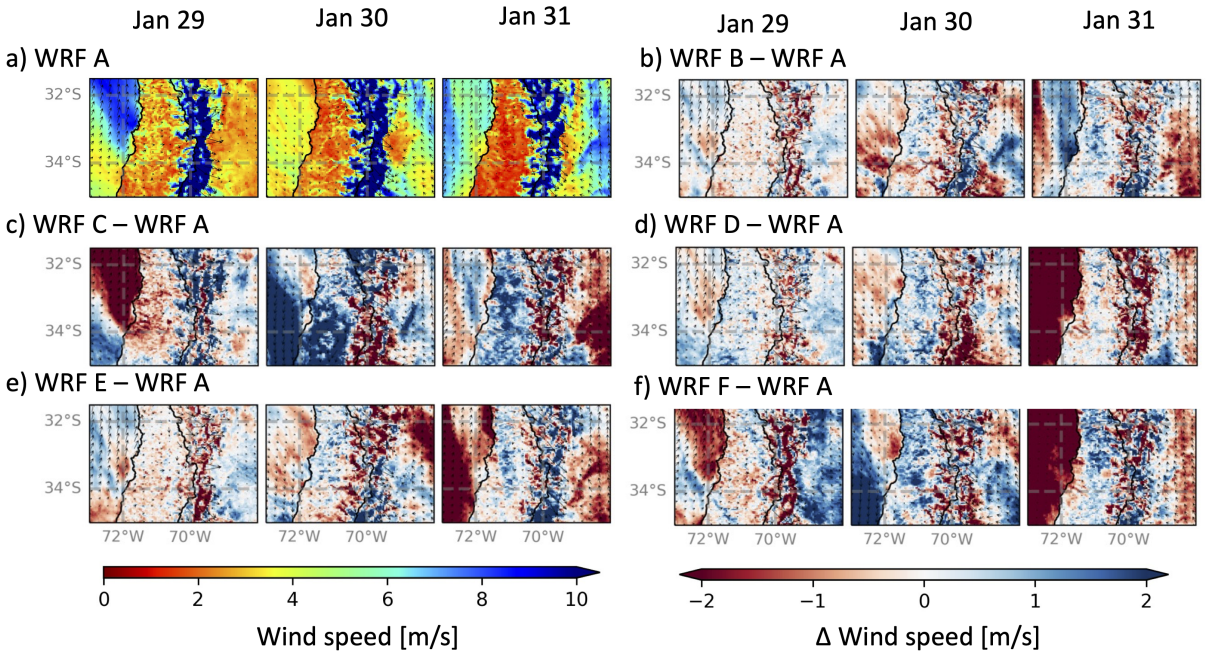

Figure 4.7: Same as Fig. 4.6 but for the Jan 2021 event

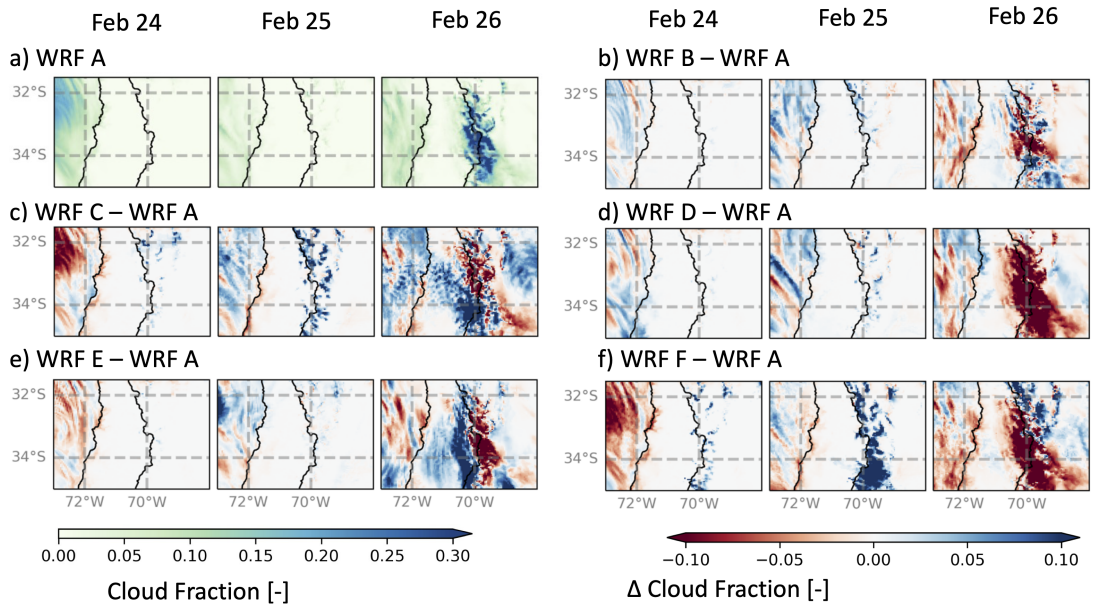

Figure 4.8: a) Cloud cover simulated by the WRF-A scheme. b-f) Relative differences simulated by the WRF-B to WRF-F configuration.

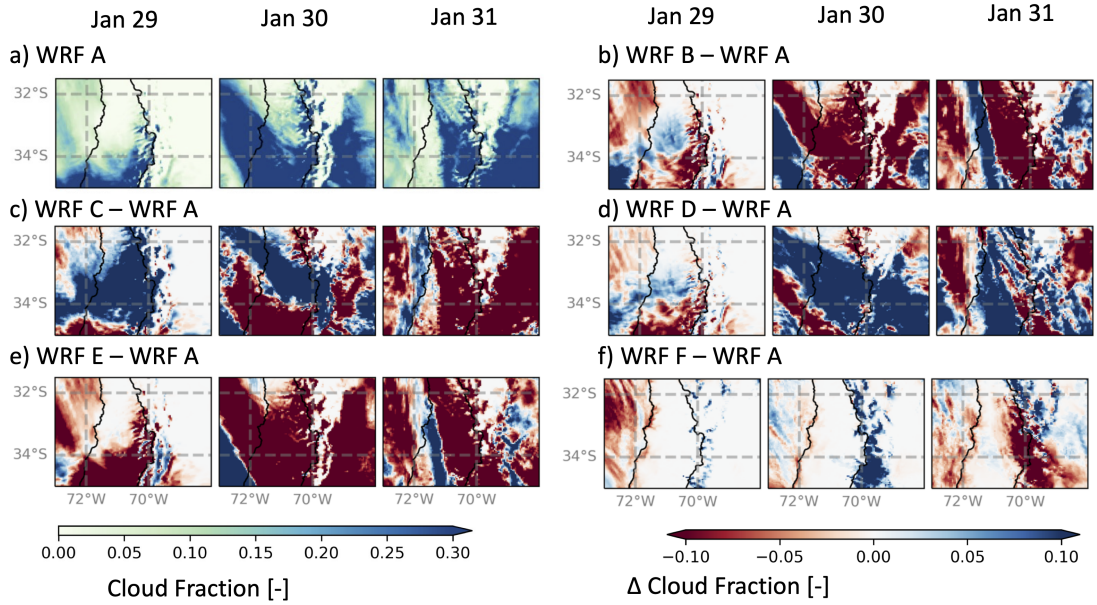

Figure 4.9: Same as Fig. 4.8 but for the Jan2021 event.

Hourly time series

To better illustrate the behavior of the simulations over time, we show the time series of observations and simulations in selected stations at high-elevation sites: *El Yeso Embalse* and

Laguna Negra. The PBL representation is assessed using observations at the DGF station. During the February 2017 event, none of the simulations could accurately reproduce the timing and magnitude of the observed precipitation, translating into low correlation metrics (Table 4.3, r $\sim$ 0). Hourly surface temperatures were better represented by the WRF-B and WRF-E simulations, with biases $<$ 1 $^\circ$ C and RMSE $<$ 3 $^\circ$ C (Table 4.4); however, the simulated surface air temperature is generally warmer than observations by up to 1.2 $^\circ C$ in *Laguna Negra* (Fig. 4.10T2m). The surface relative humidity is underestimated between -8.5 and -11.7%, while the wind speed is better represented in timing and biases (r $>$ 0.4, RMSE$<$ 2.6 m/s). Wind direction is the most challenging variable to represent for all the simulations, with errors of around 90°. The details of evaluation metrics for wind speed and relative humidity are shown in Appendix C.

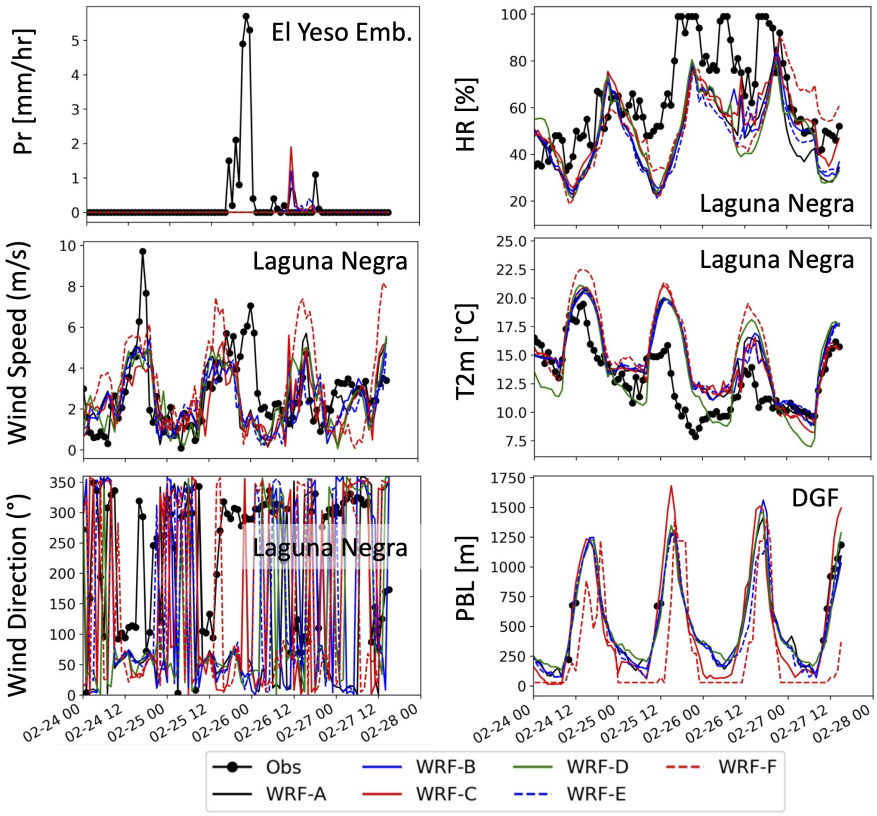

Figure 4.10: Observed and simulated time series in selected stations during the Feb 2017 event. Pr: Hourly precipitation, HR: Relative humidity, T2m: Surface air temperature, PBL: Planetary boundary layer height.

In the Jan 2021 event, the results are different as the models better reproduce the timing and magnitude of precipitation at *El Yeso Embalse*, with biases $<$ 0.5 mm/hr; the WRF-A simulation presented a higher Pearson Correlation Coefficient of 0.57; however

within all stations the WRF-C scheme excels in the time with moderate correlation r = 0.3 in median (Table 4.3Jan 2021. The relative humidity, similar to that in February 2017, is underestimated by all the simulations, which may reflect a lack of efficiency in condensation processes. Surface temperature is not well represented on January 30 and January 31. However, the RMSE for all the models is between 1.9 and 5.8 °C in the WRF-A at *Colorado* station and WRF-D schemes at *El Paico* station, respectively. The biases of wind speed range between 0.01 in the WRF-C and WRF-D at *Guayacán* station and 9.8 m/s in the WRF-E simulations at *Termas del Flaco*, respectively, and the wind direction ranges between 50 to 87° in WRF-D and WRF-A, respectively, proving to be the most challenging variable to reproduce (Fig. 4.11). A summary of all hourly stations and metrics can be seen in Appendix C.

Table 4.3: Statistic from hourly series of precipitation simulations across the different WRF configurations. The rows represent each simulation's 25th, 50th, and 75th percentiles.

WRF Configuration	Feb 2017			Jan 2021		
	Bias [mm/hr]	r	RMSE [mm/hr]	Bias [mm/hr]	r	RMSE [mm/hr]
A-Base	-0.02	-0.02	0.01	-0.37	-0.03	0.95
	0	-0.02	0.04	-0.31	-0.01	1.39
	0	-0.02	0.13	-0.18	0.02	1.55
B-Lin MP	-0.02	-0.02	0.01	-0.37	-0.01	1.04
	0	-0.01	0.02	-0.32	0.13	1.18
	0	-0.01	0.12	-0.27	0.25	1.53
C-MM5-YSU SF-PBL	-0.01	-0.02	0.01	-0.21	**0.26**	**1.04**
	0	-0.01	0.05	-0.1	**0.30**	**1.36**
	0	-0.01	0.2	-0.02	**0.40**	**1.44**
D-Noah LSM	-0.02		0.01	**-0.19**	0.04	1.06
	0	nan	0.01	**-0.08**	0.13	1.28
	0		0.12	**-0.02**	0.30	1.69
E-Thompson MP	-0.02	-0.01	0.01	-0.44	-0.02	1.04
	0	-0.01	0.04	-0.35	-0.01	1.18
	0	-0.01	0.16	-0.29	0	1.54
F-Janjic SF-PBL	-0.02	-0.01	0.01	-0.33	-0.02	1.04
	0	-0.01	0.01	-0.28	0.02	1.17
	0	-0.01	0.12	-0.2	0.04	1.69

Finally, the PBL representation for DGF was evaluated in the hours when the ceilometer identified enough aerosols in the atmosphere during the events in Santiago to estimate the mixing layer height. In general terms, the models reproduce the daily cycle of PBL with a high correlation coefficient, with the WRF-C and WRF-D as the best schemes. However, regarding the biases, the WRF-E excels the other models with biases of -27 m and 161 m for the Feb 2017 and Jan 2021 events, respectively (Table 4.5).

Table 4.4: Statistic from hourly series of temperature simulations across the different WRF configurations. The rows represent each simulation's 25th, 50th, and 75th percentiles.

WRF Configuration	Feb 2017			Jan 2021		
	Bias $[°C]$	r	RMSE $[°C]$	Bias $[°C]$	r	RMSE $[°C]$
A-Base	-0.92	0.61	2.33	-1.4	0.64	2.48
	-0.37	0.71	2.72	-0.75	0.69	3.75
	0.62	0.74	3.00	-0.38	0.78	4.27
B-Lin MP	-0.95	**0.62**	**2.27**	-1.13	0.63	2.75
	-0.33	**0.72**	**2.66**	-0.5	0.67	3.53
	0.61	**0.75**	**2.94**	-0.16	0.75	4.22
C-MM5-YSU SF-PBL	-0.78	0.59	2.37	-1.84	**0.61**	**2.75**
	-0.46	0.70	2.68	-1.3	**0.78**	**3.43**
	0.55	0.75	3.02	-0.89	**0.82**	**4.04**
D-Noah LSM	-1.42	0.58	2.73	-1.92	0.63	2.97
	-0.70	0.66	3.11	-1.34	0.66	3.72
	0.12	0.74	3.18	-0.84	0.78	4.17
E-Thompson MP	**-0.81**	0.63	2.31	**-0.98**	0.61	2.71
	-0.28	0.70	2.73	**-0.06**	0.64	3.63
	0.68	0.74	2.96	**0.47**	0.72	4.04
F-Janjic SF-PBL	-0.36	0.61	2.55	-1.31	0.59	2.79
	0.05	0.70	3.01	-0.09	0.72	3.17
	1.02	0.74	3.12	0.39	0.77	4.11

Sounding evaluation

The sounding observations reveal the different behavior from the Feb-2017 and Jan-2021 events. While both events presented near-surface temperatures near to 20 ° C, the winds were considerably weaker during the Feb-2017 event (< 18 m/s in Santo Domingo and < 10 m/s in Mendoza, while the mid-level jet in the Jan-2021 event presented winds > 20 m/s in mid-levels in both stations. The water vapor supply was similar on the compared days, with a PW of 39.5 mm and 30.3 mm on the 25th of February of 2017 at Santo Domingo and Mendoza, respectively, compared to 35.1 and 22.6 mm on the same stations (Figures 4.12 and 4.13).

The upper air comparison of temperature reveals that the station near Mendoza presented, on average, more significant biases of 1°C compared to Santo Domingo for the February 2017 event (Fig. 4.12). In Santo Domingo, the errors oscillate around zero in all the profiles up to 300 hPa; however, Mendoza presents a warm bias near the surface and a better representation at mid-levels ($\sim$ 500 hPa). A similar behavior is observed for the specific humidity at high levels (near the surface) with negative humidity biases in both stations. The WRF-C simulations give the best representation of the profile on February 25, but this behavior is not maintained for all the days and time steps. The wind speed

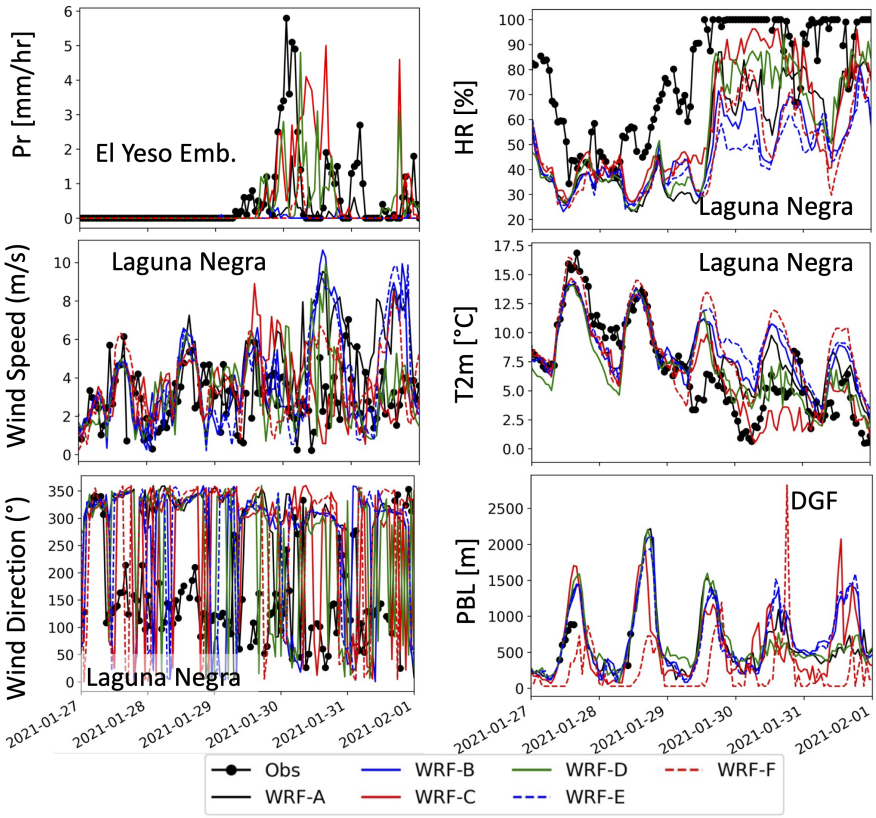

Figure 4.11: Same as Fig. 4.10 but for Jan 2021 event.

biases are larger in Mendoza ($\sim$ 2.5 m/s) than in Santo Domingo ($\sim$ 1.5 m/s). In this case, WRF-C simulations presented better metrics in Santo Domingo for all the evaluated days. In contrast, in Mendoza, no simulation excels during all the metrics and events (not shown).

In the case of the January 2021 event, the simulations capture the conditions at the Mendoza station more accurately than at the Santo Domingo station regarding temperature and specific humidity. The air temperature biases in Santo Domingo reach up to 2 $°C$ in the WRF-F simulations, while in Mendoza, the larger bias is 0.8 $°C$ in the WRF-C run. The humidity in all the profiles presents an underestimation of up to -3.5 gr/kg in Santo Domingo and -1.5 gr/Kg in Mendoza for the WRF-F scheme; however, the correlation in Mendoza reaches up to 0.912 at that station, while the coastal station gets 0.735, both in the WRF-D scheme. Finally, the wind speed is not well captured by the model with biases around $\sim$ 5 m/s at both stations for all the tested schemes (Fig. 4.13).

The AMDAR air temperature profiles at 16 UTC reveal a warming signal during all the days $<$ 10 °C, decreasing to $<$ 5 °C in mid-levels. The RMSE of the hourly-averaged air temperature profiles shows enhanced bias between 15 UTC and 23 UTC, with a minimum bias at 12 UTC during all the observations and simulations. The WRF-B simulations perform

Table 4.5: Evaluation metrics for PBL Height at DGF station.

WRF Configuration	RMSE [m]	r	Bias [m]	RMSE [m]	r	Bias [m]
	Feb 2017			Jan 2021		
A-Base	164	0.74	-44	254	0.85	180
B-Lin MP	165	0.74	-49	224	0.87	165
C-MM5-YSU SF-PBL	200	0.87	98	396	0.87	263
D-Noah LSM	166	0.81	-52	276	0.88	180
E-Thompson MP	144	0.8	-27	239	0.87	161
F-Janjic SF-PBL	619	0.56	-588	558	0.71	-540

the mean RMSE of air temperature among the hourly series (Fig. 4.14).

During the wind speed profiles at Fig. 4.15, simulations are somehow disconnected from the observations, similar to the sounding evaluation, with biases $\sim$ 4 m/s in low levels. Within the hourly evaluation, the biases are maximum between 18 and 23 UTC, similar to the temperature biases, reaching a maximum RMSE $>$ 8 m/s in all the simulations. However, the WRF-C simulations better represented the observed wind profiles. The wind direction of AMDAR observations was not evaluated.

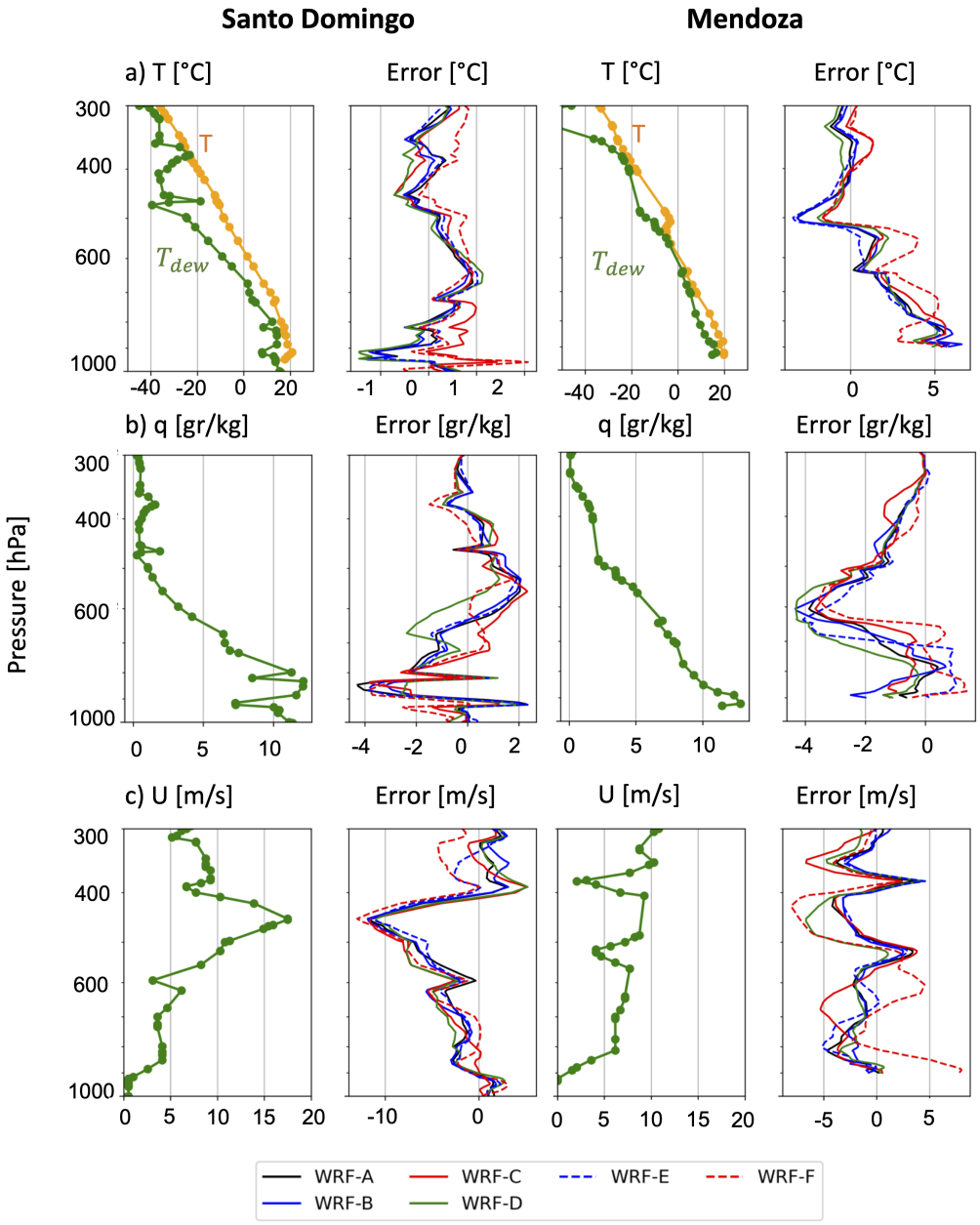

Figure 4.12: Upper air sounding and errors ($Y - X$, where Y is the simulated field, and X the interpolated observation) for February 25th, 2017, at 12 UTC, in the Santo Domingo (left panels) and Mendoza stations (right panels). The green line is observed: a) dewpoint temperature (T_{dew}, b) Specific humidity (q), and c) Wind speed (U). The orange line is air temperature T

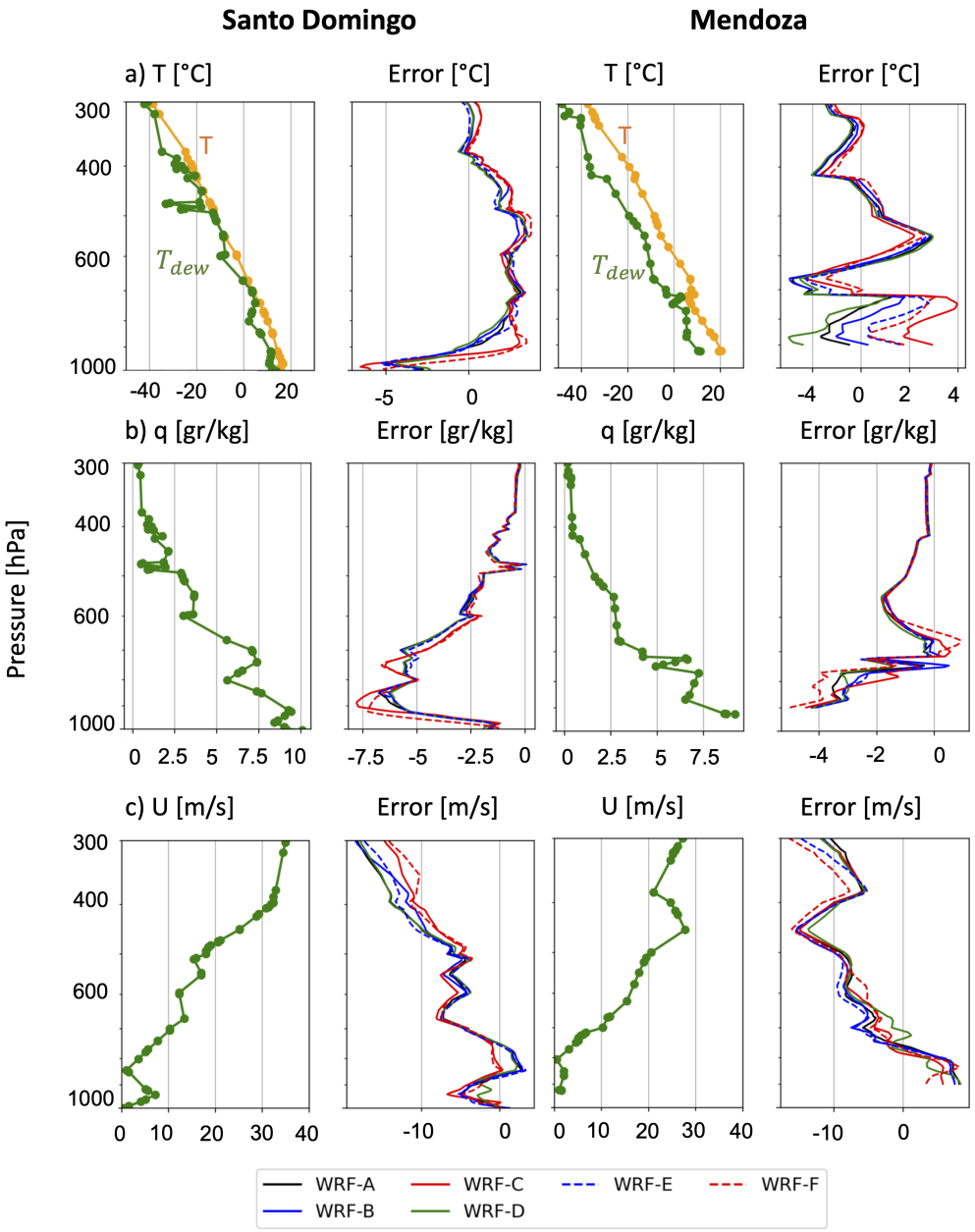

Figure 4.13: Same as Fig. 4.12 but for January 29, 2021 event at 12 UTC.

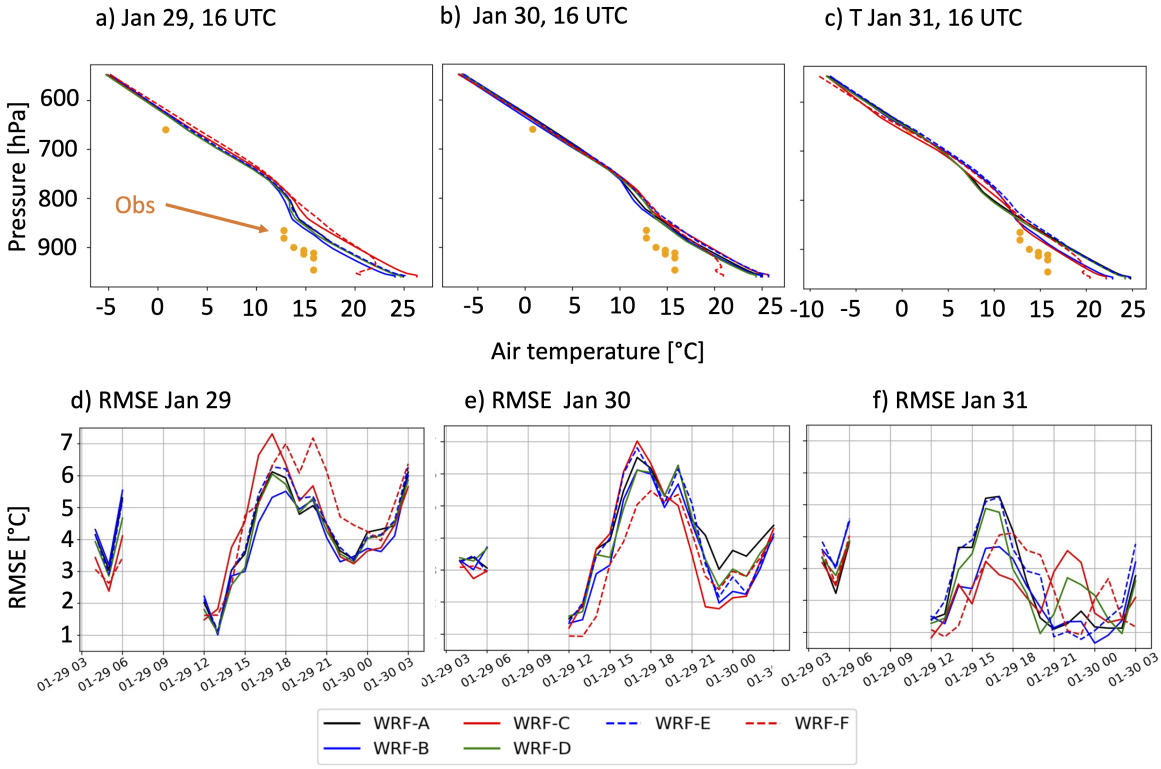

Figure 4.14: a-c) Observed (AMDAR) and simulated (WRF) air temperature profiles between January 29th and January 31 at 16 UTC (12 Local time). d-f) Shows the RMSE of hourly AMDAR temperature profiles during the same days.

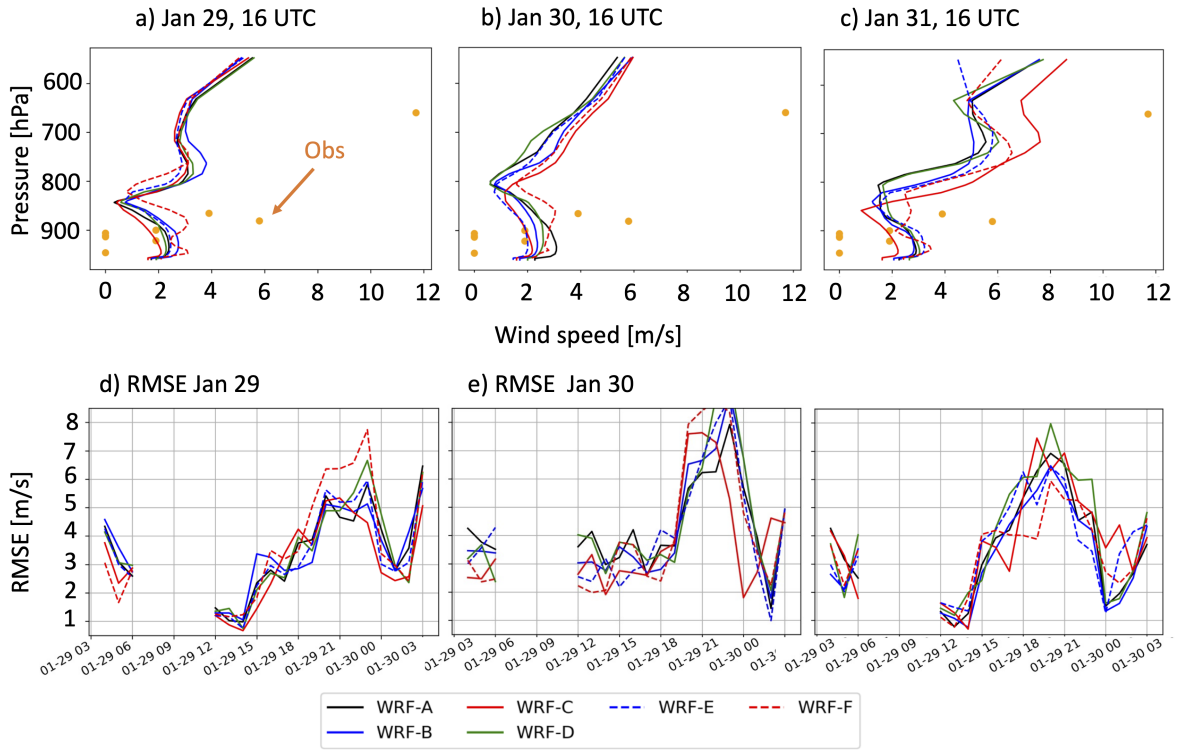

Figure 4.15: a-c) Observed (AMDAR) and simulated (WRF) wind speed profiles between January 29th and January 31 at 16 UTC (12 Local time). d-f) Shows the RMSE of hourly AMDAR wind speed profiles during the same days.

4.4.2 Ongoing efforts: SST warming experiment

wind and water vapor change

The integrated Vapor Transport (IVT) change simulated by the PGW experiment of the Jan 2021 event reveals an increase in IVT under warmer conditions, reaching up to 55 $Kgm^{-1}s^{-1}$. In contrast, this presented a peak of 45 $Kgm^{-1}s^{-1}$ in the historical conditions. Furthermore, the extent of domain with IVT values larger than 20 $Kgm^{-1}s^{-1}$ expands to lower latitudes than in the historical conditions, which may have implications for northern latitudes (Fig. 4.16), as observed in the Atacama Floods driven by extraordinary SST conditions (Bozkurt et al., 2016). This phenomenon warrants further exploration.

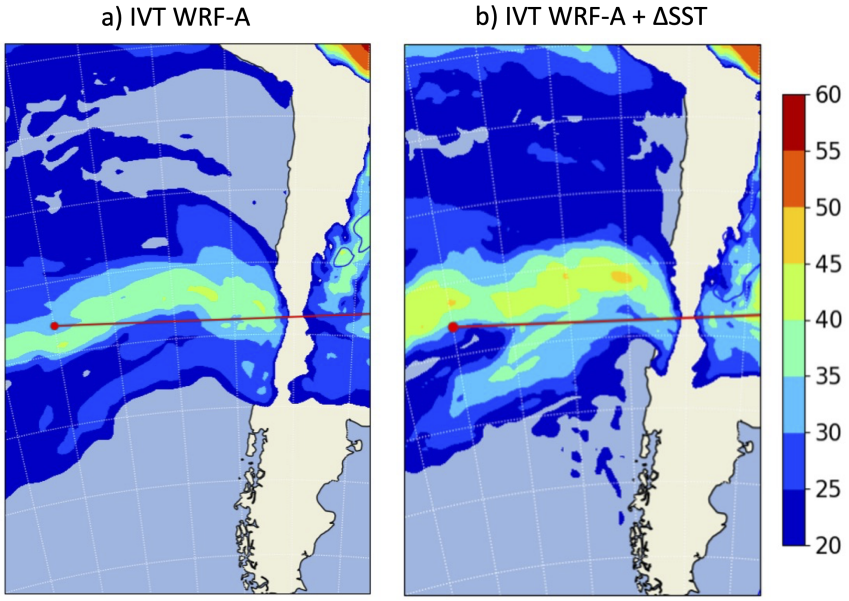

Figure 4.16: IVT projection in the outer domain for the Jan 2021 event at 18 UTC (15 hrs local time).

To gain insight into the change in dynamics, we explored results on January 29 at 15:00 local time, when the convection layer is most vigorous. The cross-sections shown in Fig. 4.17a-b reveal that the high-level zonal jet reaches lower elevations ($\sim$ 4000 m a.s.l.) compared to historical conditions. The meridional winds also present a change, developing a low-level northern jet in Argentina, utterly different from the historical simulations' neutral to the southern winds (Fig. 4.17c-d). The vertical winds also show more variability, indicating an enhancement of gravitational waves crossing the Andes (see Fig. 4.18); however, near the surface, changes in vertical motion are less than one m/s.

The water vapor availability change due to warmer SST conditions reveals wetter conditions near the Pacific coast and in mid-elevation altitudes, $\sim$ 3000 m a.s.l., and on the eastern slope of the Andes with differences greater than 2 gr/kg (Fig. 4.19). The PGW experiment also reveals more unstable conditions and higher freezing levels, observed in the time series depicted in Fig. 4.20, obtained by averaging the analyzed cross-section. These

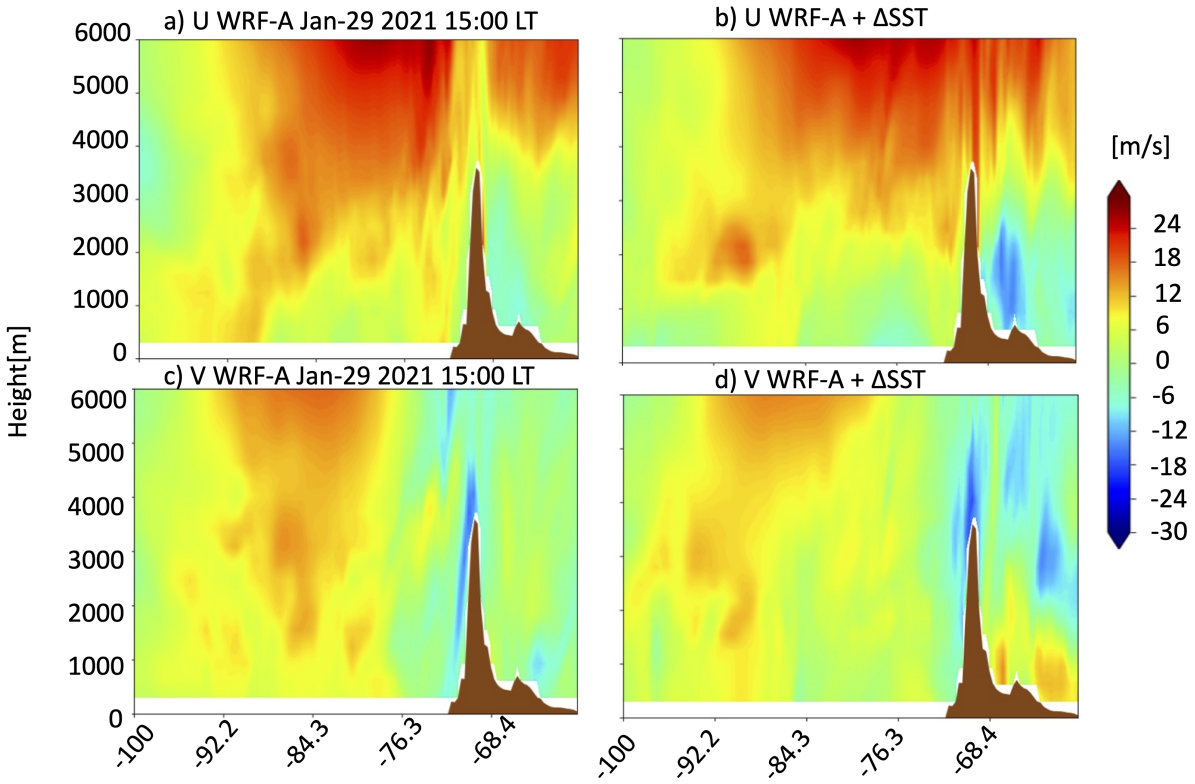

Figure 4.17: a,b) zonal and c,d) meridional winds simulated by WRF-A (left) and WRF-A + Δ SST (right), for the Jan 2021 event at 18 UTC in the transect shown in Fig. 4.16 for Dom 01.

conditions reflect the enhanced near-surface turbulence in the warmer simulation and lead to an expansion of areas affected by rainfall, intensifying the potential damage from such events.

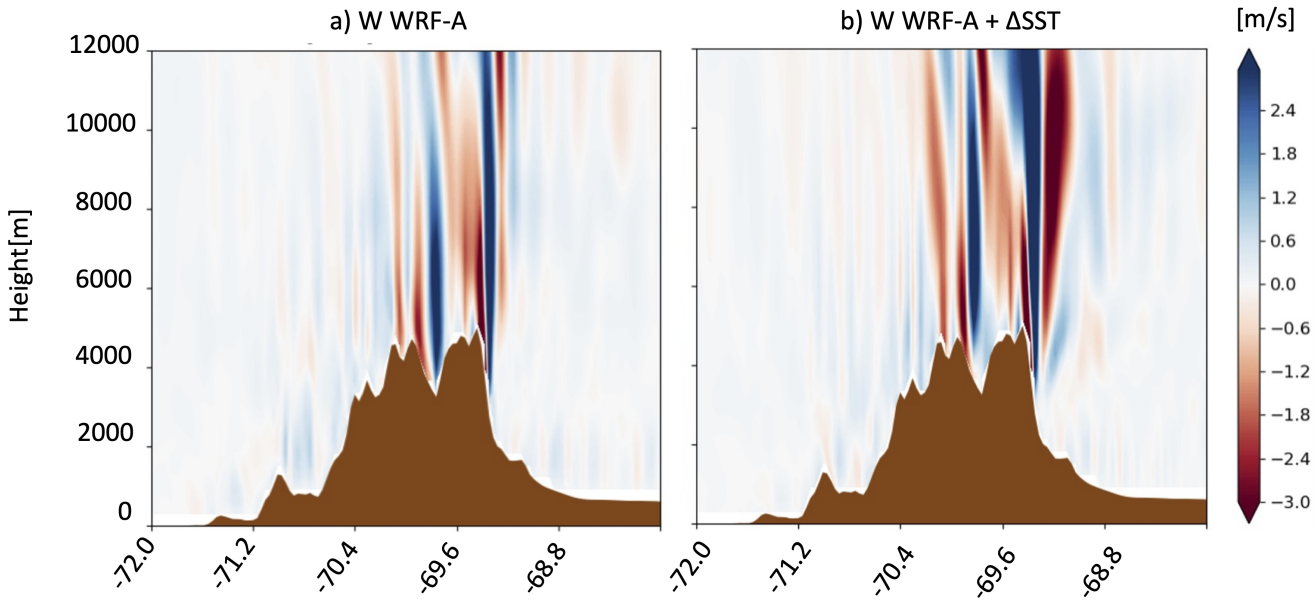

Figure 4.18: a) Vertical wind speed (W) simulated for the WRF-A scheme, and b) by WRF-A + ΔSST for the Jan 2021 event in the transect A-B at 18 UTC.

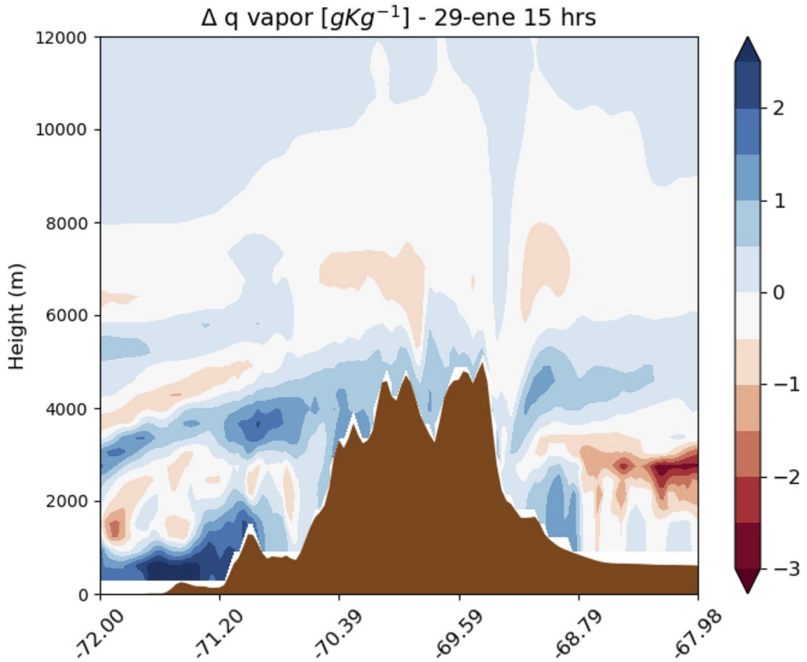

Figure 4.19: Specific humidity change for the Jan 2021 in the A-B transect.

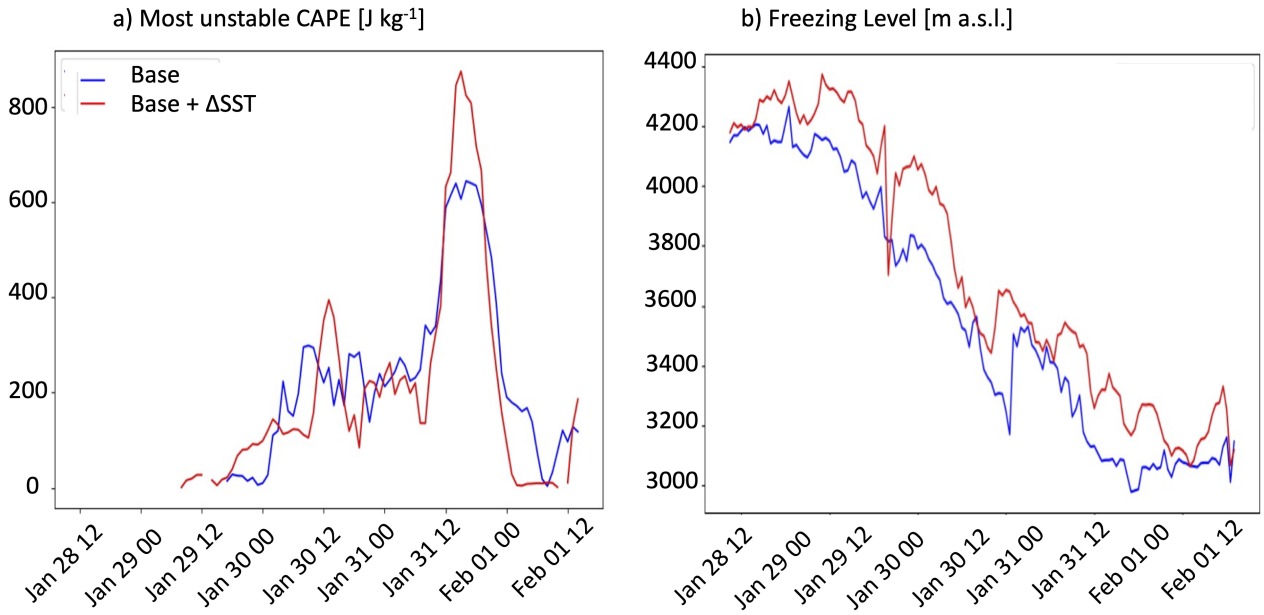

Figure 4.20: Most Unstable CAPE and freezing level for the Jan 2021 event in the transect A-B.

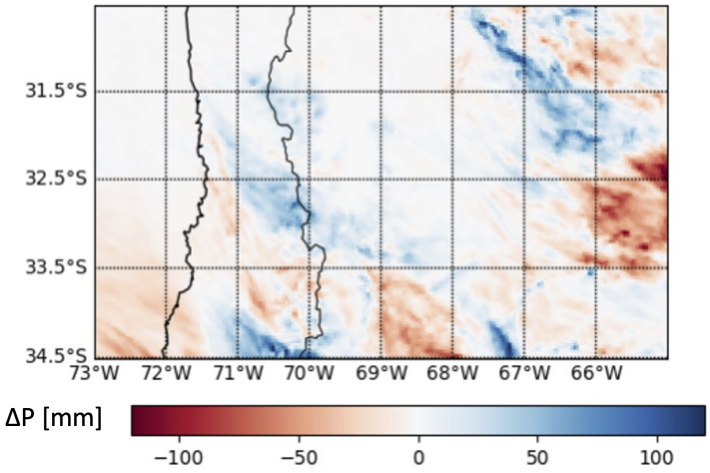

Figure 4.21: Changes in precipitation for the Jan 2021 event.

4.5 Concluding remarks

The simulated events show that precipitation production is highly sensitive to the microphysics, PBL, surface layer, and LSM schemes, particularly regarding its magnitude. This sensitivity is evident during both events and can be attributed to differences in wind patterns and cloud fractions obtained in different sensitivity simulations. Overall, the differences obtained in the representation of 2D and 3D simulated fields reveal that no model configuration excels in all the metrics; therefore, the WRF simulations, even with the Convection-permitting process activated, can hardly reproduce the observed precipitation. However, regarding the representation of precipitation and temperature in the two examined events, the WRF-C and WRF-D configurations presented the closest values compared to the observations.

Warmer SST conditions impact thermodynamic and dynamic aspects such as:

- Higher water vapor availability
- Intensification of 3D wind speeds and directional changes in horizontal winds on the eastern slopes of the Andes.
- Vertical motions near the Andes are affected, with some inhibition observed in the coastal cordillera and Central Valley.
- Precipitation intensification in the mountain zones and less precipitation in the coastal regions and the Pacific Ocean.
- Rising freezing levels and enhanced precipitation would lead to an enhanced risk of landslides and floods during summer precipitation.

This study underscores that the adopted schemes in the extratropical Andes could have impacts on climate outcomes similar to or greater than those projected by existing climate change studies; the latter reinforces the necessity to evaluate more events and more extended simulations to serve as guidelines to more robust conclusions under warmer conditions and to improve the forecast in extreme precipitation events. Future efforts should also deepen the analysis of the resolution of the model (horizontal and vertical), the use of new adaptative geometries in models to reduce the computational cost of nested domain (e.g., the ICON model Giorgetta et al., 2018). The efficiency of high-performance computing could facilitate a broader analysis of historical and future scenarios in complex topographic regions such as the Andes.

4.5.1 Limitations and future work

Even when the WRF-C and WRF-D simulations more realistically represented the observed precipitation fields, the warmer SST simulation was performed on the WRF-A model as a first step of sensitivity analysis. A publication in preparation of this chapter will include future climate experiments with the most accurate schemes to conclude about the change

of signal in precipitation, reaching out to the influence of schemes on its magnitude and affectation surfaces.

The assessment of precipitation simulations during the studied events did not consider biases of the boundary conditions in moisture and wind. Therefore, some differences between the observations and simulations may be explained by the lack of moisture convergence in the low levels, which should be further explored. Additionally, some of the detected differences may be explained by analyzing the moisture balance within specific regions to understand the sources of differences, e.g., surface evaporation, humid convergence, and precipitation, among others.

Because of the potential biases and inaccurate inflow to the WRF domain of vapor, the relation between hourly series may not be linear, and considering the Spearman correlation rank may complement the evaluation of the simulations. Additionally, the relative humidity assessment is influenced by temperature biases, which are somehow corrected by the considered humid lapse rate in Eq. 4.1, but is not corrected to surface-specific humidity. This variable should be evaluated as complementary.

The warmer SST experiment induces an extra surface instability; this is not necessarily a realistic experiment but may enhance the role of warm SST in the production of extreme precipitation as seen in Bozkurt et al. (2016); however, future experiments should consider changes in air temperature, moisture, and dynamic aspect, following, for example, a Pseudo Global Warming as performed in other CPCM efforts in past and future scenarios (e.g. Dominguez et al., 2023).

Regarding which surface process is more sensitive to generating precipitation, it is important to consider that some configurations, such as the WRF-C scheme, change the surface layer and the PBL because the YSW scheme does not work with the MYNN surface parametrization. Therefore, we could not interpret which process is more relevant to representing the simulated precipitation better in this scheme.

Chapter 5

Conclusions

This thesis contributes to understanding the physical mechanisms associated with recent climatic trends of extreme daily seasonal precipitation across continental Chile, associated temperatures, and possible mechanisms associated with its variations (Chapter 2). Chapter 3 reviews climate change projections of Regional Climate Models in the sub-tropical Andes (30-35°S), analyzing seasonal precipitation and extreme daily precipitation, looking for an explanation of the climate disagreement of precipitation changes in the domain; for that purpose, we analyze the simulated instability of the troposphere in different latitudinal bands finding strong connection between instability and convective-precipitation dominated areas. Finally, in Chapter 4, different convection-permitting climate model schemes were tested on two summer precipitation events with different synoptic genesis, Cut-Off Low and Atmospheric River, to explore insights into climate change signals to warmer Sea Surface Temperatures. The main findings of this thesis are summarized as follows:

- There is evidence of trends in seasonal extreme precipitation across Chile. With positive tendencies $\sim$ 30°S in fall, $\sim$ 35 in summer, and south of 45°S in almost all the seasons. Additionally, a robust drying signal was found in central Chile in all the seasons; however, a warming signal was detected between 30-35° during winter, the season with more significant precipitation for these latitudes, which may produce more intense floods.

- The intensification in summer Rx1day may be associated with air moistening in these latitudes, warmer SST conditions, and more CAPE available in the north of Chile. The negative trends in central Chile can be related to the poleward expansion of the Hadley Cell, the circulation induced by the Southern Blob, and a decrease in ARs landing these latitudes. The austral intensification of Rx1day is associated with an intensification of the storm track reflected in the intensification of the EKE.

- Seasonal Rx1day precipitation projections presented an opposite behavior of seasonal precipitation. The strong drying signal projected by their driving GCM is maintained between the fall and spring seasons.

- The RCM projections analyzed present heterogeneous behavior with the projected intensification of precipitation in the warm seasons of the north of Chile. This projection confirms the observer tendencies in the historical period. However, some models project an enhancement of seasonal Rx1day for the western Andes in the 30-35°S.

- Considering the potential instability as a proxy, it can explain the positive change of seasonal precipitation rather than extreme events, except the eastern slope of the Andes between 30-35°S during almost all seasons.

- The tested CPCM simulations reveal a strong influence in the microphysics, PBL, surface layer, and Land Surface Model to reproduce observed precipitation, temperature, winds, and PBLH, as well as upper air observations. Even when none of the schemes excels in all metrics and fields, the WRF-C and WRF-D schemes presented the more realistic representation of precipitation in the COL Feb 2017 and AR Jan 2021 events.

- The warmer SST conditions in the AR January 2021 event reveal impacts in dynamics and humidity together with enhanced instability and higher freezing levels. Future simulations show IVT and precipitation reaching northern latitudes compared to historical conditions. An aspect that should be further explored.

5.1 Limitations

Regarding the observational trends, the primary source of uncertainty is the lack of homogeneous datasets for temperature; spatially distributed different land cover and elevation are still needed to produce a regionalization of this field. Upper air observations inland will also allow the understanding of the troposphere behavior for different precipitation events, and, of course, more reliable measurements of total precipitation in the Mountains will permit a more realistic observation dataset to evaluate the headwaters in the Andes, reaching out diverse geophysical, and environmental sciences topics and its contribution to the population and downstream ecosystems.

Despite some insights in explaining the seasonal change of precipitation simulated by Regional Climate Models, the large heterogeneity of results from the driving GCM, different parameterizations, and lack of representativeness at high-resolution scales in complex terrains and convective scales still need to be studied. In this study, some schemes were tested in two summer precipitation events; however, a long-term simulation, considering land-surface feedbacks such as moisture exchange between the soil and the atmosphere, is still needed to generate more reliable simulations in the studied region.

Regarding the Convection-Permitting event simulations, there is a trade-off between the schemes, and resolving a larger period, including more events, will allow us to draw more robust conclusions. An aspect to highlight is that the PGW simulations present patterns of change similar to the ones obtained by choosing different schemes. To overcome this issue, additional PGW runs are needed for the best-performing schemes to evaluate the impact of the projections of warm precipitation events in the extratropical Andes. The study indicates significant sensitivity to the chosen microphysics, PBL, and LSM schemes. Still, these sensitivities' impact on future climate projections needs deeper analyses, and more PGW experiments could help identify which model components most influence the outcomes and where model improvements are most needed.

The analysis of warming conditions was only conducted for SST; this approach does not directly account for shifts in extratropical dynamics that influence baroclinic circulations, wave breaking, and large-scale circulations, which are crucial for understanding phenomena like COLs and ARs. In addition, modifications in water vapor transport from the subtropics/tropics significantly affect ARs frequency and intensity, a factor not directly captured by the current approach.

5.2 Future work

Future efforts will include the evaluation of horizontal and vertical resolution in CPCM simulations for the studied summer precipitation events to set a suitable scheme appropriate for reproducing summer precipitation events and evaluate future climate conditions through more extended simulations, including warmer conditions. Additionally, including all perturbations in the PGW scheme, such as air temperature, specific humidity, and geopotential height, will result in more realistic and coherent behavior in future scenarios. Another opportunity to explore is the intercomparison of CPCM simulations available in the region, including the SAAG-WRF initiative (Dominguez et al., 2023), the Hadley-Center simulations (Halladay et al., 2023), and climate simulations performed in South America (Feijoó and Solman, 2022; Hodnebrog et al., 2022). The comprehensive assessment of climate simulations will help to reduce the uncertainty in climate model projections in a highly uncertain region such as the Andes.

Bibliography

24horas (2017). Aguas andinas anuncia corte masivo de agua en santiago a raíz de lluvias. *24Horas*, pages url: https://www.24horas.cl/nacional/aguas–andinas–anuncia–corte–masivo–de–agua–en–santiago–a–raiz–de–ll

Aceituno, P., Boisier, J. P., Garreaud, R., Rondanelli, R., and Rutllant, J. A. (2021). Climate and weather in chile. In *Water Resources of Chile*, pages 7–29. Springer.

Aleshina, M., Semenov, V., and Chernokulsky, A. (2021). A link between surface air temperature and extreme precipitation over russia from station and reanalysis data. *Environmental Research Letters*, 16(10):105004.

Alexander, L. V. (2016). Global observed long-term changes in temperature and precipitation extremes: A review of progress and limitations in ipcc assessments and beyond. *Weather and Climate Extremes*, 11:4–16.

Algarra, I., Nieto, R., Ramos, A. M., Eiras-Barca, J., Trigo, R. M., and Gimeno, L. (2020). Significant increase of global anomalous moisture uptake feeding landfalling atmospheric rivers. *Nature communications*, 11(1):1–7.

Allen, J. T., Karoly, D. J., and Walsh, K. J. (2014). Future australian severe thunderstorm environments. part ii: The influence of a strongly warming climate on convective environments. *Journal of Climate*, 27(10):3848–3868.

Alvarez-Garreton, C., Mendoza, P. A., Boisier, J. P., Addor, N., Galleguillos, M., Zambrano-Bigiarini, M., Lara, A., Puelma, C., Cortes, G., Garreaud, R., McPhee, J., and Ayala, A. (2018). The CAMELS-CL dataset: catchment attributes and meteorology for large sample studies – Chile dataset. *Hydrology and Earth System Sciences Discussions*.

Araya-Osses, D., Casanueva, A., Román-Figueroa, C., Uribe, J. M., and Paneque, M. (2020). Climate change projections of temperature and precipitation in chile based on statistical downscaling. *Climate Dynamics*, 54(9):4309–4330.

Arévalo, J., Marín, J. C., Díaz, M., Raga, G., Pozo, D., Córdova, A. M., and Baumgardner, D. (2023). Sensitivity of simulated conditions to different parameterization choices over complex terrain in central chile. *Atmosphere*, 15(1):10.

Barrett, B. S., Campos, D. A., Veloso, J. V., and Rondanelli, R. (2016). Extreme temperature and precipitation events in March 2015 in central and northern Chile. *Journal of Geophysical Research: Atmospheres*, 121:4563–4580.

Barrett, B. S., Garreaud, R. D., and Falvey, M. (2009). Effect of the Andes Cordillera on precipitation from a midlatitude cold front. *Monthly Weather Review*, 137(9):3092–3109.

Bauer, P., Thorpe, A., and Brunet, G. (2015). The quiet revolution of numerical weather prediction. *Nature*, 525(7567):47–55.

Beck, H. E., Wood, E. F., McVicar, T. R., Zambrano-Bigiarini, M., Alvarez-Garreton, C., Baez-Villanueva, O. M., Sheffield, J., and Karger, D. N. (2020). Bias correction of global high-resolution precipitation climatologies using streamflow observations from 9372 catchments. *Journal of Climate*, 33(4):1299–1315.

Blázquez, J. and Nuñez, M. N. (2013). Analysis of uncertainties in future climate projections for south america: comparison of wcrp-cmip3 and wcrp-cmip5 models. *Climate Dynamics*, 41(3-4):1039–1056.

Bohren, C. and Albrecht, B. (1998). Atmospheric thermodynamics oxford university press. *New York*.

Boisier, J. P., Alvarez-Garretón, C., Cepeda, J., Osses, A., Vásquez, N., and Rondanelli, R. (2018a). Cr2met: A high-resolution precipitation and temperature dataset for hydroclimatic research in chile. In *EGU General Assembly Conference Abstracts*, page 19739.

Boisier, J. P., Alvarez-Garreton, C., Cordero, R. R., Damiani, A., Gallardo, L., Garreaud, R. D., Lambert, F., Ramallo, C., Rojas, M., and Rondanelli, R. (2018b). Anthropogenic drying in central-southern chile evidenced by long-term observations and climate model simulations. *Elementa: Science of the Anthropocene*, 6.

Boisier, J. P., Rondanelli, R., Garreaud, R., and Muñoz, F. (2016a). Anthropogenic Contribution to the Southeast Pacific Precipitation Decline and Recent (2010-2015) Mega-Drought in Chile. *American Geophysical Union, Fall Meeting 2015, abstract id. H43E-1549*, 43:1–9.

Boisier, J. P., Rondanelli, R., Garreaud, R., and Muñoz, F. (2016b). Anthropogenic Contribution to the Southeast Pacific Precipitation Decline and Recent (2010-2015) Mega-Drought in Chile. *American Geophysical Union, Fall Meeting 2015, abstract id. H43E-1549*, 43:1–9.

Boogaard, H., Schubert, J., De Wit, A., Lazebnik, J., Hutjes, R., and Van der Grijn, G. (2020). Agrometeorological indicators from 1979 to present derived from reanalysis, version 1.0. *Copernicus Climate Change Service (C3S) Climate Data Store (CDS)*.

Bozkurt, D., Rojas, M., Boisier, J. P., Rondanelli, R., Garreaud, R., and Gallardo, L. (2019). Dynamical downscaling over the complex terrain of southwest south america: present climate conditions and added value analysis. *Climate Dynamics*, 53(11):6745–6767.

Bozkurt, D., Rojas, M., Pablo, J. P., and Valdivieso, J. (2018). Projected hydroclimate changes over Andean basins in central Chile from downscaled CMIP5 models under the low and high emission scenarios. *Climate Change*, 150:131–147.

Bozkurt, D., Rondanelli, R., Garreaud, R., and Arriagada, A. (2016). Impact of warmer eastern tropical pacific SST on the March 2015 atacama floods. *Monthly Weather Review*, 144(11):4441–4460.

Brönnimann, S., Rajczak, J., Fischer, E. M., Raible, C. C., Rohrer, M., and Schär, C. (2018). Changing seasonality of moderate and extreme precipitation events in the alps. *Natural Hazards and Earth System Sciences*, 18(7):2047–2056.

Buishand, T. (1984). Tests for detecting a shift in the mean of hydrological time series. *Journal of hydrology*, 73(1-2):51–69.

Burger, F., Brock, B., and Montecinos, A. (2018). Seasonal and elevational contrasts in temperature trends in central chile between 1979 and 2015. *Global and Planetary Change*, 162:136–147.

Burkey, J. (2021). Mann–kendall tau–b with sen's method (enhanced).

Campos, D. and Rondanelli, R. (2023). Enso-related precipitation variability in central chile: The role of large scale moisture transport. *Journal of Geophysical Research: Atmospheres*, 128(17):e2023JD038671.

Cerón, W. L., Andreoli, R. V., Kayano, M. T., Canchala, T., Ocampo-Marulanda, C., Avila-Diaz, A., and Antunes, J. (2022). Trend pattern of heavy and intense rainfall events in colombia from 1981–2018: A trend-eof approach. *Atmosphere*, 13(2):156.

Cerón, W. L., Kayano, M. T., Andreoli, R. V., Avila-Díaz, A., Ayes, I., Freitas, E. D., Martins, J. A., and Souza, R. A. (2021). Recent intensification of extreme precipitation events in the la plata basin in southern south america (1981–2018). *Atmospheric Research*, 249:105299.

Chemke, R., Ming, Y., and Yuval, J. (2022). The intensification of winter mid-latitude storm tracks in the southern hemisphere. *Nature climate change*, 12(6):553–557.

Clapeyron, É. (1834). Mémoire sur la puissance motrice de la chaleur. *Journal de l'École polytechnique*, 14:153–190.

Clausius, R. (1850). Über die bewegende kraft der wärme und die gesetze, welche sich daraus für die wärmelehre selbst ableiten lassen. *Annalen der Physik*, 155(3):368–397.

Colmet-Daage, A., Sanchez-Gomez, E., Ricci, S., Llovel, C., Borrell Estupina, V., Quintana-Seguí, P., Llasat, M. C., and Servat, E. (2018). Evaluation of uncertainties in mean and extreme precipitation under climate change for northwestern mediterranean watersheds from high-resolution med and euro-cordex ensembles. *Hydrology and Earth System Sciences*, 22(1):673–687.

Comin, A. N., Schumacher, V., Justino, F., and Fernandez, A. (2018). Impact of different microphysical parameterizations on extreme snowfall events in the southern andes. *Weather and climate extremes*, 21:65–75.

Compo, G. P., Whitaker, J. S., Sardeshmukh, P. D., Matsui, N., Allan, R. J., Yin, X., Gleason, B. E., Vose, R. S., Rutledge, G., Bessemoulin, P., et al. (2011). The twentieth century reanalysis project. *Quarterly Journal of the Royal Meteorological Society*, 137(654):1–28.

CR2, C. (2018). Simulaciones climáticas regionales y marco de evaluación de la vulnerabilidad. Technical report.

CR2, C. (2020). Explorador Climático.

Demaria, E. M., Maurer, E. P., Thrasher, B., Vicuña, S., and Meza, F. J. (2013). Climate change impacts on an alpine watershed in Chile: Do new model projections change the story? *Journal of Hydrology*, 502:128–138.

DGA (2017). Actualización del Balance Hídrico Nacional, SIT N° 417. Technical report, Direcció General de Aguas.

Dickinson, R. E., Errico, R. M., Giorgi, F., and Bates, G. T. (1989). A regional climate model for the western united states. *Climatic change*, 15:383–422.

Dominguez, F., Rasmussen, R., Liu, C., Ikeda, K., Prein, A., Varble, A., Arias, P. A., Bacmeister, J., Bettolli, M. L., Callaghan, P., et al. (2023). Advancing south american water and climate science through multi-decadal convection-permitting modeling. *Bulletin of the American Meteorological Society*.

Dudhia, J. (1989). Numerical study of convection observed during the winter monsoon experiment using a mesoscale two-dimensional model. *Journal of Atmospheric Sciences*, 46(20):3077–3107.

El Mostrador (2017). Tres muertos y 19 desaparecidos por aluviones en regiones centro y norte del país.

El Mostrador (2021). Fotoreportaje: Aluviín en el cajón del maipo.

Elliott, W. P. and Gaffen, D. J. (1991). On the utility of radiosonde humidity archives for climate studies. *Bulletin of the American Meteorological Society*, 72(10):1507–1520.

ESGF (2023). The earth system grid federation (esgf) portal. https://esg-dn1.nsc.liu.se/projects/esgf-liu/. [Accessed 30-11-2023].

Espinoza, J. C., Garreaud, R., Poveda, G., Arias, P. A., Molina-Carpio, J., Masiokas, M., Viale, M., and Scaff, L. (2020). Hydroclimate of the Andes Part I: Main Climatic Features. *Frontiers in Earth Science*, 8(March):1–20.

Falvey, M. and Garreaud, R. (2007). Wintertime precipitation episodes in Central Chile: Associated meteorological conditions and orographic influences. *Journal of Hydrometeorology*, 8(2):171–193.

Falvey, M. and Garreaud, R. D. (2009a). Regional cooling in a warming world: Recent temperature trends in the southeast Pacific and along the west coast of subtropical South America (1979-2006). *Journal of Geophysical Research Atmospheres*, 114(4):1–16.

Falvey, M. and Garreaud, R. D. (2009b). Regional cooling in a warming world: Recent temperature trends in the southeast Pacific and along the west coast of subtropical South America (1979-2006). *Journal of Geophysical Research Atmospheres*, 114(4):1–16.

Feijoó, M. and Solman, S. (2022). Convection-permitting modeling strategies for simulating extreme rainfall events over southeastern south america. *Climate Dynamics*, 59(9):2549–2569.

Feldmann, H., Schädler, G., Panitz, H.-J., and Kottmeier, C. (2013). Near future changes of extreme precipitation over complex terrain in central europe derived from high resolution rcm ensemble simulations. *International Journal of Climatology*, 33(8):1964–1977.

Fischer, E. M. and Knutti, R. (2016). Observed heavy precipitation increase confirms theory and early models. *Nature Climate Change*, 6(11):986–991.

Fowler, H. J., Lenderink, G., Prein, A. F., Westra, S., Allan, R. P., Ban, N., Barbero, R., Berg, P., Blenkinsop, S., Do, H. X., et al. (2021). Anthropogenic intensification of short-duration rainfall extremes. *Nature Reviews Earth & Environment*, 2(2):107–122.

Fuenzalida, H., Falvey, M., Rojas, M., Sánchez, R., Garreaud, R., and Aceituno, P. (2006). Technical report (in spanish). estudio de variabilidad climática en chile para el siglo xxi. cambios climáticos regionales para fines del siglo xxi obtenido mediante el modelo precis. Technical report.

Funk, C., Peterson, P., Landsfeld, M., Pedreros, D., Verdin, J., Shukla, S., Husak, G., Rowland, J., Harrison, L., Hoell, A., et al. (2015). The climate hazards infrared precipitation with stations—a new environmental record for monitoring extremes. *Scientific data*, 2(1):1–21.

Garreaud, R. (2000). Intraseasonal variability of moisture and rainfall over the south american altiplano. *Monthly Weather Review*, 128(9):3337–3346.

Garreaud, R. (2009). The Andes climate and weather. *Advances In Geosciences*, 7:9.

Garreaud, R. (2017). Análisis: Un (nuevo) evento hidrometeorológico previsto pero igual ocurrió una catástrofe.

Garreaud, R. and Aceituno, P. (2001). Interannual rainfall variability over the south american altiplano. *Journal of climate*, 14(12):2779–2789.

Garreaud, R., Falvey, M., and Montecinos, A. (2016). Orographic precipitation in coastal southern chile: Mean distribution, temporal variability, and linear contribution. *Journal of Hydrometeorology*, 17(4):1185–1202.

Garreaud, R. D., Clem, K., and Veloso, J. V. (2021). The south pacific pressure trend dipole and the southern blob. *Journal of Climate*, 34(18):7661–7676.

Gateño, F., Mendoza, P. A., Vásquez, N. A., Jiménez, H., Jerez, C., Lagos-Zúñiga, M., Vargas, X., Rubio-Álvarez, E. A., and Montserrat, S. (2023). Evaluating cmip6 models for climate impact assessments in chile. *Authorea Preprints*.

Giorgetta, M. A., Brokopf, R., Crueger, T., Esch, M., Fiedler, S., Helmert, J., Hohenegger, C., Kornblueh, L., Köhler, M., Manzini, E., et al. (2018). Icon-a, the atmosphere component of the icon earth system model: I. model description. *Journal of Advances in Modeling Earth Systems*, 10(7):1613–1637.

Giorgi, F. and Bates, G. T. (1989). The climatological skill of a regional model over complex terrain. *Monthly Weather Review*, 117(11):2325–2347.

Giorgi, F., Coppola, E., Solmon, F., Mariotti, L., Sylla, M., Bi, X., Elguindi, N., Diro, G., Nair, V., Giuliani, G., et al. (2012). Regcm4: model description and preliminary tests over multiple cordex domains. *Climate Research*, 52:7–29.

Giorgi, F., Raffaele, F., and Coppola, E. (2019). The response of precipitation characteristics to global warming from climate projections. *Earth System Dynamics*, 10(1):73–89.

Giorgi, F., Torma, C., Coppola, E., Ban, N., Schär, C., and Somot, S. (2016). Enhanced summer convective rainfall at Alpine high elevations in response to climate warming. *Nature Geoscience*, 9(8):584–589.

Grell, G. A. (1993). Prognostic evaluation of assumptions used by cumulus parameterizations. *Monthly weather review*, 121(3):764–787.

Grise, K. M. and Davis, S. M. (2020). Hadley cell expansion in cmip6 models. *Atmospheric Chemistry and Physics*, 20(9):5249–5268.

Grose, M. R., Syktus, J., Thatcher, M., Evans, J. P., Ji, F., Rafter, T., and Remenyi, T. (2019). The role of topography on projected rainfall change in mid-latitude mountain regions. *Climate Dynamics*, 53:3675–3690.

Guan, B. and Waliser, D. E. (2015). Detection of atmospheric rivers: Evaluation and application of an algorithm for global studies. *Journal of Geophysical Research: Atmospheres*, 120(24):12514–12535.

Guerreiro, S. B., Fowler, H. J., Barbero, R., Westra, S., Lenderink, G., Blenkinsop, S., Lewis, E., and Li, X.-F. (2018). Detection of continental-scale intensification of hourly rainfall extremes. *Nature Climate Change*, 8(9):803–807.

Gutiérrez, J. M., Jones, R., Narisma, G., et al. (2021). Ipcc interactive atlas. *Climate change*.

Gutowski Jr, W. J., Giorgi, F., Timbal, B., Frigon, A., Jacob, D., Kang, H.-S., Krishnan, R., Lee, B., Lennard, C., Nikulin, G., et al. (2016). Wcrp coordinated regional downscaling experiment (cordex): a diagnostic mip for cmip6.

Halladay, K., Kahana, R., Johnson, B., Still, C., Fosser, G., and Alves, L. (2023). Convection-permitting climate simulations for south america with the met office unified model. *Climate Dynamics*, 61(11):5247–5269.

Hardwick Jones, R., Westra, S., and Sharma, A. (2010). Observed relationships between extreme sub-daily precipitation, surface temperature, and relative humidity. *Geophysical Research Letters*, 37(22).

He, J. and Soden, B. J. (2017). A re-examination of the projected subtropical precipitation decline. *Nature Climate Change*, 7(1):53–57.

Hersbach, H., Bell, B., Berrisford, P., Hirahara, S., Horányi, A., Muñoz-Sabater, J., Nicolas, J., Peubey, C., Radu, R., Schepers, D., et al. (2020). The era5 global reanalysis. *Quarterly Journal of the Royal Meteorological Society*, 146(730):1999–2049.

Hodnebrog, Ø., Steensen, B., Marelle, L., Alterskjær, K., Dalsøren, S. B., and Myhre, G. (2022). Understanding model diversity in future precipitation projections for south america. *Climate Dynamics*, 58(5-6):1329–1347.

Hong, S.-Y., Dudhia, J., and Chen, S.-H. (2004). A revised approach to ice microphysical processes for the bulk parameterization of clouds and precipitation. *Monthly weather review*, 132(1):103–120.

Hong, S.-Y., Noh, Y., and Dudhia, J. (2006). A new vertical diffusion package with an explicit treatment of entrainment processes. *Monthly weather review*, 134(9):2318–2341.

Hong, S.-Y., Sunny Lim, K.-S., Kim, J.-H., Jade Lim, J.-O., and Dudhia, J. (2009). Sensitivity study of cloud-resolving convective simulations with wrf using two bulk microphysical parameterizations: Ice-phase microphysics versus sedimentation effects. *Journal of Applied Meteorology and Climatology*, 48(1):61–76.

Hu, Y. and Fu, Q. (2007). Observed poleward expansion of the hadley circulation since 1979. *Atmospheric Chemistry and Physics*, 7(19):5229–5236.

Hu, Y., Zhou, C., and Liu, J. (2011). Observational evidence for poleward expansion of the hadley circulation. *Advances in Atmospheric Sciences*, 28(1):33–44.

Huang, B., Thorne, P. W., Banzon, V. F., Boyer, T., Chepurin, G., Lawrimore, J. H., Menne, M. J., Smith, T. M., Vose, R. S., Zhang, H.-M., et al. (2017). Noaa extended reconstructed sea surface temperature (ersst), version 5. *NOAA National Centers for Environmental Information*, 30(8179-8205):25.

Huang, Y., Xue, M., Hu, X.-M., Martin, E., Novoa, H. M., McPherson, R. A., Perez, A., and Morales, I. Y. (2023). Convection-permitting simulations of precipitation over the peruvian central andes: Strong sensitivity to planetary boundary layer parameterization. *Journal of Hydrometeorology*, 24(11):1969–1990.

Huffman, G. J., Adler, R. F., Arkin, P., Chang, A., Ferraro, R., Gruber, A., Janowiak, J., McNab, A., Rudolf, B., and Schneider, U. (1997). The global precipitation climatology project (gpcp) combined precipitation dataset. *Bulletin of the american meteorological society*, 78(1):5–20.

Huffman, G. J., Bolvin, D. T., Braithwaite, D., Hsu, K. L., Joyce, R. J., Kidd, C., Nelkin, E. J., Sorooshian, S., Stocker, E. F., Tan, J., Wolff, D. B., and Xie, P. (2015). Integrated Multi-satellite Retrievals for the Global Precipitation Measurement (GPM) Mission (IMERG). *Advances in Global Change Research*, 67(March):343–353.

Ibañez, M., Gironás, J., Oberli, C., Chadwick, C., and Garreaud, R. D. (2021). Daily and seasonal variation of the surface temperature lapse rate and 0 c isotherm height in the western subtropical andes. *International Journal of Climatology*, 41:E980–E999.

Jacob, D., Bärring, L., Christensen, O. B., Christensen, J. H., De Castro, M., Deque, M., Giorgi, F., Hagemann, S., Hirschi, M., Jones, R., et al. (2007). An inter-comparison of regional climate models for europe: model performance in present-day climate. *Climatic change*, 81(1):31–52.

Janssen, E., Wuebbles, D. J., Kunkel, K. E., Olsen, S. C., and Goodman, A. (2014). Observational-and model-based trends and projections of extreme precipitation over the contiguous united states. *Earth's Future*, 2(2):99–113.

Juliá, C., Rahn, D. A., and Rutllant, J. A. (2012). Assessing the influence of the mjo on strong precipitation events in subtropical, semi-arid north-central chile (30 s). *Journal of Climate*, 25(20):7003–7013.

Karl, T. R., Nicholls, N., and Ghazi, A. (1999). Clivar/gcos/wmo workshop on indices and indicators for climate extremes workshop summary. *Weather and climate extremes: Changes, variations and a perspective from the insurance industry*, pages 3–7.

Katsafados, P., Mavromatidis, E., Papadopoulos, A., and Pytharoulis, I. (2011). Numerical simulation of a deep mediterranean storm and its sensitivity on sea surface temperature. *Natural Hazards and Earth System Sciences*, 11(5):1233–1246.

Kendall, M. G. (1948). Rank correlation methods.

Kotlarski, S., Gobiet, A., Morin, S., Olefs, M., Rajczak, J., and Samacoïts, R. (2023). 21st century alpine climate change. *Climate Dynamics*, 60(1-2):65–86.

Ladstädter, F., Steiner, A. K., and Gleisner, H. (2023). Resolving the 21st century temperature trends of the upper troposphere–lower stratosphere with satellite observations. *Scientific Reports*, 13(1):1306.

Lagos-Zúñiga, M., Balmaceda-Huarte, R., Regoto, P., Torrez, L., Olmo, M., Lyra, A., Pareja-Quispe, D., and Bettolli, M. L. (2022a). Extreme indices of temperature and precipitation in south america: trends and intercomparison of regional climate models. *Climate Dynamics*, pages 1–22.

Lagos-Zúñiga, M., Bozkurt, D., and Rondanelli, R. (2022b). Assessment of summer precipitation events through different convection-permitting wrf simulations in the central andes. In *American Geophysical Union fall meeting*.

Lagos-Zúñiga, M., Bozkurt, D., and Rondanelli, R. (2022c). A case study of climate sensitivity of ar-induced precipitation to warm sea surface temperatures. In *International Atmospheric Rivers Conference*.

Lagos-Zúñiga, M., Bozkurt, D., and Rondanelli, R. (2022d). Sensitivity of convective precipitation to warming in the extratropical andes. In *VI Convection-Permitting Climate Model Workshop*.

Lagos-Zúñiga, M., Mendoza, P. A., Campos, D., and Rondanelli, R. (2024). Trends in seasonal precipitation extremes and associated temperatures along continental chile. *Climate Dynamics*, pages 1–18.

Lagos-Zúñiga, M., Mendoza, P. A., and Rondanelli, R. (2021a). Are extreme precipitation events becoming stronger and warmer in the andes? In *EGU General Assembly Conference Abstracts*, pages EGU21–6967.

Lagos-Zúñiga, M., Pinto, D., Torrez, L., and Rondanelli, R. (2021b). ¿son las precipitaciones extremas estacionarias en chile? In *XXV Congreso Chileno de Ingeniería Hidráulica*.

Lagos-Zúñiga, M., Rondanelli, R., and Garreaud, R. (2021c). Procesos meteorológicos en eventos de precipitación y siplificaciones en ingeniería. buscando el equilivrio entre la física y la práctica. *Rutas Hidrológicas.* In Spanish, page 121.

Lagos-Zúñiga, M., Torrez, L., Regoto, P., Balmaceda-Huerta, R., Lyra, A., Olmo, M., Pareja, D., and Bettolli, M. L. (2021d). How well are rcms representing extreme indices in the sam region? In *American Geophysical Union fall meeting*.

Lagos-Zúñiga, M. Á. and Vargas-Mesa, X. (2014). Potential influences of climate change on pluvial floods in an andean watershed. *Tecnología y ciencias del agua*, 5(2):19–38.

Lagos-Zúñiga, Mendoza, P. A. and Rondanelli, R. (2022). ¿por qué están cambiando las precipitaciones máximas estacionales en chile continental?,. In *VI Congreso de Oceanografía física, meteorología y clima del Pacífico sur oriental*.

Laprise, R. (2008). Regional climate modelling. *Journal of Computational Physics*, 227(7):3641–3666.

Lee, D., Min, S.-K., Ahn, J.-B., Cha, D.-H., Shin, S.-W., Chang, E.-C., Suh, M.-S., Byun, Y.-H., and Kim, J.-U. (2023). Uncertainty analysis of future summer monsoon duration and area over east asia using a multi-gcm/multi-rcm ensemble. *Environmental Research Letters*, 18(6):064026.

Lenderink, G., Barbero, R., Loriaux, J., and Fowler, H. (2017). Super-clausius–clapeyron scaling of extreme hourly convective precipitation and its relation to large-scale atmospheric conditions. *Journal of Climate*, 30(15):6037–6052.

Lenderink, G., Mok, H., Lee, T., and Van Oldenborgh, G. (2011). Scaling and trends of hourly precipitation extremes in two different climate zones–hong kong and the netherlands. *Hydrology and Earth System Sciences*, 15(9):3033–3041.

Li, C., Zwiers, F., Zhang, X., Li, G., Sun, Y., and Wehner, M. (2021). Changes in annual extremes of daily temperature and precipitation in cmip6 models. *Journal of Climate*, 34(9):3441–3460.

Lin, Y.-L., Farley, R. D., and Orville, H. D. (1983). Bulk parameterization of the snow field in a cloud model. *Journal of Applied Meteorology and climatology*, 22(6):1065–1092.

Liu, C., Ikeda, K., Rasmussen, R., Barlage, M., Newman, A. J., Prein, A. F., Chen, F., Chen, L., Clark, M., Dai, A., et al. (2017). Continental-scale convection-permitting modeling of the current and future climate of north america. *Climate Dynamics*, 49:71–95.

Lundquist, J., Hughes, M., Gutmann, E., and Kapnick, S. (2019). Our skill in modeling mountain rain and snow is bypassing the skill of our observational networks. *Bulletin of the American Meteorological Society*, 100(12):2473–2490.

Ma, W., Chen, G., and Guan, B. (2020). Poleward shift of atmospheric rivers in the southern hemisphere in recent decades. *Geophysical Research Letters*, 47(21):e2020GL089934.

Machado Crespo, N., Reboita, M. S., Gozzo, L. F., de Jesus, E. M., Torres-Alavez, J. A., Lagos-Zúñiga, M. Á., Torrez-Rodriguez, L., Reale, M., and da Rocha, R. P. (2022). Assessment of the regcm4-cordex-core performance in simulating cyclones affecting the western coast of south america. *Climate Dynamics*, pages 1–19.

Manabe, S. and Wetherald, R. T. (1975). The effects of doubling the co 2 concentration on the climate of a general circulation model. *Journal of Atmospheric Sciences*, 32(1):3–15.

Mann, H. B. (1945). Nonparametric tests against trend. *Econometrica: Journal of the econometric society*, pages 245–259.

Mardones, P. and Garreaud, R. D. (2020). Future changes in the free tropospheric freezing level and rain–snow limit: The case of central chile. *Atmosphere*, 11(11):1259.

Markowski, P. and Richardson, Y. (2011). *Mesoscale meteorology in midlatitudes*, volume 2. John Wiley & Sons.

Martel, J.-L., Brissette, F. P., Lucas-Picher, P., Troin, M., and Arsenault, R. (2021). Climate change and rainfall intensity–duration–frequency curves: Overview of science and guidelines for adaptation. *Journal of Hydrologic Engineering*, 26(10):03121001.

Martel, J.-L., Mailhot, A., Brissette, F., and Caya, D. (2018). Role of natural climate variability in the detection of anthropogenic climate change signal for mean and extreme precipitation at local and regional scales. *Journal of Climate*, 31(11):4241–4263.

Martinez-Villalobos, C. and Neelin, J. D. (2023). Regionally high risk increase for precipitation extreme events under global warming. *Scientific Reports*, 13(1):5579.

Martinkova, M. and Kysely, J. (2020). Overview of observed clausius-clapeyron scaling of extreme precipitation in midlatitudes. *Atmosphere*, 11(8):786.

Massmann, A. K., Minder, J. R., Garreaud, R. D., Kingsmill, D. E., Valenzuela, R. A., Montecinos, A., Fults, S. L., and Snider, J. R. (2017). The chilean coastal orographic precipitation experiment: Observing the influence of microphysical rain regimes on coastal orographic precipitation. *Journal of Hydrometeorology*, 18(10):2723–2743.

May, R. M., Goebbert, K. H., Thielen, J. E., Leeman, J. R., Camron, M. D., Bruick, Z., Bruning, E. C., Manser, R. P., Arms, S. C., and Marsh, P. T. (2022). Metpy: A meteorological python library for data analysis and visualization. *Bulletin of the American Meteorological Society*, 103(10):E2273–E2284.

Mbienda, A. K., Guenang, G., Kaissassou, S., Tanessong, R., Choumbou, P., and Giorgi, F. (2023). Enhancement of regcm4. 7-clm precipitation and temperature by improved bias correction methods over central africa. *Meteorological Applications*, 30(1):e2116.

Meredith, E. P., Ulbrich, U., and Rust, H. W. (2019). The diurnal nature of future extreme precipitation intensification. *Geophysical Research Letters*, 46(13):7680–7689.

Mesinger, F., Chou, S. C., Gomes, J. L., Jovic, D., Bastos, P., Bustamante, J. F., Lazic, L., Lyra, A. A., Morelli, S., Ristic, I., et al. (2012). An upgraded version of the eta model. *Meteorology and Atmospheric Physics*, 116(3-4):63–79.

Meteored (2023). Tormentas de verano dejan aluviones, cortes de caminos y personas aisladas.

Mlawer, E. J., Taubman, S. J., Brown, P. D., Iacono, M. J., and Clough, S. A. (1997). Radiative transfer for inhomogeneous atmospheres: Rrtm, a validated correlated-k model for the longwave. *Journal of Geophysical Research: Atmospheres*, 102(D14):16663–16682.

Molnar, P., Fatichi, S., Gaál, L., Szolgay, J., and Burlando, P. (2015). Storm type effects on super clausius–clapeyron scaling of intense rainstorm properties with air temperature. *Hydrology and Earth System Sciences*, 19(4):1753–1766.

Moninger, W. R., Mamrosh, R. D., and Pauley, P. M. (2003). Automated meteorological reports from commercial aircraft. *Bulletin of the American Meteorological Society*, 84(2):203–216.

Moya-Álvarez, A. S., Gálvez, J., Holguín, A., Estevan, R., Kumar, S., Villalobos, E., Martínez-Castro, D., and Silva, Y. (2018). Extreme rainfall forecast with the wrf-arw model in the central andes of peru. *Atmosphere*, 9(9):362.

Mukherjee, S., Aadhar, S., Stone, D., and Mishra, V. (2018). Increase in extreme precipitation events under anthropogenic warming in india. *Weather and climate extremes*, 20:45–53.

Muñoz, C. and Schultz, D. M. (2021). Cutoff lows, moisture plumes, and their influence on extreme-precipitation days in central chile. *Journal of Applied Meteorology and Climatology*, 60(4):437–454.

Muñoz, R. C. and Undurraga, A. A. (2010). Daytime mixed layer over the santiago basin: Description of two years of observations with a lidar ceilometer. *Journal of Applied Meteorology and Climatology*, 49(8):1728–1741.

Muñoz, R. C., Whiteman, C. D., Garreaud, R. D., Rutllant, J. A., and Hidalgo, J. (2022). Using commercial aircraft meteorological data to assess the heat budget of the convective boundary layer over the santiago valley in central chile. *Boundary-Layer Meteorology*, 183(2):295–319.

Na, Y., Lu, R., Fu, Q., and Kodama, C. (2021). Precipitation characteristics and future changes over the southern slope of tibetan plateau simulated by a high-resolution global nonhydrostatic model. *Journal of Geophysical Research: Atmospheres*, 126(3):e2020JD033630.

Nakanishi, M. and Niino, H. (2006). An improved mellor–yamada level-3 model: Its numerical stability and application to a regional prediction of advection fog. *Boundary-Layer Meteorology*, 119:397–407.

Nguyen, P.-L., Bador, M., Alexander, L. V., Lane, T. P., and Ngo-Duc, T. (2022). More intense daily precipitation in cordex-sea regional climate models than their forcing global climate models over southeast asia. *International Journal of Climatology*, 42(12):6537–6561.

Niu, G.-Y., Yang, Z.-L., Mitchell, K. E., Chen, F., Ek, M. B., Barlage, M., Kumar, A., Manning, K., Niyogi, D., Rosero, E., et al. (2011). The community noah land surface model with multiparameterization options (noah-mp): 1. model description and evaluation with local-scale measurements. *Journal of Geophysical Research: Atmospheres*, 116(D12).

O'Neill, B. C., Kriegler, E., Riahi, K., Ebi, K. L., Hallegatte, S., Carter, T. R., Mathur, R., and van Vuuren, D. P. (2014). A new scenario framework for climate change research: The concept of shared socioeconomic pathways. *Climatic Change*, 122(3):387–400.

Ortega, C., Vargas, G., Rojas, M., Rutllant, J. A., Muñoz, P., Lange, C. B., Pantoja, S., Dezileau, L., and Ortlieb, L. (2019). Extreme ENSO-driven torrential rainfalls at the southern edge of the Atacama Desert during the Late Holocene and their projection into the 21th century. *Global and Planetary Change*, 175(September 2018):226–237.

Pal, I. and Al-Tabbaa, A. (2009). Trends in seasonal precipitation extremes–an indicator of 'climate change'in kerala, india. *Journal of Hydrology*, 367(1-2):62–69.

Paxian, A., Hertig, E., Seubert, S., Vogt, G., Jacobeit, J., and Paeth, H. (2015). Present-day and future mediterranean precipitation extremes assessed by different statistical approaches. *Climate dynamics*, 44:845–860.

Pei, F., Wu, C., Liu, X., Hu, Z., Xia, Y., Liu, L.-A., Wang, K., Zhou, Y., and Xu, L. (2018). Detection and attribution of extreme precipitation changes from 1961 to 2012 in the yangtze river delta in china. *Catena*, 169:183–194.

Pepin, N., Bradley, R. S., Diaz, H., Baraër, M., Caceres, E., Forsythe, N., Fowler, H., Greenwood, G., Hashmi, M., Liu, X., et al. (2015). Elevation-dependent warming in mountain regions of the world. *Nature climate change*, 5(5):424.

Pfahl, S., O'Gorman, P. A., and Fischer, E. M. (2017). Understanding the regional pattern of projected future changes in extreme precipitation. *Nature Climate Change*, 7(6):423–427.

Pilatin, H., Yucel, I., Duzenli, E., and Yilmaz, M. T. (2021). Sensitivity of wrf-derived hydrometeorological extremes to sea surface temperatures in regions with complex topography and diverse climate. *Atmospheric Research*, 264:105816.

Pool, S., Viviroli, D., and Seibert, J. (2019). Value of a Limited Number of Discharge Observations for Improving Regionalization: A Large-Sample Study Across the United States. *Water Resources Research*, 55(1):363–377.

Potter, B. E. and Anaya, M. A. (2015). A wildfire-relevant climatology of the convective environment of the united states. *International Journal of Wildland Fire*, 24(2):267–275.

Poveda, G., Espinoza, J. C., Zuluaga, M. D., Solman, S. A., Garreaud, R., and van Oevelen, P. J. (2020). High impact weather events in the andes. *Frontiers in Earth Science*, 8:162.

Prein, A. F., Holland, G. J., Rasmussen, R. M., Done, J., Ikeda, K., Clark, M. P., and Liu, C. H. (2013). Importance of regional climate model grid spacing for the simulation of heavy precipitation in the colorado headwaters. *Journal of climate*, 26(13):4848–4857.

Prein, A. F., Langhans, W., Fosser, G., Ferrone, A., Ban, N., Goergen, K., Keller, M., Tölle, M., Gutjahr, O., Feser, F., et al. (2015). A review on regional convection-permitting climate modeling: Demonstrations, prospects, and challenges. *Reviews of geophysics*, 53(2):323–361.

Prein, A. F. and Mearns, L. O. (2021). Us extreme precipitation weather types increased in frequency during the 20th century. *Journal of Geophysical Research: Atmospheres*, 126(7):e2020JD034287.

Rädler, A. T., Groenemeijer, P. H., Faust, E., Sausen, R., and Púčik, T. (2019). Frequency of severe thunderstorms across europe expected to increase in the 21st century due to rising instability. *npj Climate and Atmospheric Science*, 2(1):1–5.

Rasmussen, K. and Houze Jr, R. (2016). Convective initiation near the andes in subtropical south america. *Monthly Weather Review*, 144(6):2351–2374.

Reboita, M. S., Kuki, C. A. C., Marrafon, V. H., de Souza, C. A., Ferreira, G. W. S., Teodoro, T., and Lima, J. W. M. (2022). South america climate change revealed through climate indices projected by gcms and eta-rcm ensembles. *Climate Dynamics*, 58(1-2):459–485.

Regoto, P., Dereczynski, C., Chou, S. C., and Bazzanela, A. C. (2021). Observed changes in air temperature and precipitation extremes over brazil. *International Journal of Climatology*, 41(11):5125–5142.

Rondanelli, R., Hatchett, B., Rutllant, J., Bozkurt, D., and Garreaud, R. (2019). Strongest MJO on Record Triggers Extreme Atacama Rainfall and Warmth in Antarctica. *Geophysical Research Letters*, 46(6):3482–3491.

Ross, R. J. and Gaffen, D. J. (1998). Comment on "widespread tropical atmospheric drying from 1979 to 1995" by schroeder and mcguirk. *Geophysical Research Letters*, 25(23):4357–4358.

Rutllant, J. A., Matus, F., Rudloff, V., and Rondanelli, R. (2023). The role of atmospheric rivers in rainfall-induced landslides: A study from the elqui valley. *Journal of Arid Environments*, 216:105016.

Saavedra, F. A., Kampf, S. K., Fassnacht, S. R., and Sibold, J. S. (2018). Changes in andes snow cover from modis data, 2000–2016. *The Cryosphere*, 12(3):1027–1046.

Saide, P. E., Carmichael, G. R., Spak, S. N., Gallardo, L., Osses, A. E., Mena-Carrasco, M. A., and Pagowski, M. (2011). Forecasting urban pm10 and pm2. 5 pollution episodes in very stable nocturnal conditions and complex terrain using wrf–chem co tracer model. *Atmospheric Environment*, 45(16):2769–2780.

Salazar, Á., Thatcher, M., Goubanova, K., Bernal, P., Gutiérrez, J., and Squeo, F. (2024). Cmip6 precipitation and temperature projections for chile. *Climate Dynamics*, 62(3):2475–2498.

Sarricolea, P., Herrera-Ossandon, M., and Meseguer-Ruiz, Ó. (2017). Climatic regionalisation of continental chile. *Journal of Maps*, 13(2):66–73.

Sarricolea, P., Meseguer-Ruiz, Ó., Serrano-Notivoli, R., Soto, M. V., and Martin-Vide, J. (2019). Trends of daily precipitation concentration in central-southern chile. *Atmospheric research*, 215:85–98.

Scaff, L., Prein, A. F., Li, Y., Liu, C., Rasmussen, R., and Ikeda, K. (2019). Simulating the convective precipitation diurnal cycle in north america's current and future climate. *Climate Dynamics*, pages 1–14.

Scaff, L., Rutllant, J. A., Rahn, D., Gascoin, S., and Rondanelli, R. (2017). Meteorological interpretation of orographic precipitation gradients along an Andes west slope basin at 30°S (Elqui Valley, Chile). *Journal of Hydrometeorology*, 18(3):713–727.

Schulzweida, U., Kronblueh, L., and Budich, R. G. (2019). cdo: climate data operators.

Schumacher, V., Fernández, A., Justino, F., and Comin, A. (2020a). Wrf high resolution dynamical downscaling of precipitation for the central andes of chile and argentina. *Frontiers in Earth Science*, 8:328.

Schumacher, V., Justino, F., Fernández, A., Meseguer-Ruiz, O., Sarricolea, P., Comin, A., Peroni Venancio, L., and Althoff, D. (2020b). Comparison between observations and gridded data sets over complex terrain in the chilean andes: Precipitation and temperature. *International Journal of Climatology*, 40(12):5266–5288.

Seeley, J. T. and Romps, D. M. (2015). The effect of global warming on severe thunderstorms in the united states. *Journal of Climate*, 28(6):2443–2458.

Sen, P. K. (1968). Estimates of the regression coefficient based on kendall's tau. *Journal of the American statistical association*, 63(324):1379–1389.

Sharma, A., Wasko, C., and Lettenmaier, D. P. (2018). If Precipitation Extremes Are Increasing, Why Aren't Floods?

Shaw, T., Baldwin, M., Barnes, E. A., Caballero, R., Garfinkel, C., Hwang, Y.-T., Li, C., O'gorman, P., Rivière, G., Simpson, I., et al. (2016). Storm track processes and the opposing influences of climate change. *Nature Geoscience*, 9(9):656–664.

Sherwood, S. C. and Nishant, N. (2015). Atmospheric changes through 2012 as shown by iteratively homogenized radiosonde temperature and wind data (iukv2). *Environmental Research Letters*, 10(5):054007.

Shi, J., Cui, L., Wang, J., Du, H., and Wen, K. (2019). Changes in the temperature and precipitation extremes in china during 1961–2015. *Quaternary International*, 527:64–78.

Skamarock, W., Klemp, J., et al. (2019). A description of the advanced research wrf model version 4. ncar technical notes, no. Technical report, NCAR/TN-556+ STR.

Somos-Valenzuela, M. A., Oyarzún-Ulloa, J. E., Fustos-Toribio, I. J., Garrido-Urzua, N., and Chen, N. (2020). The mudflow disaster at villa santa lucía in chilean patagonia: understandings and insights derived from numerical simulation and postevent field surveys. *Natural Hazards and Earth System Sciences*, 20(8):2319–2333.

Souvignet, M., Oyarzún, R., Verbist, K. M., Gaese, H., and Heinrich, J. (2012). Hydro-meteorological trends in semi-arid north-central chile (29–32 s): Water resources implications for a fragile andean region. *Hydrological Sciences Journal*, 57(3):479–495.

Steiner, A. K., Ladstädter, F., Randel, W. J., Maycock, A. C., Fu, Q., Claud, C., Gleisner, H., Haimberger, L., Ho, S.-P., Keckhut, P., et al. (2020). Observed temperature changes in the troposphere and stratosphere from 1979 to 2018. *Journal of Climate*, 33(19):8165–8194.

Sylla, M., Gaye, A., and Jenkins, G. (2012). On the fine-scale topography regulating changes in atmospheric hydrological cycle and extreme rainfall over west africa in a regional climate model projections. *International Journal of Geophysics*, 2012.

Tang, G., Clark, M. P., Newman, A. J., Wood, A. W., Papalexiou, S. M., Vionnet, V., and Whitfield, P. H. (2020). Scdna: A serially complete precipitation and temperature dataset for north america from 1979 to 2018. *Earth System Science Data*, 12(4):2381–2409.

Taszarek, M., Allen, J. T., Marchio, M., and Brooks, H. E. (2021). Global climatology and trends in convective environments from era5 and rawinsonde data. *NPJ climate and atmospheric science*, 4(1):35.

Te Chow, V., Maidment, D. R., and Mays, L. W. (1988). *Applied hydrology*.

Teichmann, C., Jacob, D., Remedio, A. R., Remke, T., Buntemeyer, L., Hoffmann, P., Kriegsmann, A., Lierhammer, L., Bülow, K., Weber, T., et al. (2021). Assessing mean climate change signals in the global cordex-core ensemble. *Climate Dynamics*, 57:1269–1292.

Torma, C., Giorgi, F., and Coppola, E. (2015). Added value of regional climate modeling over areas characterized by complex terrain—precipitation over the alps. *Journal of Geophysical Research: Atmospheres*, 120(9):3957–3972.

Torrez-Rodriguez, L., Goubanova, K., Muñoz, C., and Montecinos, A. (2023). Evaluation of temperature and precipitation from cordex-core south america and eta-rcm regional climate simulations over the complex terrain of subtropical chile. *Climate Dynamics*, 61(7):3195–3221.

Trenberth, K. E. (2011). Changes in precipitation with climate change. *Climate Research*, 47(1-2):123–138.

Valdes-Pineda, R., Pizarro, R., Valdes, J. B., Carrasco, J. F., Garcia-Chevesich, P., and Olivares, C. (2016). Spatio-temporal trends of precipitation, its aggressiveness and concentration, along the pacific coast of south america (36–49 s). *Hydrological Sciences Journal*, 61(11):2110–2132.

Valenzuela, R., Garreaud, R., Vergara, I., Campos, D., Viale, M., and Rondanelli, R. (2022). An extraordinary dry season precipitation event in the subtropical andes: Drivers, impacts and predictability. *Weather and Climate Extremes*, 37:100472.

Valenzuela, R. A. and Garreaud, R. D. (2019). Extreme daily rainfall in central-southern Chile and its relationship with low-level horizontal water vapor fluxes. *Journal of Hydrometeorology*, 20(9):1829–1850.

Vera, C., Silvestri, G., Liebmann, B., and González, P. (2006). Climate change scenarios for seasonal precipitation in south america from ipcc-ar4 models. *Geophysical research letters*, 33(13).

Viale, M., Bianchi, E., Cara, L., Ruiz, L. E., Villalba, R., Pitte, P., Masiokas, M., Rivera, J., and Zalazar, L. (2019). Contrasting climates at both sides of the Andes in Argentina and Chile. *Frontiers in Environmental Science*, 7(May):1–15.

Viale, M. and Garreaud, R. (2014). Summer precipitation events over the western slope of the subtropical andes. *Monthly Weather Review*, 142(3):1074–1092.

Viale, M. and Nuñez, M. N. (2011). Climatology of winter orographic precipitation over the subtropical central andes and associated synoptic and regional characteristics. *Journal of Hydrometeorology*, 12(4):481–507.

Viale, M., Valenzuela, R., Garreaud, R. D., and Ralph, F. M. (2018). Impacts of atmospheric rivers on precipitation in southern south america. *Journal of Hydrometeorology*, 19(10):1671–1687.

Vicencio, J., Rondanelli, R., Campos, D., Valenzuela, R., Garreaud, R., Reyes, A., Padilla, R., Abarca, R., Barahona, C., Delgado, R., et al. (2020). The chilean tornado outbreak of may 2019: synoptic, mesoscale, and historical contexts. *Bulletin of the American Meteorological Society*, pages 1–52.

Vicuña, S., Garreaud, R. D., and Mcphee, J. (2010). Climate change impacts on the hydrology of a snowmelt driven basin in semiarid Chile. *Climatic Change*.

Vicuña, S., Vargas, X., Boisier, J. P., Mendoza, P. A., Gómez, T., Vásquez, N., and Cepeda, J. (2021). Impacts of climate change on water resources in chile. *Water resources of Chile*, pages 347–363.

Vuille, M. (1999). Atmospheric circulation over the bolivian altiplano during dry and wet periods and extreme phases of the southern oscillation. *International Journal of Climatology: A Journal of the Royal Meteorological Society*, 19(14):1579–1600.

Wang, G., Wang, D., Trenberth, K. E., Erfanian, A., Yu, M., Bosilovich, M. G., and Parr, D. T. (2017). The peak structure and future changes of the relationships between extreme precipitation and temperature. *Nature Climate Change*, 7(4):268–274.

Wi, S., Dominguez, F., Durcik, M., Valdes, J., Diaz, H. F., and Castro, C. L. (2012). Climate change projection of snowfall in the colorado river basin using dynamical downscaling. *Water Resources Research*, 48(5).

Wilcox, A. C., Escauriaza, C., Agredano, R., Mignot, E., Zuazo, V., Otarola, S., Castro, L., Gironas, J., Cienfuegos, R., and Mao, L. (2016). An integrated analysis of the march 2015 atacama floods. *Geophysical Research Letters*, 43(15):8035–8043.

Wilcoxon, F. (1992). *Individual comparisons by ranking methods*. Springer.

Yáñez-Morroni, G., Gironás, J., Caneo, M., Delgado, R., and Garreaud, R. (2018). Using the weather research and forecasting (wrf) model for precipitation forecasting in an andean region with complex topography. *Atmosphere*, 9(8):304.

Zegers, G., Navarro-Valdivia, L., Lagos-Zuñiga, M., Navarrete-Calvo, A., Caraballo, M. A., Niño, Y., McPhee, J., and Montserrat, S. (2021). An integrated modeling approach for mineral and metal transport in acidic rivers at high mountainous porphyry cu systems. *Journal of Hydrology*, 602:126718.

Zhai, P., Zhang, X., Wan, H., and Pan, X. (2005). Trends in total precipitation and frequency of daily precipitation extremes over china. *Journal of climate*, 18(7):1096–1108.

Zhang, W., Li, J., and Zhao, X. (2010). Sea surface temperature cooling mode in the pacific cold tongue. *Journal of Geophysical Research: Oceans*, 115(C12).

Zhao, Y., Feng, D., Yu, L., Wang, X., Chen, Y., Bai, Y., Hernández, H. J., Galleguillos, M., Estades, C., Biging, G. S., Radke, J. D., and Gong, P. (2016). Detailed dynamic land cover mapping of Chile: Accuracy improvement by integrating multi-temporal data. *Remote Sensing of Environment*, 183.

Zobel, Z., Wang, J., Wuebbles, D. J., and Kotamarthi, V. R. (2018). Analyses for high-resolution projections through the end of the 21st century for precipitation extremes over the united states. *Earth's Future*, 6(10):1471–1490.

Zolina, O., Simmer, C., Kapala, A., Bachner, S., Gulev, S., and Maechel, H. (2008). Seasonally dependent changes of precipitation extremes over germany since 1950 from a very dense observational network. *Journal of Geophysical Research: Atmospheres*, 113(D6).

Zou, S., Abuduwaili, J., Duan, W., Ding, J., De Maeyer, P., Van De Voorde, T., and Ma, L. (2021). Attribution of changes in the trend and temporal non-uniformity of extreme precipitation events in central asia. *Scientific Reports*, 11(1):1–11.

ANNEXES

Annex A

Supplementary material on Chapter 2

Table A.1 shows the trends of freezing level (H0) and Precipitable Water (PW) during seasonal Rx1day and p-value by season. Figures A.1 to A.5 show the fraction of observed days per year, by pressure levels on the five studied radiosonde stations normalized by the days of each year. Figure A.6 resumes the years considered by pressure level to compute trends and climate variation between historical periods. Figure A.7 shows the relationship between trends in seasonal Rx1day events and trends in associated Tx. Finally, Figure A.8 shows the time series of freezing levels of the soundings during the analyzed extreme precipitation events.

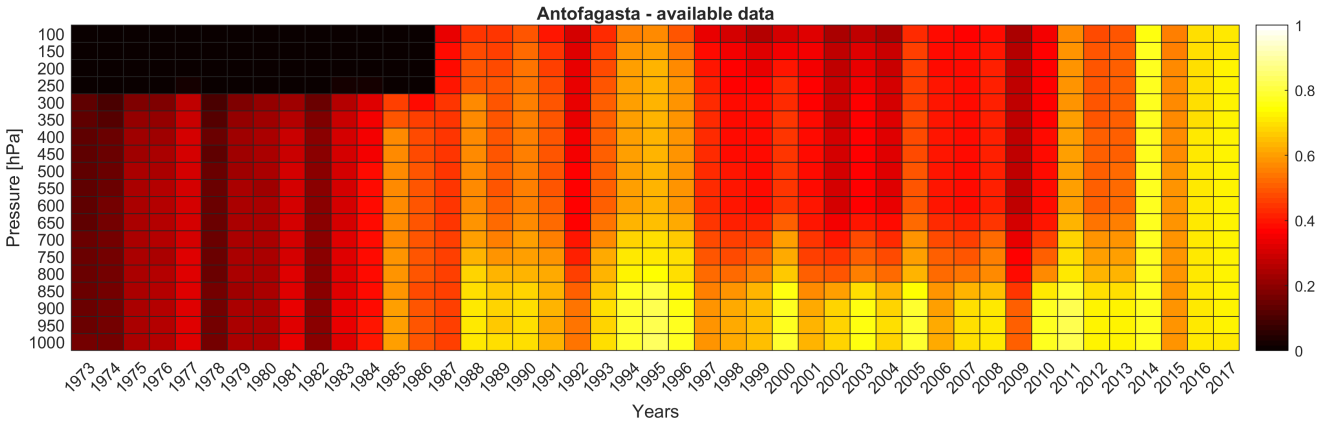

Figure A.1: Data availability of Antofagasta station during the years for different pressure levels

Table A.1: Sen's slope trends (p-value) for all radiosonde retrieved data during seasonal Rx1day events.

Radiosonde station (period)	Season	H0 [m/dec]	PW [mm/dec]
Antofagasta (1973-2017)	Annual	41 (0.57)	0.52 (0.553)
Quintero (1976-1999)	DJF	104 (0.659)	0.97 (0.726)
	MAM	60.6 (0.797)	3.5 (0.02)
	JJA	-34 (0.791)	-1.8 (0.359)
	SON	-5 (0.98)	—2.7(0.063)
Santo Domingo (2000-2017)	DJF	-10.9(0.961)	-1.3 (0.822)
	MAM	78.7 (0.773)	1.5 (0.537)
	JJA	240 (0.596)	-0.8 (0.705)
	SON	131 (0.449)	0.93 (0.802)
Puerto Montt (1973-2017)	DJF	41.7 (0.540)	0.83 (0.329)
	MAM	102 (0.269)	-0.23(0.812)
	JJA	11 (0.902)	0.28 (0.739)
	SON	-24 (0.790)	0.57 (0.298)
Punta Arenas (1976-2017)	DJF	15 (0.902)	0.11 (0.898)
	MAM	-34 (0.789)	0.62 (0.315)
	JJA	-51 (0.526)	-1 (0.109)
	SON	-71 (0.594)	∼0 (0.989)

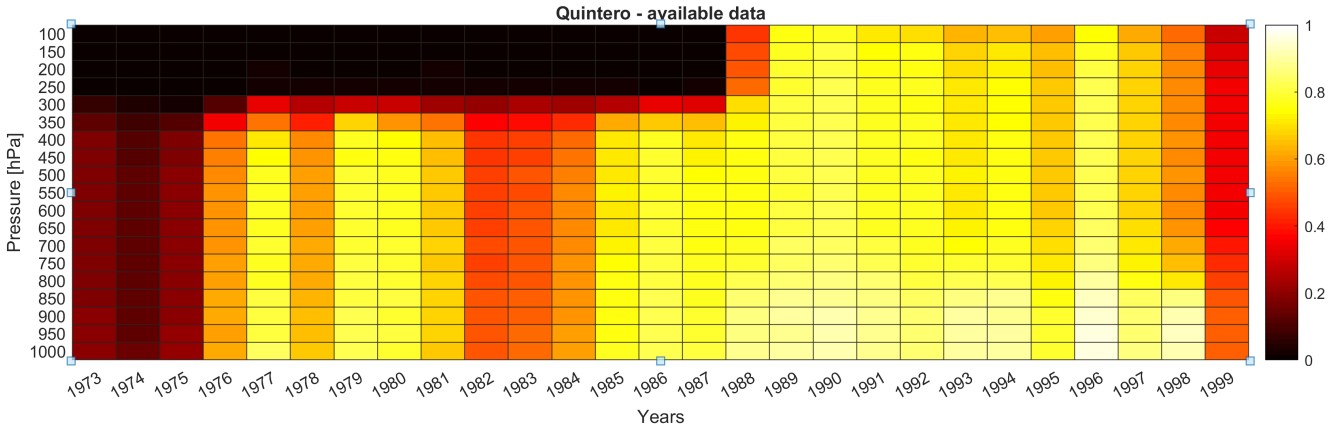

Figure A.2: Data availability of Quintero station during the years for different pressure levels

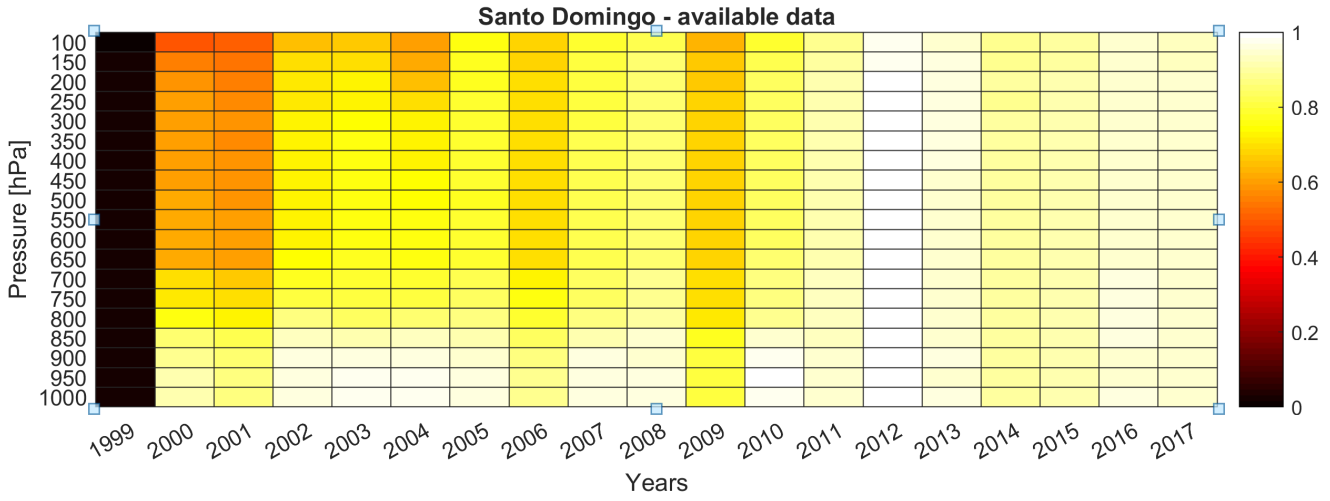

Figure A.3: Data availability of Santo Domingo station during the years for different pressure levels

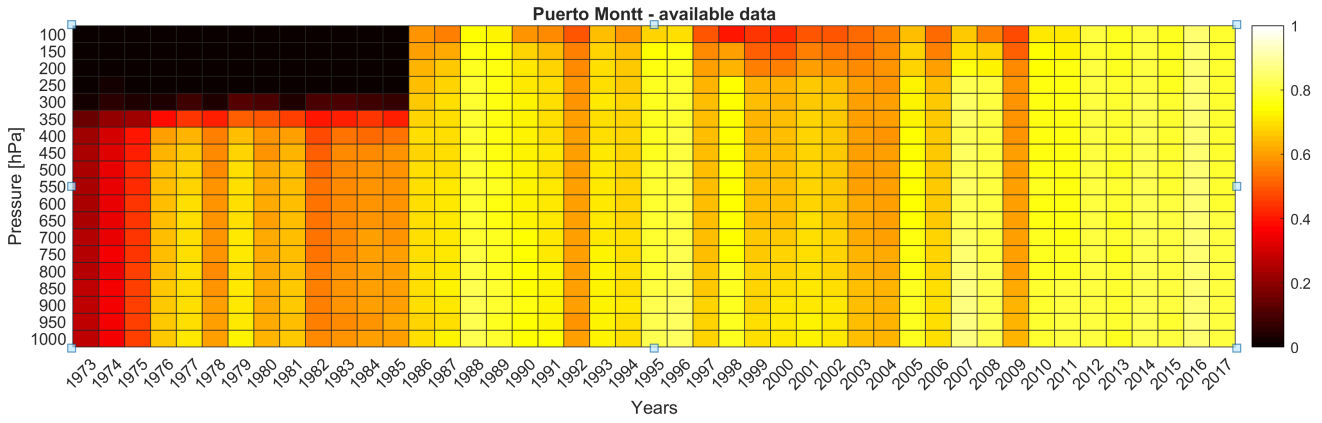

Figure A.4: Data availability of Puerto Montt station during the years for different pressure levels

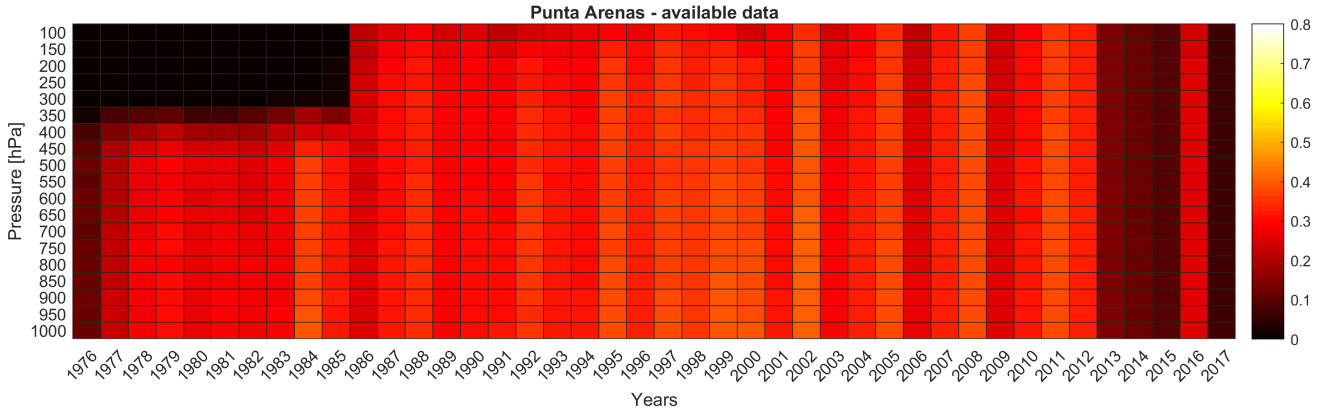

Figure A.5: Data availability of Punta Arenas station during the years for different pressure levels

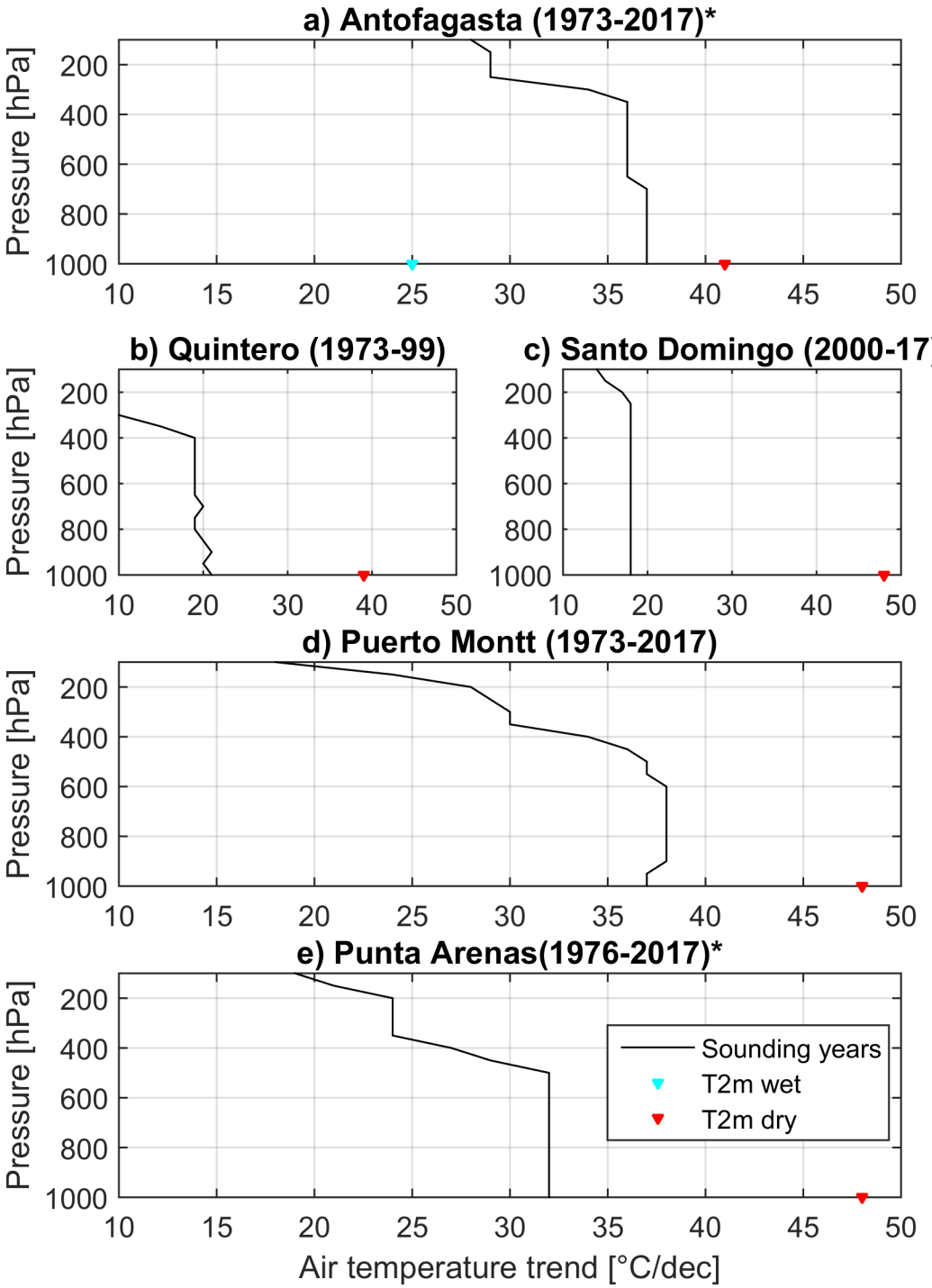

Figure A.6: Complete years considered for computing air temperature trends in radiosonde stations and their nearest surface station. * indicates that these stations don't have a long period as others (Table 2.1).

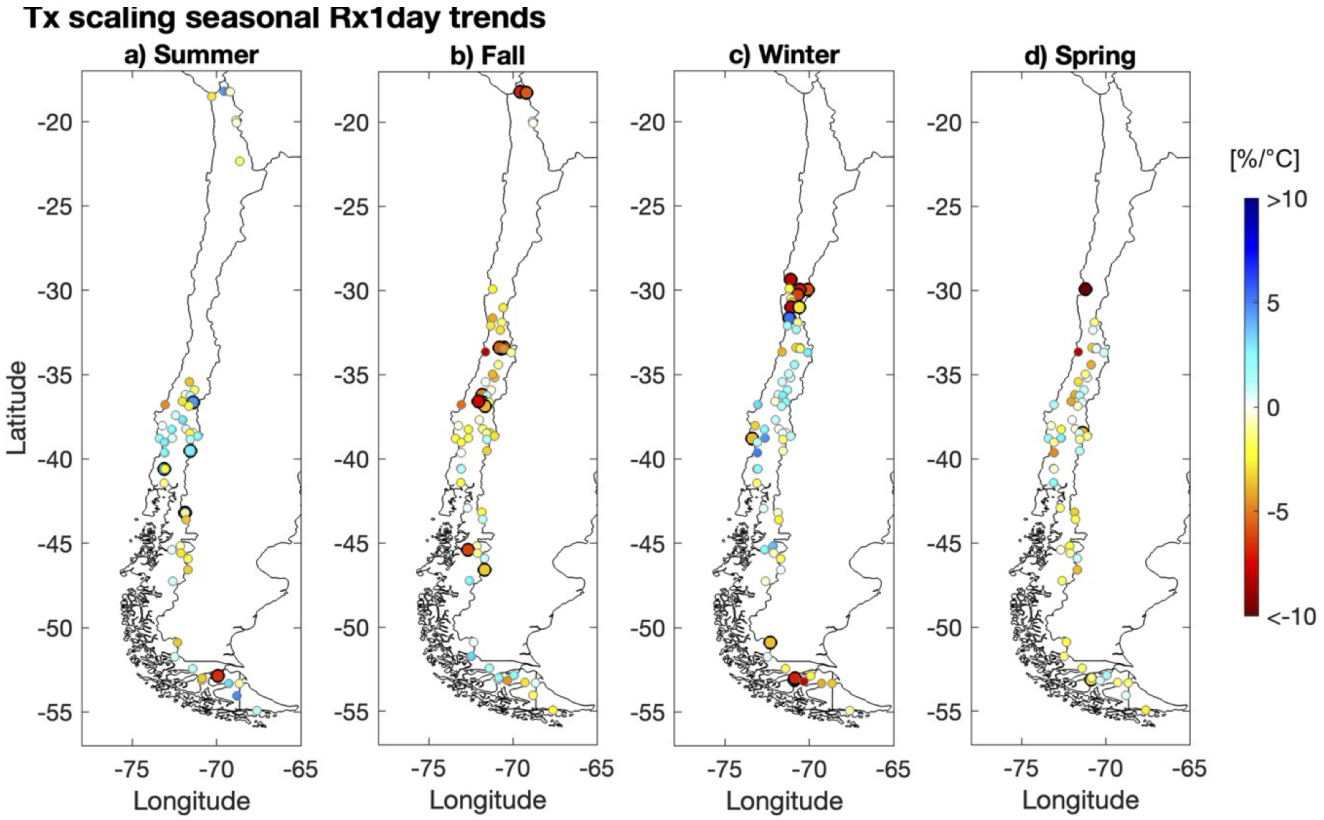

Figure A.7: Sensitivities of seasonal Rx1day to Tx variations during 1979-2017.

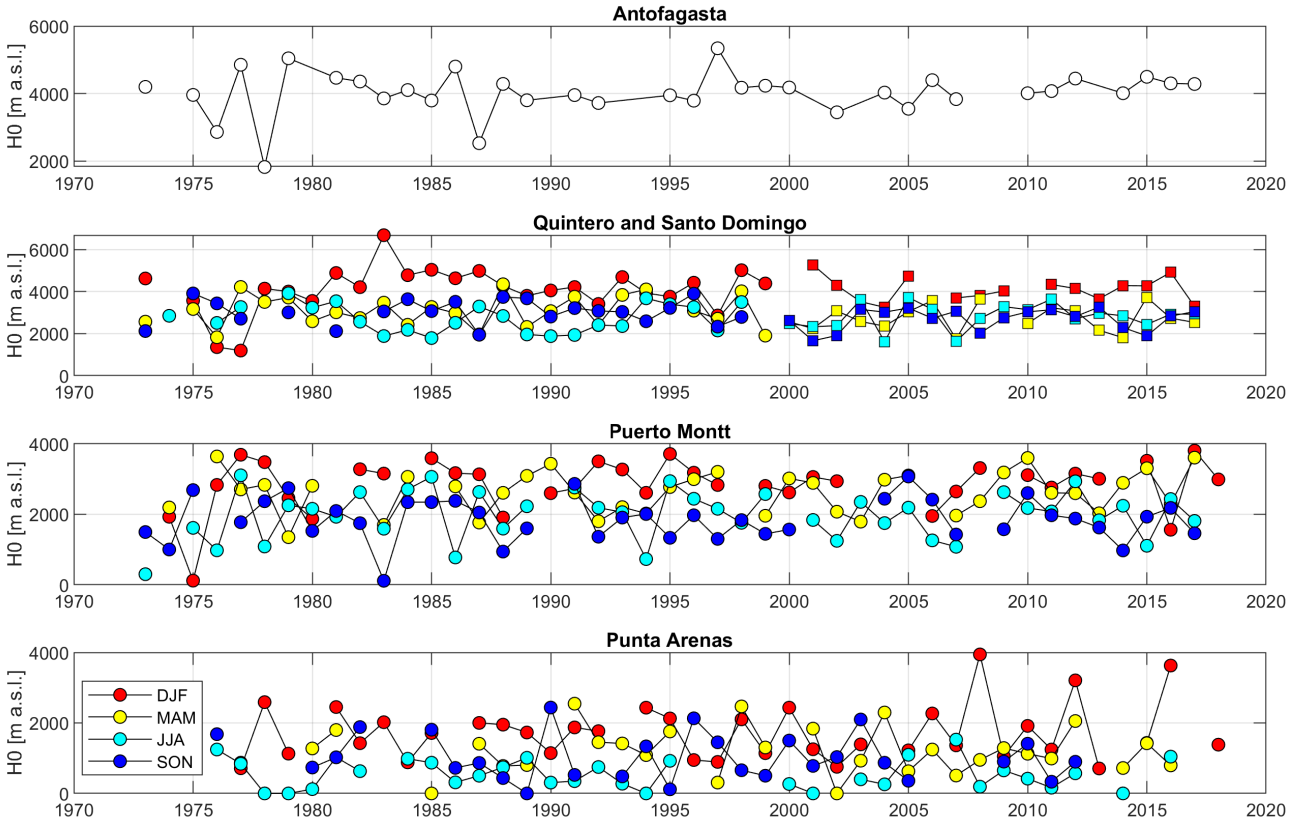

Figure A.8: Freezing levels observed during seasonal Rx1day events for all Radiosonde stations.

Annex B

Supplementary material on Chapter 3

This Appendix contains the supplementary information used in Chapter 3, related to projections of seasonal precipitation of the driving GCMs of the RCMs used in this study (Fig. B.1). The Figures B.2 to B.4 present the projected changes of the Eta simulations, while the Figures B.5 to B.7 presents the seasonal projections of the RegCM4.7 runs.

The driving GCMs, model reference, horizontal resolution, and analysis are listed in Table B.1. The schemes used in the RegCM4.5 at the Chilean domain and RegCM4.7, REMO2015 end Eta simulations in South America were mainly obtained by the references Bozkurt et al. (2019), Giorgi et al. (2012), Mbienda et al. (2023), Gutiérrez et al. (2021) and Mesinger et al. (2012) are listed in the Tables B.2 and B.3.

Table B.1: Regional climate models were used in this study. Pr: accumulated precipitation, Rx1day: Maximum 1-day precipitation, PI: Potential instability index.

Model	Driving GCMs	Reference	Horizontal resolution (lat-lon)	Analysis
RegCM4.7	HadGEM2-ES	Giorgi et al. (2012)	0.22	Pr, Rx1day & PI
	MPI-ESM-MR			
	NorESM1-M			
RegCM4.5	MPI-ESM-MR	Bozkurt et al., (2019)	0.10	Pr, Rx1day
REMO2015	HadGEM2-ES	Jacob et al. (2007)	0.22	Pr, Rx1day
	NorESM1-M			
	MPI-ESM-LR			
Eta	CanESM2	Mesinger et al. (2012)	0.20	Pr, Rx1day & PI
	MIROC5			
	HadGEM2-ES			

Table B.2: Parametrizations used in the RegCM4.5 and RegCM4.7 models. SIC: Snow Ice Content, SST: Sea Surface Temperature.

Model Aspect	Regional Climate Model	
	RegCM4.5	RegCM4.7
Radiative Transfer	NCAR Modified CCM3 (Kiehl et al. 1998)	
Planetary Boundary Layer	Modified Holtslag et al. (1990)	Modified Holtslag et al. (1990) and Grell (1993) with Arakawa and Schubert (1974) closure
Cumulus Convection	Grell scheme (Grell 1993) with a cumulus closure scheme of Fritsch and Chappell (Fritsch and Chappell 1980)	Simplified Kuo (Anthes et al. 1987) Grell (Grell 1993) MIT (Emanuel & Zivkovic-Rothman1999) Tiedtke (Tiedtke 1989)
Resolvable Precipitation	SUBEX (Pal et al. 2000)	
Land Surface	BATS (Dickinson et al. 1993)	CLM4.5 (Steiner et al. 2009)
Ocean fluxes	Zeng et al. (1998) and Prescribed SST	
Interactive Aerosols	No active aerosol chemical model	

Table B.3: Parametrizations used in the REMO2015 and Eta models. SIC: Snow Ice Content, SST: Sea Surface Temperature.

Model Aspect	Regional Climate Model	
	REMO2015	Eta
Radiative Transfer	ECMWF-ECHAM4 (Roeckner et al. 1992)	Geophysical Fluid Dynamics Laboratory scheme. The scheme includes short-wave (Lacis and Hansen 1974) and long-wave radiation (Fels and Schwarzkopf 1975).
Planetary Boundary Layer	Louis (1979)	Mellor-Yamada (1974) 2.5 closure level
Cumulus Convection	Mass-flux scheme Tiedtke (1989) Nordeng (1996) Pfeifer (2006)	Betts-Miller-Janjic cumulus parameterization scheme (Janjic 1994)
Resolvable Precipitation	Lohmann and Roeckner (1996) with some revisions, and a diagnostic cloud cover scheme (Sundqvist et al., 1989)	N.A.
Land Surface	A tile-based scheme including annual cycle of albedo (Rechid et al., 2009)	NOAH scheme (Ek et al., 2003).
Ocean fluxes	Prescribed SST and SIC	Prescribed SST
Interactive Aerosols	Prescribed (Tanré et al., 1984)	No active aerosol chemical model

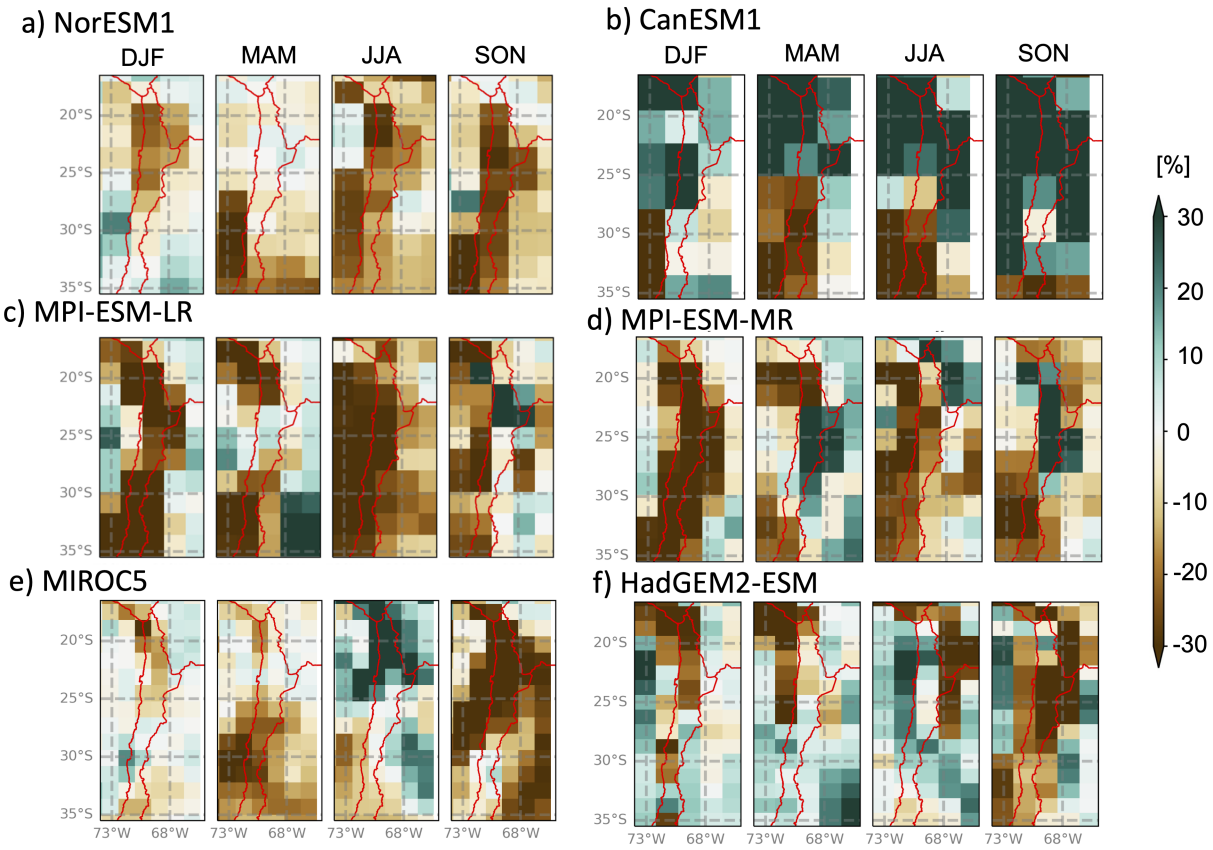

Figure B.1: Seasonal change of precipitation proyected by the driving GCMs used in RCMs of Chapter 3

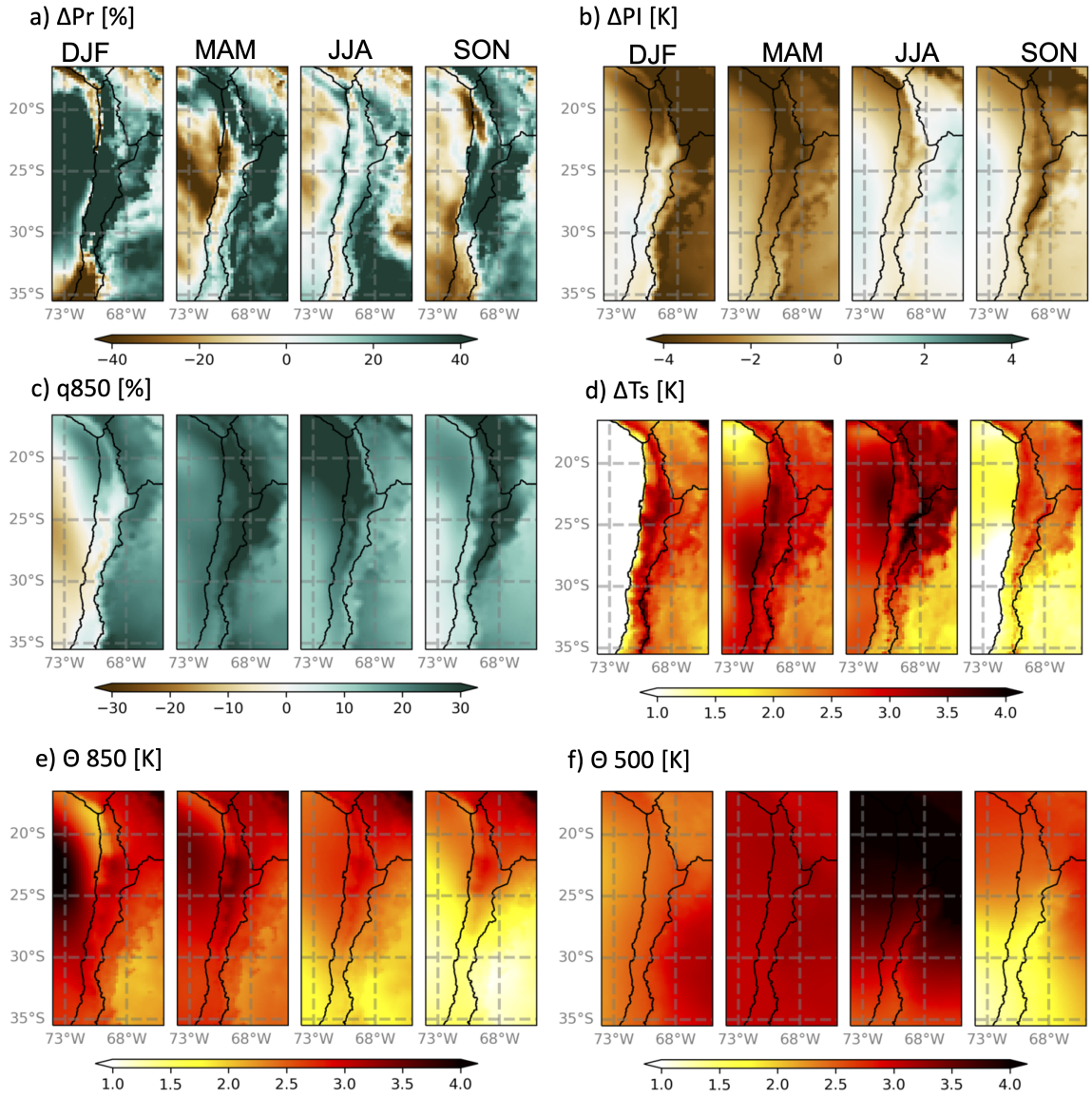

Figure B.2: ETA-HadGEM2 simulated changes of a) Seasonal precipitation, b) Potential Instability, c) Specific humidity at 850 hPa, d) Surface temperature, e) Potential temperature at 850 hPa, and f) Potential temperature at 500 hPa.

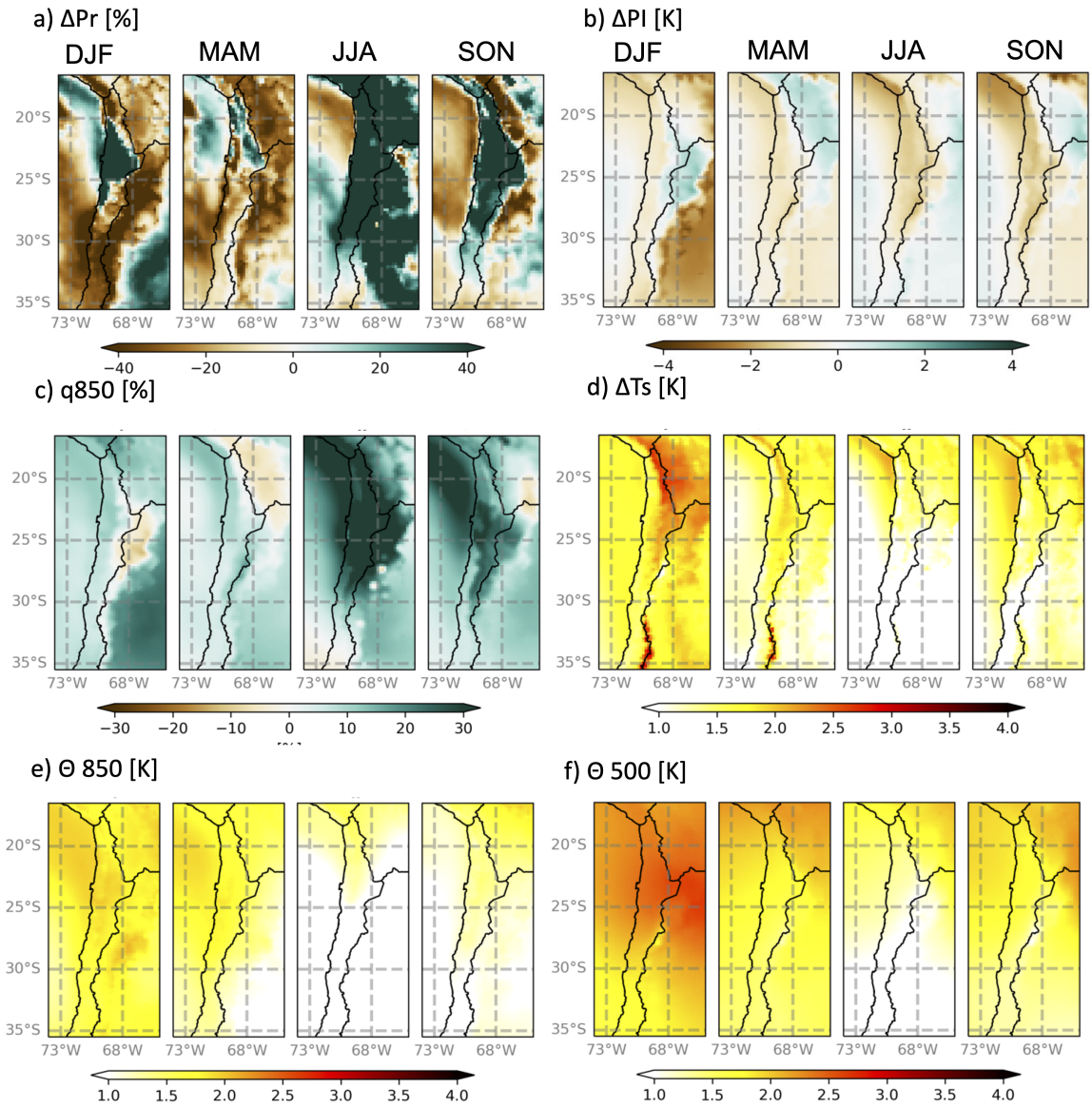

Figure B.3: Same as Fig. B.2 but for Eta-MIROC5 simulation.

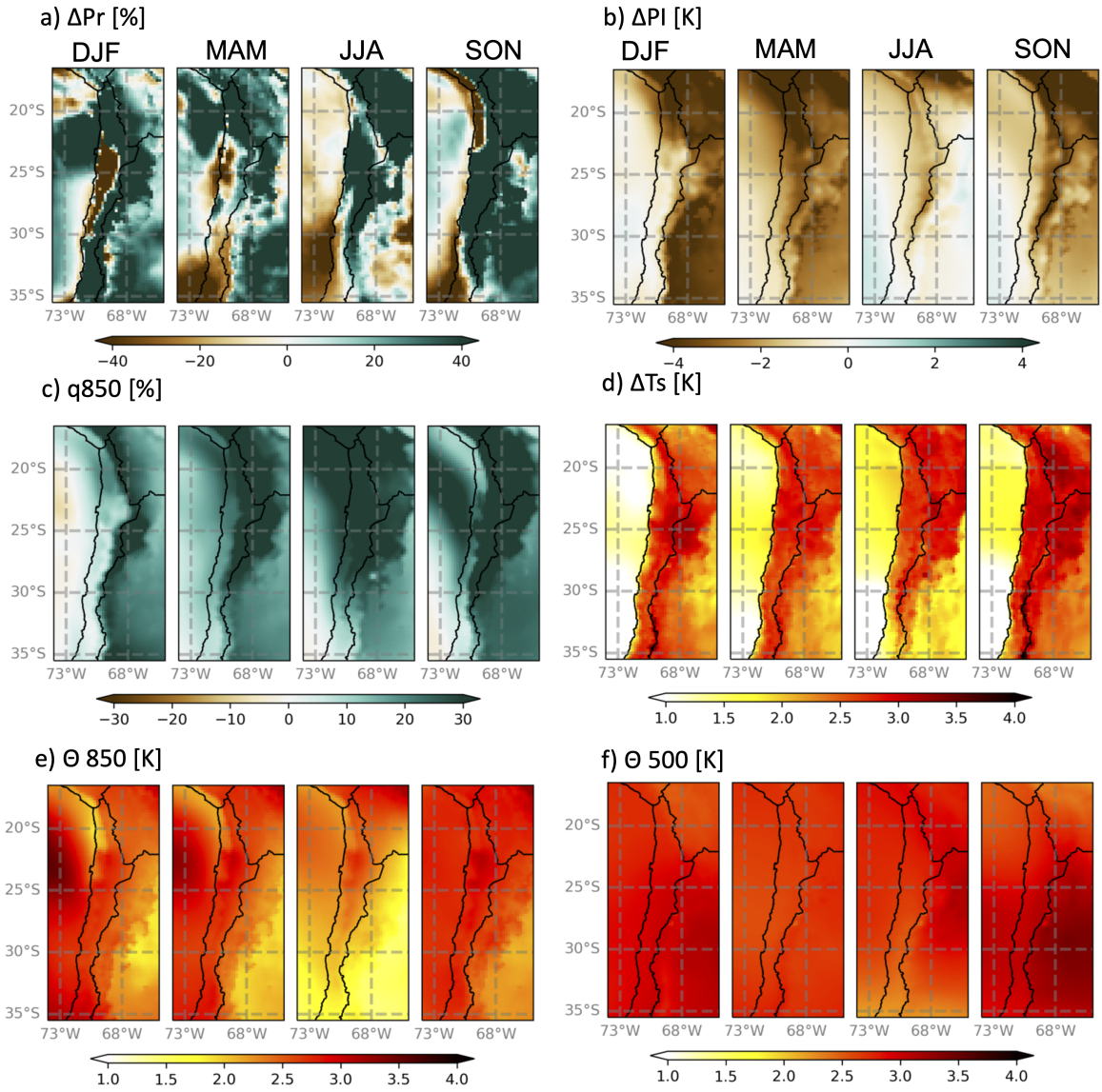

Figure B.4: Same as Fig. B.2 but for Eta-CanESM2 simulation.

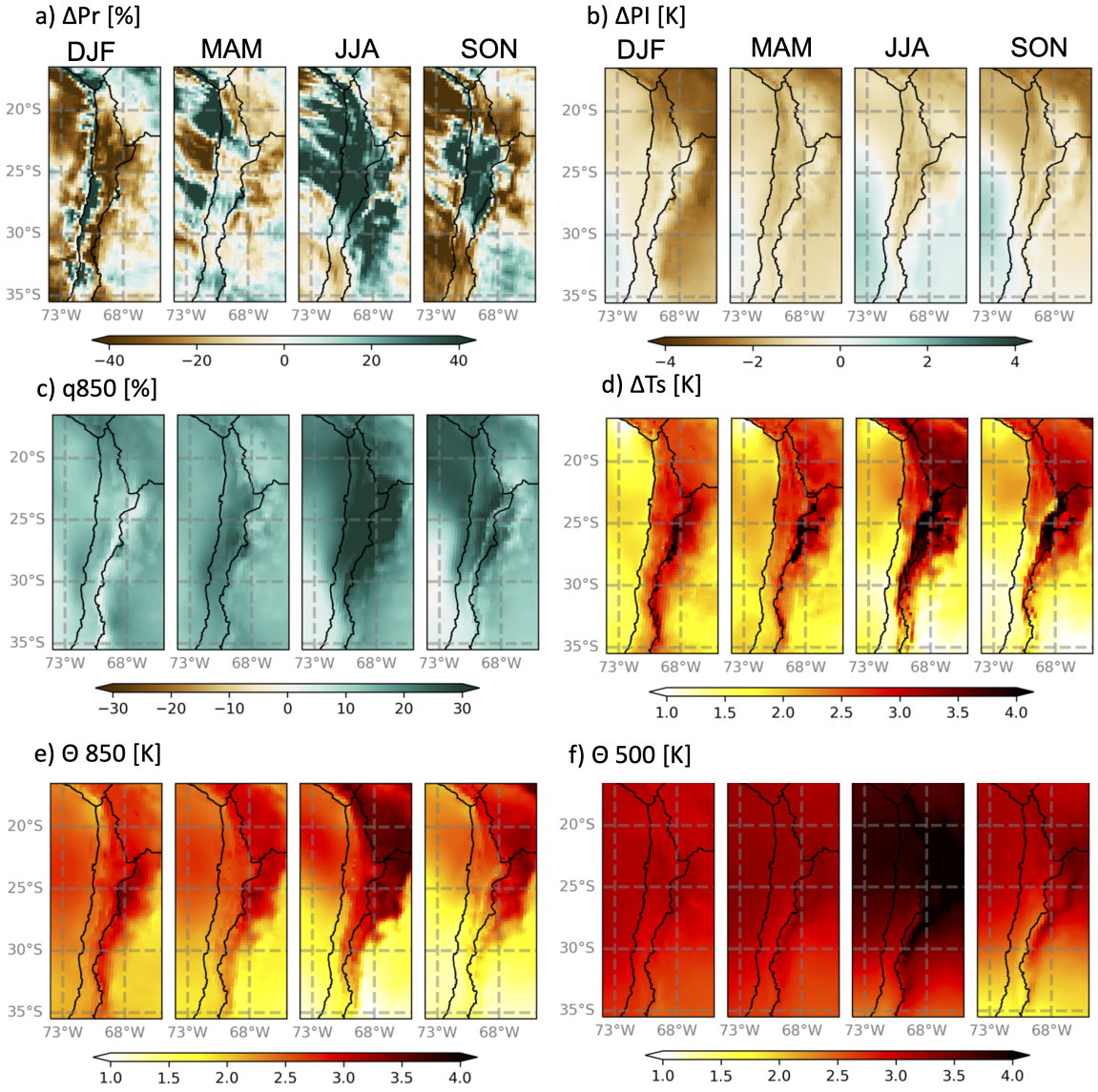

Figure B.5: Same as Fig. B.2 but for RegCM4.7-HadGEM2 simulation.

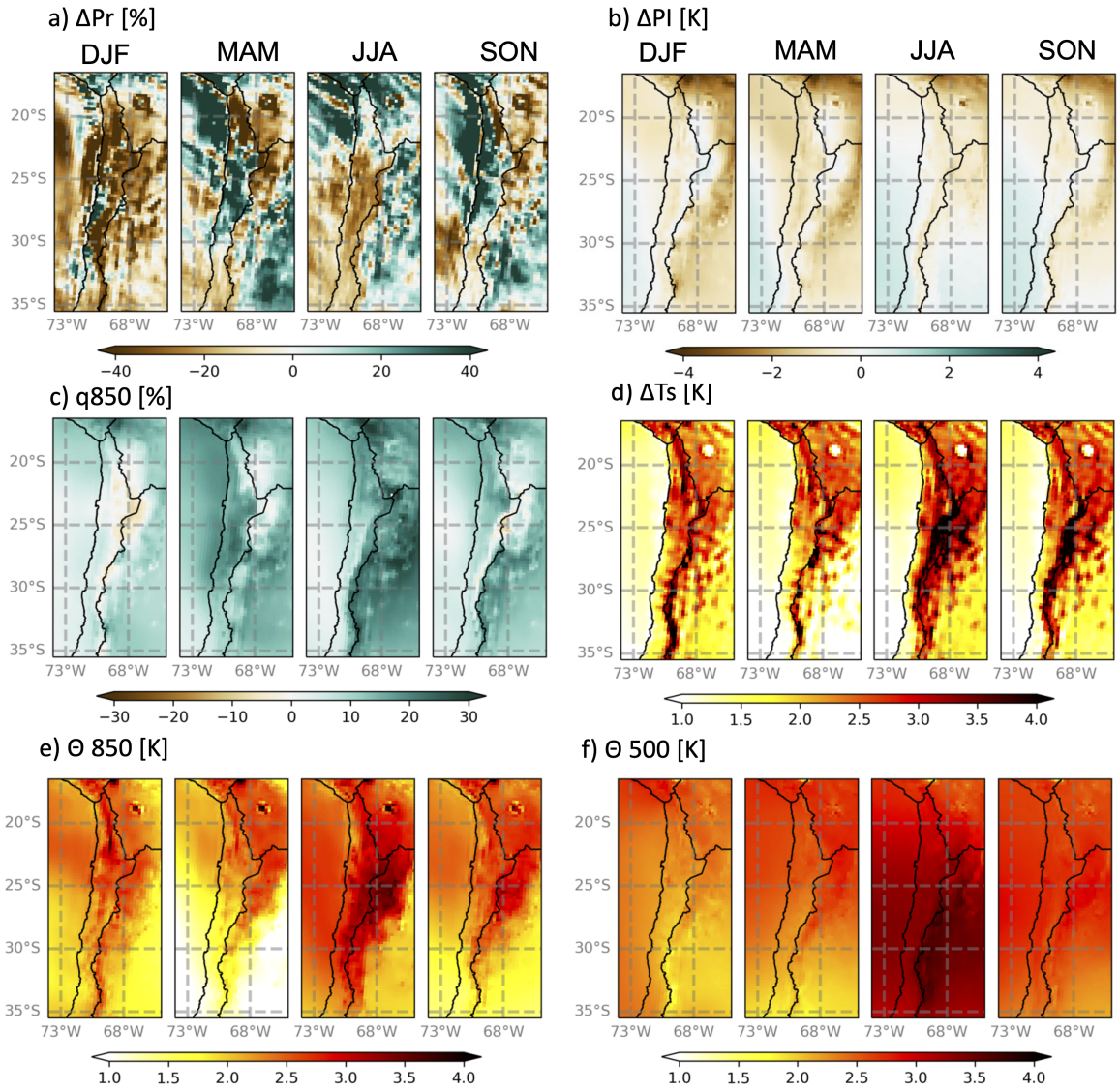

Figure B.6: Same as Fig. B.2 but for RegCM4.7-MPI-ESM-MR simulation.

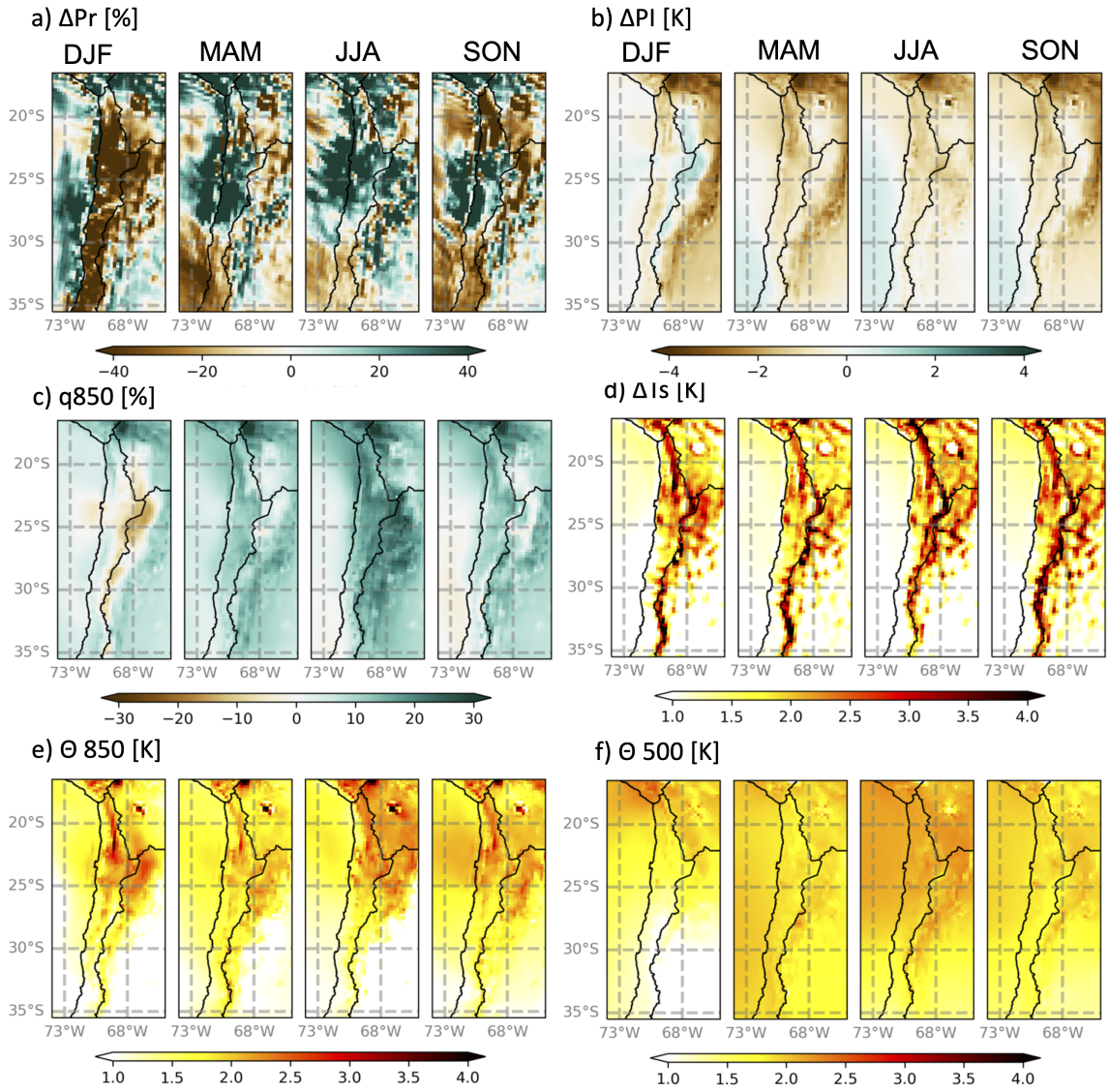

Figure B.7: Same as Fig. B.2 but for RegCM4.7-HadGEM2 simulation.

Annex C

Supplementary material on Chapter 4

This appendix shows the behavior of the hourly time series evaluation for Pearson correlation coefficient and RMSE from the stations listed in Table 4.1. Figure C.1 shows the Bias obtained for Hourly precipitation, temperature, relative humidity, wind speed, and wind direction. Similarly, figures C.2 and C.3 show the Pearson Correlation coefficient and the Root Mean Square Error in the same variables and hourly stations. The tables C.1 and C.2 resume the percentiles 25th, 50th, and 75th of the evaluated metrics for each simulation and event of hourly relative humidity and wind speed.

Table C.1: Evaluation metrics for hourly simulations of relative humidity. The rows of each WRF configuration represent the 25th, 50th, and 75th percentiles.

WRF Configuration	Feb 2017			Jan 2021		
	Bias [%]	r	RMSE [%]	Bias [%]	r	RMSE [%]
A-Base	-11.59	0.40	15.63	-17.06	**0.65**	17.28
	-8.04	0.54	19.18	-10.43	**0.74**	20.21
	-1.21	0.70	20.18	-4.22	**0.78**	26.45
B-Lin MP	-10.55	0.42	14.95	-21.18	0.61	19.48
	-7.22	0.55	18.21	-12.06	0.67	21.41
	-0.73	0.70	19.63	-10.31	0.75	31.45
C-MM5-YSU SF-PBL	**-11.37**	**0.50**	**12.96**	-15.29	0.57	17.28
	-3.41	**0.59**	**16.47**	-7.98	0.69	21.83
	0.64	**0.72**	**17.59**	-3.35	0.74	25.53
D-Noah LSM	-9.66	0.41	14.56	**-14.39**	0.66	**17.07**
	-5.30	0.54	18.51	**-6.85**	0.73	**19.05**
	-0.63	0.65	20.69	**-3.37**	0.77	**24.22**
E-Thompson MP	-11.74	0.41	15.12	-24.27	0.59	20.20
	-8.21	0.54	19.26	-13.64	0.65	22.77
	-1.06	0.68	19.84	-10.76	0.70	31.74
F-Janjic SF-PBL	-12.10	0.45	14.13	-19.21	0.60	17.55
	-3.42	0.56	17.37	-14.49	0.62	23.78
	1.22	0.63	20.18	-9.45	0.75	30.28

Table C.2: Evaluation metrics for hourly simulations of wind speed. The rows of each WRF configuration represent the 25th, 50th, and 75th percentiles.

WRF Configuration	Feb 2017			Jan 2021		
	Bias [m/s]	r	RMSE [m/s]	Bias [m/s]	r	RMSE [m/s]
A-Base	0.52	0.22	1.87	-0.39.	**0.19**	1.95
	1.13	0.43	2.51	0.76	**0.26**	2.76
	1.80	0.50	3.43	1.23	**0.39**	3.06
B-Lin MP	0.53	0.23	1.87	**-0.23**	0.13	2.10
	1.07	0.45	2.51	**0.95**	0.26	2.77
	1.74	0.50	3.36	**1.11**	0.38	3.12
C-MM5-YSU SF-PBL	**0.08**	0.30	1.89	-0.61	0.12	**1.97**
	1.12	0.41	2.68	0.5	0.17	**2.37**
	1.82	0.45	3.49	1.17	0.33	**3.10**
D-Noah LSM	0.55	0.27	1.92	**-0.42**	0.18	1.99
	1.15	0.40	2.56	**0.68**	0.26	2.55
	1.76	0.47	3.23	**1.17**	0.38	3.27
E-Thompson MP	0.43	**0.23**	**1.81**	**-0.23**	0.08	2.05
	1.06	**0.43**	**2.49**	**0.86**	0.19	2.82
	1.85	**0.50**	**3.45**	**1.18**	0.38	3.16
F-Janjic SF-PBL	0.51	0.25	2.20	-0.25	0.17	2.30
	1.42	0.36	3.22	0.71	0.25	2.69
	2.63	0.47	3.91	1.20	0.38	3.17

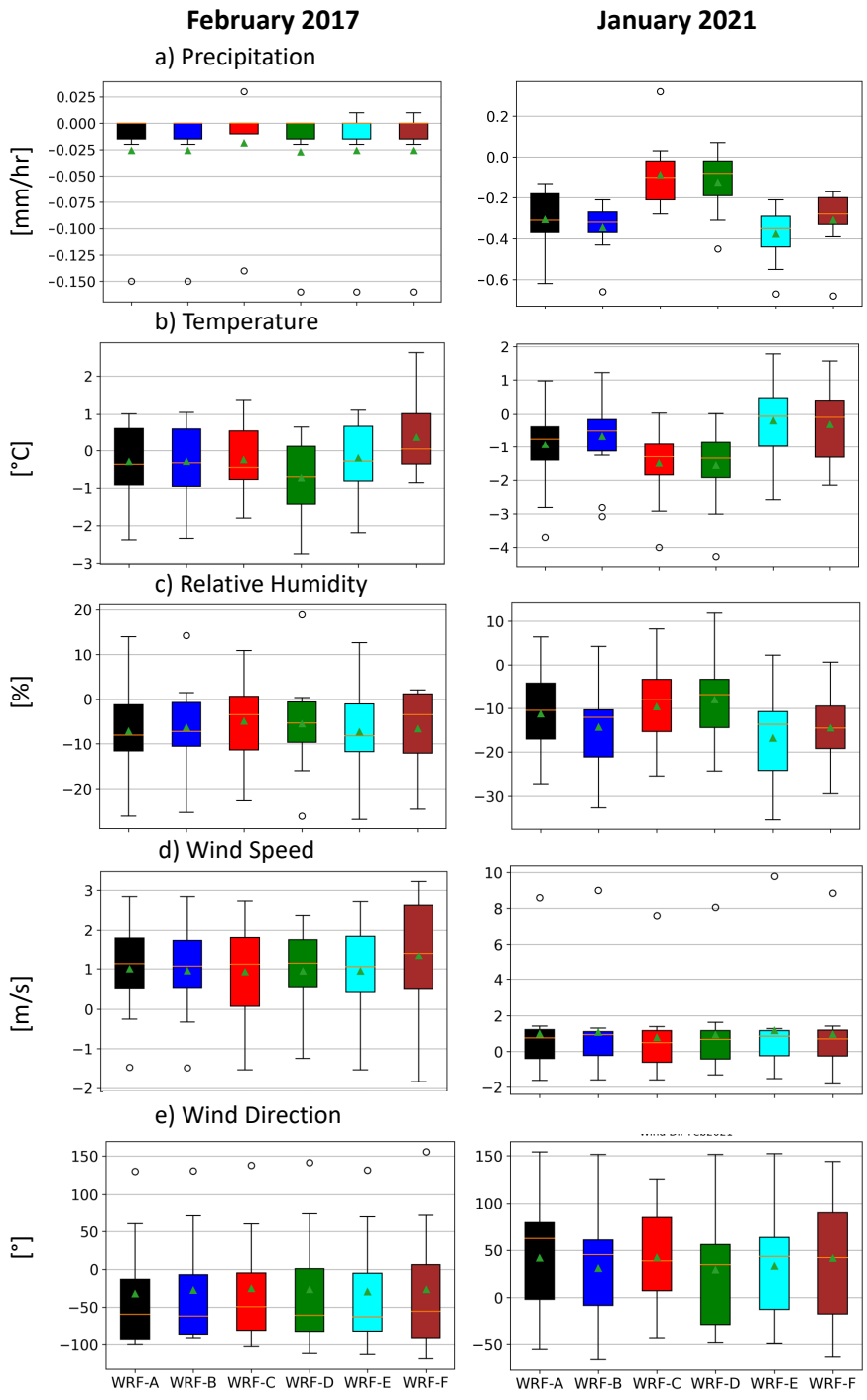

Figure C.1: Biases obtained from the stations and variables used in Chapter 4 for hourly station records.

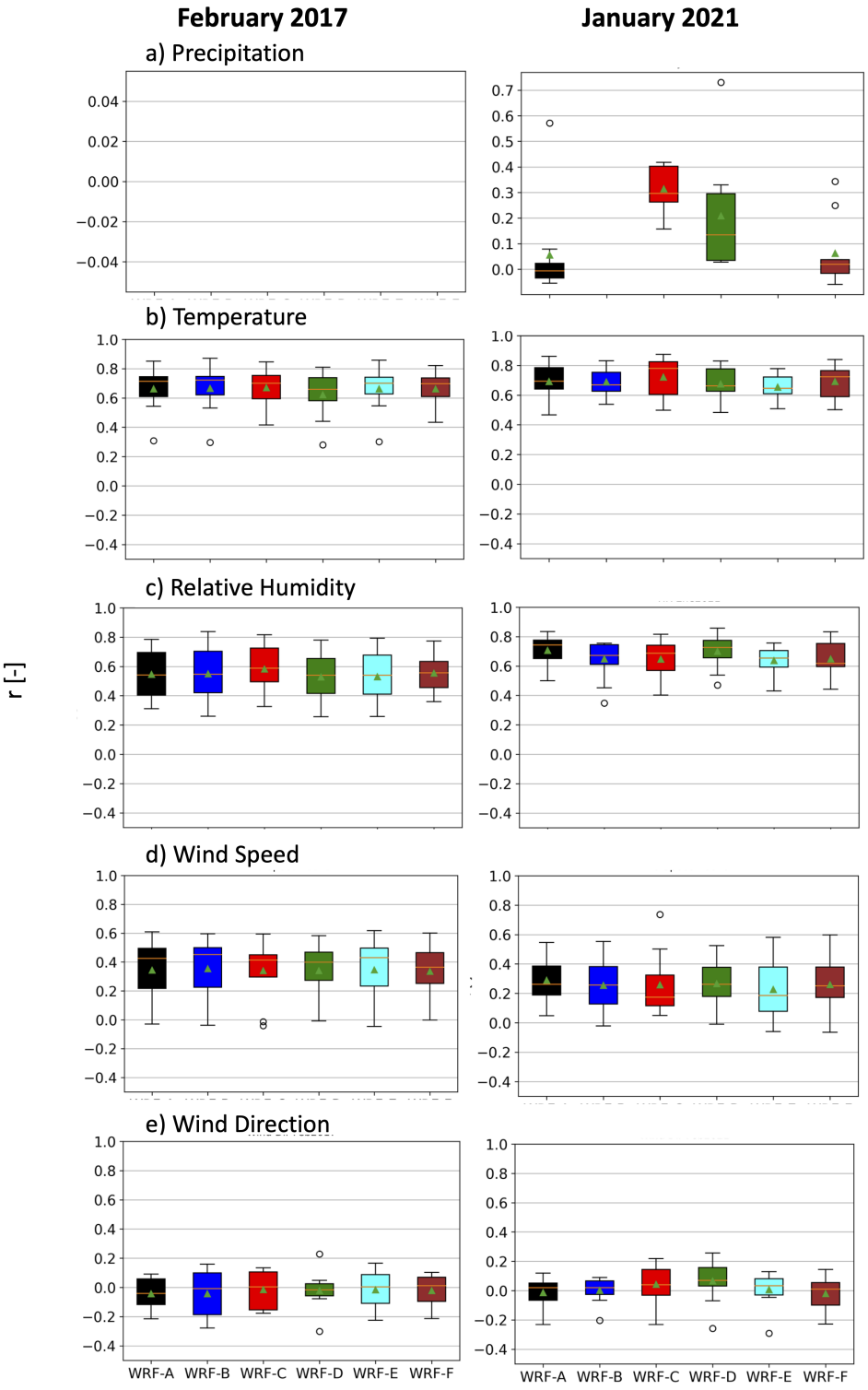

Figure C.2: Pearson correlation coefficient obtained from the stations and variables used in Chapter 4 for hourly station records.

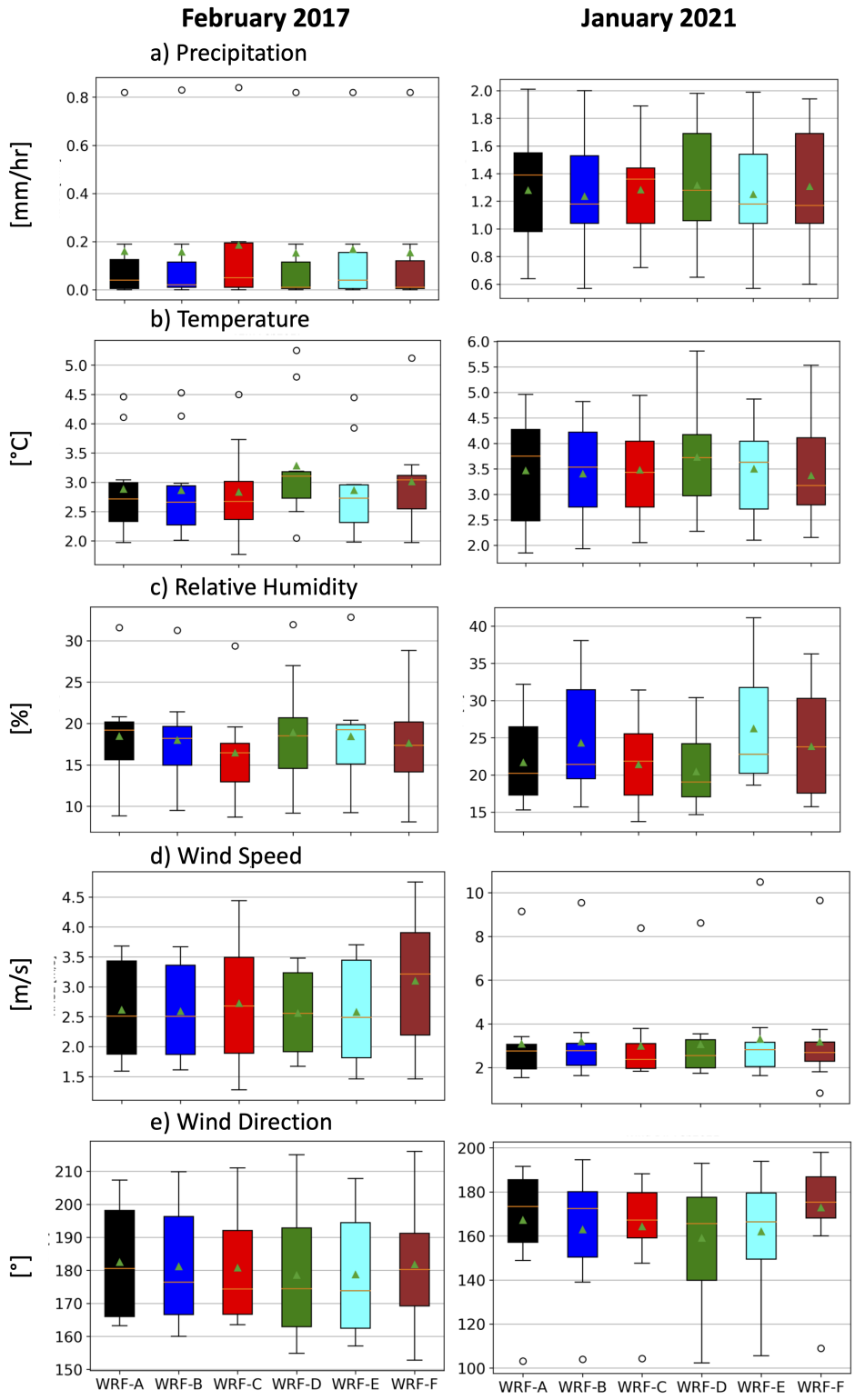

Figure C.3: RMSE obtained from the stations and variables used in Chapter 4 for hourly station records.